Universität Hamburg

From Clusters to Nanocrystals: Nucleation and Growth of Semiconductor Nanocrystals in a Continuous-Flow Device

---

Von Clustern zu Nanokristallen: Nukleation und Wachstum von Halbleiternanokristallen in einem kontinuierlichen Flussreaktor

Dissertation
zur Erlangung des Doktorgrades
Dr. rer. nat.
im Fachbereich Chemie
Fakultät für Mathematik, Informatik
und Naturwissenschaften

vorgelegt von:
Robert Seher

2017

Die Druckfreigabe für diese Arbeit wurde am 06.10.2017 durch das Studienbüro Chemie der Universität Hamburg erteilt.

1. Gutachter: Prof. Dr. Horst Weller
2. Gutachter: PD Dr. Christian Klinke
Datum der Disputation: 06.10.2017

Abstract

The present work details the investigation of the nucleation and growth behaviour of colloidal CdSe nanocrystals (NCs) with special regard to the role of magic-sized clusters (MSCs) as intermediates in the reaction. For this purpose a continuous-flow device (CFD), which allowed high-temperature NC synthesis combined with online ultraviolet (UV)/visible (Vis) absorption spectroscopy for characterization, was developed and set up. The CFD's modular design allowed a rapid variation of the time resolution and the incorporation of a home-built X-ray flow cell, allowing *in situ* synchrotron X-ray scattering experiments.

Following the variation of nucleation and growth temperature, as well as residence time, during the synthesis of CdSe NCs in the CFD, substantial evidence for magic-sized intermediates during the NC formation was obtained. From the available data, a reaction pathway, starting at the formation of the nuclei, followed by subsequent sequential growth of different-size moieties of MSCs and ending in the formation and subsequent continuous growth of regular NCs via Ostwald ripening, was deduced.

Specific growth experiments, in which preprepared solutions were heated to different growth temperatures and residence times were varied, were conducted In these, the previously formulated reaction pathway could be corroborated by identifying individual cluster species, that were formed as intermediates. Furthermore, the transition from magic-sized intermediate to continuously growing NC via Ostwald ripening was observed clearly in the absence of excess monomer.

In conclusion, it was possible to develop and establish an experimental apparatus, allowing time-resolved study of NC formation, as well as other processes, taking place on comparable time scales. Using this apparatus, a reaction pathway describing the formation of CdSe NCs, via intermediate MSCs, growing via a sequential growth mechanism, could be identified.

Kurzfassung

Die vorliegende Arbeit behandelt die Untersuchung von Nukleations- und Wachstumsverhalten von kolloidalen CdSe-Nanokristallen, mit besonderem Augenmerk auf die Rolle von Clustern magischer Größe als Zwischenprodukt der Reaktion. Zu diesem Zweck wurde ein kontinuierlicher Flussreaktor entwickelt und aufgebaut, der die Möglichkeit zur Hochtemperatursynthese von Nanokristallen, kombiniert mit deren Charakterisierung mittels UV/Vis-Absorptionsspektroskopie, bot. Der modulare Aufbau des Flussreaktors erlaubte sowohl die schnelle Variation der Zeitauflösung, als auch den Einbau einer selbstkonstruierten Röntgenflusszelle, durch die die Durchführung von *in situ* Röntgenstreuexperimenten am Synchrotron ermöglicht wurde.

Durch die Variation von Nukleations- und Wachstumstemperaturen sowie Verweilzeiten während der Synthese von CdSe-Nanokristallen im Flussreaktor konnten deutliche Hinweise auf Intermediate magischer Größe während der Nanokristallbildung beobachtet werden. Aufgrund der erhaltenen Daten konnte ein Reaktionsweg formuliert werden. Dieser beinhaltet die anfängliche Bildung von Nukleationskeimen, gefolgt von anschließendem sequentiellen Wachstum von magischen Clustern verschiedener Größe und endet in der Bildung und abschließendem kontinuierlichen Wachstum von regulären Nanokristallen durch Ostwaldreifung.

Spezielle Wachstumsexperimente, in denen zuvor hergestellte Nanokristalllösung auf verschiedene Wachstumstemperaturen geheizt wurde und die Verweilzeit variiert wurde, wurden durchgeführt. In diesen konnte der zuvor formulierte Reaktionsweg bestätigt werden, indem einzelne Clusterspezies, die an der Reaktion beteiligt waren, identifiziert werden konnten. Zudem konnte in Abwesenheit von überschüssigem, unreagierten Monomer der Übergang von Intermediaten magischer Größen zu kontinuierlich wachsenden Nanokristallen per Ostwaldreifung eindeutig beobachtet werden.

Zusammenfassend war es möglich, einen experimentellen Aufbau zu entwickeln und zu etablieren, der die zeitaufgelöste Untersuchung der Nanokristallbildung sowie anderer Prozesse, die auf ähnlicher Zeitskala stattfinden, ermöglicht. Mit Hilfe dieses Aufbaus ist es gelungen, einen Reaktionspfad zu identifizieren, der die Bildung von CdSe-Nanokristallen über Zwischenprodukte magischer Größe beschreibt, die über einen sequentiellen Wachstumsmechanismus wachsen.

Contents

Glossary

ASCII American standard code for information interchange.

CFD continuous-flow device.

Cyanex Cyanex® 923, a mixture of tertiary alkyl phosphine oxides produced by Cytec Industries Inc..

DESY Deutsches Elektronensynchrotron, synchrotron facility in Hamburg, Germany.

DPE diphenylether.

EDX energy-dispersive X-ray spectrometry.

ESRF European Synchrotron Radiation Facility, synchrotron facility in Grenoble, France.

EtOH Ethanol.

EXAFS extended X-ray absorption fine structure.

FWHM full width at half-maximum.

HWHM half width at half-maximum.

ICDD International Centre for Diffraction Data.

ID02 The time-resolved ultra small-angle X-ray scattering beamline at ESRF.

KFC Kapton flow cell.

LCAO linear combination of atomic orbitals.

MeOH Methanol.

MSC magic-sized cluster.

NC nanocrystal.

OD optical density.

ODE octadec-1-ene.

ODPA octadecylphosphonic acid.

P03 The micro- and nanofocus X-ray scattering beamline at PETRA III, DESY.

P65 The high-energy X-ray absorption spectroscopy beamline at PETRA III, DESY.

PL photoluminescence.

PLE photoluminescence excitation.

QD quantum dot.

QY quantum yield.

RTD resistance temperature detector.

SAXS small-angle X-ray scattering.

TEM transmission electron microscope.

TOP trioctylphosphine.

UV ultraviolet.

Vis visible.

WAXS wide-angle X-ray scattering.

XRD X-ray powder diffraction.

1. Introduction

Since the first reports of their synthesis and characterization in the 1980s,[1–4] semiconductor NCs, or quantum dots (QDs), have been on a constant journey of increasing importance: from interesting model systems as artificial atoms,[5,6] to commercial application in mass-market consumer electronics.[7,8] This rapid rise to fame is mostly due to their unique electronic properties, arising from the quantization of their energy states, which leads to a size-dependence of their electronic band gap in a phenomenon called the quantum size effect.[9–11] As a result, the wavelength of light, they absorb and emit, can be controlled, by controlling the particle size, a property, which makes them uniquely suited for applications in display technology.[12] Besides their current commercial applications, a multitude of additional application for QDs are currently discussed in scientific literature. These range from applications in nanoelectronics, like sensors,[13–15] transistors,[16–18] light-emitting[19–21] or photovoltaic devices,[22–24] to their use as fluorescent probes in bioimaging.[25–27]

Due to the diversity of the potential applications, the specific properties, required from a material in question, vary greatly between applications.[28] In consequence, a wide range of different QD materials have been synthesized, covering a wide spectrum of electronic band gaps, sizes, shapes, mechanical properties and surface chemistries.[29–31] Development of new QD synthesis protocols, targeted at emerging applications, represents a considerable investment of time and resources, as suitable conditions have to be determined in expansive empirical trials. Avoiding this, by devising tailor-made synthesis strategies based on a systematic understanding of the fundamental formation principles of QDs would be greatly beneficial.

To gain this understanding, it is necessary, to develop a kinetic model of NC nucleation and growth through time-resolved measurement of size, shape, and composition evolution during their synthesis. Apart from several theoretical[32–35] and precursor conversion based studies,[36–38] some experimental studies, reporting conclusive mechanisms for NC nucleation and growth, have been published more than ten years ago, both, for metallic,[39] as well as semiconductor NCs.[40–42] These studies typically relied on analyzing samples manually taken from batch reactions, and in consequence only allowed investigation of later stages of the formation reaction.

Technological advances during later years allowed time-resolved *in situ* analyses down to the ms scale, using commercial stopped-flow devices,[43–46] as well as home-built CFDs[47] and liquid-jet assemblies[48–50] to analyze NC formation *in situ*. UV/Vis absorption spectroscopy,[43,45,46] as well as small-angle X-ray scattering (SAXS) and wide-angle X-ray scattering (WAXS) analysis[44,46–48,50,51] proved to be the most suitable characterization methods. All of these studies were limited to low temperature reactions, however, studying systems like gold,[44,46,47,51] CdS,[50] ZnS,[43,48] and PbS.[45]

Only in recent years have the *in situ* time-resolved studies of nucleation and growth been extended to high-temperature colloidal syntheses of NC systems like CdSe,[52,53] $Cu_{(2-x)}S$,[54] PbSe and PbS.[55] Of these studies, especially the works of Abécassis *et al.*, who tracked the formation reaction of CdSe QDs in a heat-up procedure within a capillary via *in situ* synchrotron SAXS and WAXS,[52] and the study by Maceiczyk *et al.*, who reported on the kinetics of CdSe growth in a microfluidic reactor,[53] have to be highlighted.

Both authors report the formation of CdSe QDs directly from the decomposing precursors without intermediates, growing continuously with reaction coordinate, and are able to formulate kinetic models pertinent to the respective reaction conditions.[52,53] While these models agree more or less well with the classical nucleation theory of crystallites, as applied to colloidal NCs, several authors have already reported evidence of magic-sized intermediates in the formation of NCs.[50,56–58] These MSCs, whose increased stability is postulated to be due to a closed shell of atoms,[56,59] have been reported to grow via a heterogeneous growth process from one magic size to the next in low-temperature syntheses of colloidal QDs.[60,61]

Considering the existence of these local energy minima in the chemical potential of small colloidal QDs, shown at low temperatures, it appears likely, that their formation can always occur via a growth mechanism including magic-sized intermediates, even at high temperature. In order to confirm this mechanism and gain insight into the kinetics of this process, via a time-resolved measurement, additional research is warranted.

2. Theoretical Background

2.1. Nanoscale Semiconductors

With regard to their electrical conductivity, bulk solids are typically classified as metals, semiconductors or insulators. Whereas metals conduct electrons intrinsically, semiconductors require some additional energy in order to become electrically conductive and insulators require a rather significant amount of energy, if they are to become electronically conductive. This behaviour results from the arrangement of the solid's atoms and its resulting electronic structure.

A typical bulk solid consists of a large number of atoms which are arranged periodically into a crystal lattice. In the simplest description, the free electron model, the electron wave can propagate without any interaction through the periodic potential of ions. This results in a complete delocalization of the electron wave function throughout the crystal.[62]

A more accurate description of the electron-ion interaction in a crystal lattice is given by the nearly free electron model. Electron waves meeting the Bragg condition (see section 2.2.2) will be reflected from the lattice and become standing waves. Depending on their previous propagation direction, they form one of two types of standing waves. The standing wave function $\psi(+)$, possessing its maxima at the coordinates of the positively charged ions, leads to a higher probability density of the electron near the ions. This leads to a decrease in potential energy compared to a completely delocalized electron. The opposite case of the wave function $\psi(-)$, having its minima at the coordinates of the lattice ions, and subsequently lowering the probability density of the electron at this position, leads to an increase in potential energy. The energy difference or gap E_g between both states is a forbidden energy zone, in which no wave-like solution of the Schrödinger equation exists.[62]

Another approach to describing the electronic structure of a bulk solid is the tight-binding model, which considers strongly localized electrons at the ionic cores that retain their properties during the formation of the bulk solid. This approach describes the electronic structure of the crystal as a linear combination of atomic orbitals (LCAO). In essence, the atomic orbitals of the constituting atoms are combined into molecular orbitals of the crystal. Due to the very large number of atoms in a bulk solid, the energy difference between the individual molecular orbitals becomes very small, resulting in an energetically more favorable quasi continuum of possible electronic states – an energy band. Depending on the energy of the original atomic orbitals, the resulting energy bands are separated by an energy gap. The highest occupied band is called the valence band, while the lowest unoccupied band is called the conduction band.[63]

The conduction behaviour of solids, as described in the beginning of this section, can be explained based on the size of this energy band gap, as well as the population of its bands. In a metal, the valence band is not fully populated, allowing for electron conduction in its empty orbitals. In an insulator however, electric conduction is strongly inhibited, as its valence band is fully populated and the size of its band gap prohibits excitation of electrons into the conduction band at normal temperatures. At $T = 0\,\mathrm{K}$ population of the bands in a semiconductor resembles that of an insulator. Since its band gap is smaller, thermal energy at higher temperatures is sufficient to excite electrons into the conduction band and thus increase the semiconductors conductivity. The energy required for the excitation of an electron into the conduction band in a semiconductor can also be introduced by an incident photon.[63,64]

Once an electron is excited into the conduction band, it leaves behind a positively charged hole in the valence band. Due to their Coulomb attraction, electron and hole form a quasi-particle called an exciton. Since this Coulomb interaction in most semiconductors is strongly screened by the valence electrons of the crystal, the exciton is only weakly bound. This type of exciton is called Wannier–Mott exciton (or Wannier exciton), which is opposed to strongly bound Frenkel excitons, which exist in ionic crystals.[65] The energy levels of the exciton can be calculated using the hydrogen model and the effective-mass approximation as:

$$E_{n,K} = E_g - \frac{\mu^* e^4}{32\pi^2\hbar^2\varepsilon^2\varepsilon_0^2}\frac{1}{n^2} + \frac{\hbar^2 K^2}{2(m_e^* + m_h^*)} \tag{2.1}$$

The first term in equation 2.1 is E_g, the band gap energy. In order to obtain the excitonic states' energy, the binding energy of the exciton is subtracted from it. The binding energy contains μ^*, the reduced effective mass of the effective masses of electrons (m_e^*) and holes (m_h^*), and ε the relative permittivity of the semiconductor material. The third term in the equation is the kinetic energy of the exciton's center of mass, which contains K, the wave vector corresponding to the center-of-mass motion of the electron and the hole.[63]

If the exciton is created by optical excitation, only excitonic states with $K \approxeq 0$ can be excited. In this case it becomes evident from equation 2.1, that the energy of an excitonic state is lower than the band gap energy, by the amount of the binding energy, as the kinetic term can be neglected. For that reason, electrons can be excited into excitonic states $E_{n,K}$ as they are located slightly below the edge of the conduction band in energy terms.[63] As excitons typically possess relatively low binding energies in bulk semiconductors, they are ionized easily into free charge carriers, i.e. electrons and holes. These can then recombine radiatively or nonradiatively.[66]

In the case of nanometer-sized semiconductor crystals, the dimensions of the crystal itself are on the order of magnitude of the Bohr radius of the exciton. This leads to a phenomenon called quantum confinement, in which causes an increase in minimum energy (confinement energy) and also a quantization of the crystals excited states.[65] Considering the fact, that, compared to bulk solids, NCs consist of only a small number of atoms, this quantization seems obvious, as the energy bands can not be considered continuous any more, but rather resembling molecular orbitals.[66]

In fact the confined exciton in a NC can be described using the quantum mechanical model of a particle in a box made of infinitely high potential barriers. Solving the Schrödinger equation for the particle in a spherical box yields its energy eigenvalues as

$$E_n = \frac{n^2 h^2}{8mR^2} \tag{2.2}$$

with m being the mass of the particle and L the length of the box. The equation shows a reciprocal correlation between the energy levels and the length of the box. Thus a smaller box results in higher energy differences between the states. Applied to a semiconductor NC this means, that the band gap energy increases with decreasing particle size. This phenomenon is called the quantum size effect.

The approach to calculate the energy eigenvalues of semiconductor NCs by application of the particle-in-a-box model has been used by Brus (amongst others) in the 1980s. He calculated the shift in energy difference between first excited state and ground state, i.e. the increase in band gap energy with reduction of particle size, by considering the excited state as a particle in a spherical potential well. His solution for the change in band gap energy is given in equation 2.3.[10,67]

$$E^* \simeq E_g + \frac{\hbar^2\pi^2}{2R^2}\left[\frac{1}{m_e} + \frac{1}{m_h}\right] - \frac{1.8e^2}{\varepsilon R} + \text{smaller terms} \tag{2.3}$$

In equation 2.3 E^* refers to the modified band gap energy, while E_g is the bulk band-gap energy. The second term is the quantum localization term, that describes the increase in band gap energy as a function of radius R^{-2}. The third term describes the Coulomb attraction between the electron and the hole, that decreases the band gap energy as a function of R^{-1}. The subsequent smaller terms contain the solvation energy term, which is a function of the crystal's as well as the surrounding medium's relative permittivity. It also scales with R^{-1} but has only a minor contribution to the resulting energy.[10,67]

In conclusion, semiconductor NCs possess a band gap in between their valence and conduction band. Through thermal or optical excitation an exciton can be formed, the energy of which is lower than the band gap energy. The exciton is confined due to the fact, that the crystal's size is similar to or smaller than the exciton's Bohr radius. This leads to a quantization of the energy states within the bands and more importantly to an increase in band gap energy with a decrease in crystal size, the quantum size effect. Nanoparticles exhibiting the quantum size effect are called quantum dots.[68]

2.2. Nanocrystal Characterization

Due to the significant interest in semiconductor NCs, a wide range of methods for their characterization has been developed over the last decades. Since the range of the NC's properties that can be characterized using these methods is probably even wider, this chapter will not attempt to give a comprehensive overview. Rather it will focus on the techniques used to characterize the NCs prepared in this work giving an overview of the underlying physics and the principles of measurement.

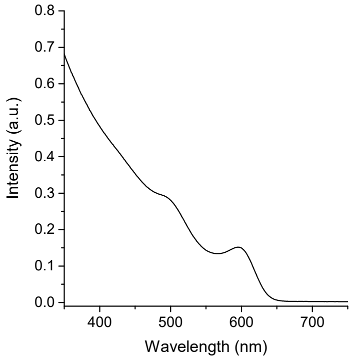

Figure 2.1.: Typical UV/Vis absorption spectrum of CdSe NCs prepared in this work.

2.2.1. Optical Spectroscopy

Absorption Spectroscopy

As was discussed in section 2.1, semiconductor NCs can absorb light, that has an energy corresponding to their band gap. This very useful characteristic makes UV/Vis absorption spectroscopy an excellent tool to characterize these so-called quantum dots. In UV/Vis absorption spectroscopy a sample's transmittance of monochromatic light as a function of the light's wavelength is measured. Typically, instead of the transmittance, absorbance, or optical density is given. These quantities are related according to Beer's law, which is shown in equation 2.4.

$$A_\lambda = -\log T_\lambda = -\log \frac{I}{I_0} = -\varepsilon c L \tag{2.4}$$

Equation 2.4 contains A_λ, the absorbance at a specific wavelength, T_λ, the transmittance at that wavelength, I, the light intensity, attenuated by the sample, I_0 the incident light intensity, ε the molar extinction coefficient of the chromophore, c the chromophore's concentration and L the optical path length. As is evident from Beer's law, both, the chromophore's concentration, as well as its molar extinction coefficient can be derived from its absorption spectrum.

As was discussed in section 2.1 quantum dots possess quantized electronic energy levels instead of the continuous bands observed in bulk semiconductors. Thus the absorption of light at energies corresponding to excitations into these energy levels can be observed in absorption spectra of quantum dots. Figure 2.1 shows a UV/Vis absorption spectrum of CdSe NCs prepared in this work. Both peaks in the spectrum result from electronic transitions into discrete excitonic energy levels of the quantum dots. The first peak at a wavelength of around 600 nm corresponds to the first excitonic transition, the excitation across the band gap of the quantum dot, while the second corresponds to a higher energy transition.[69,70]

The wavelength of this first excitonic peak can be used to determine the quantum dots' size for example by using Brus' equation (equation 2.3).[67] Another approach is the use of empirical sizing curves that have been published by Peng and co-workers and by Mulvaney and co-workers. Both groups have investigated the change in wavelength of the quantum dots' first excitonic absorption peak as a function of particle diameter and published the fit function to their experimental data.[71,72] As both sizing curves are in good agreement[72] the method published by Peng and co-workers was used to determine particle sizes in this work.

Additionally, the concentration of quantum dots in the sample can be determined, using the absorbance at the wavelength of the first excitonic absorption peak. According to Beer's law (equation 2.4), the molar extinction coefficient has to be determined, in order to calculate the concentration. Analogously to the sizing curves mentioned above, both Peng's group, as well as Mulvaney's group have published fit functions that describe their experimentally obtained correlation of the molar extinction coefficient at the wavelength of the first excitonic absorption peak with the quantum dot diameter. Both of their functions require a calibration using the half width at half-maximum (HWHM) of the first absorption peak, in order to consider the quantum dots' size distribution.[71,72]

Finally it has to be noted, that while, based on the particle-in-a-sphere model, a quantum dot should possess only discrete transitions, as long as the exciton is strongly confined, its electronic states actually approach a continuum state at higher energies.[73,74] This can be seen as some of their absorption properties become more bulk-like at energies far above the band gap and less influenced by size quantization effects.[75] Their intrinsic absorption coefficient, for example, becomes invariable to change in diameter[75] and their absorption cross section at 350 nm can be modelled using bulk optical constants.[76]

This results in homogeneous line broadening of the discrete absorption lines in quantum dot spectra, which results in continuum absorption at higher energies, as can be seen in figure 2.1. Additional contributions to homogeneous line broadening come from the temperature and the resulting coupling of electronic transitions to the crystallite's vibrational modes.[4] Homogeneous broadening alone however does not explain the significant discrepancy between the expected absorption lines for discrete transitions and the relatively broad peaks exhibited by the spectrum in figure 2.1. The most significant contribution to the peak width is the inhomogeneous broadening due to the quantum dots' size distribution.[4]

Photoluminescence Spectroscopy

The exciton formed after the absorption of light by a quantum dot is, compared to the electronic ground state, an energetically unfavorable state, which results in a recombination of electron and hole by the fastest possible pathway. The energy difference between excited state and ground state is typically released from the crystal in a process called photoluminescence (PL) under emission of a photon.[64]

PL spectra of quantum dots typically show a relatively narrow peak which is centered at a wavelength shifted to lower energy compared to the first excitonic absorption peak by the so-call Stokes-shift.[77] This nonresonant PL is called fluorescence and is explained through the application of the Franck–Condon principle. The excitation initiated by the absorbed photon occurs from the electronic ground state into the electronic excited state. Due to the vastly different masses of atomic nuclei and electron, the nuclei take longer to rearrange into the equilibrium geometry of the electronic excited state than it takes for the electronic transition to occur. Because of this, the system ends up in a higher vibronic energy state within the electronic excited state.[78] Subsequently relaxation to the vibronic ground state of the electronic excited state occurs, before the relaxation to the electronic ground state takes place under emission of a photon. The emitted photon's energy reduction (or Stokes-shift) compared to the absorbed photon is, among other parameters, correlated to the number of vibronic states involved in the relaxation process.[77]

Due to their very large surface-to-volume ratio, the optical properties of quantum dots are strongly influenced by their surface. In consequence their PL efficiency, defined by the so-called PL quantum yield (QY)[1], is often greatly reduced due to trap states located at the NCs' surface. The concentration of these trap states, which are typically a result of interstitial atoms, impurities, dislocations and defects,

---

[1] PL QY: the ratio of emitted photons to absorbed photons[64]

is higher there, due to the different bonding situation compared to the volume.[66] The trap states often offer fast non-radiative relaxation pathways for the system, that compete with the PL pathways and thus reduce the PL QY. While a portion of the surface is already passivated due to the ligands bound to the surface atoms, the most efficient method for surface passivation and increase of the PL QY is the coating of the NC with another semiconductor material. The resulting core/shell quantum dots can reach PL QYs of up to 100 %.[79,80]

Experimentally quantum dot PL spectra are typically obtained by measuring the emitted light intensity from a quantum dot sample at a right angle from the incident monochromatic excitation light as a function of the wavelength. A special case of PL measurement is the photoluminescence excitation (PLE) experiment. In this experiment, the intensity of the emitted light at a specific wavelength is measured as a function of the excitation wavelength. With this measurement technique, it is possible to determine the transitions in the absorption spectrum that lead to a specific feature in the PL spectrum.

2.2.2. X-ray Scattering

X-ray scattering techniques are among the oldest methods for structure determination in solids. Von Laue and co-workers found diffraction patterns when irradiating a crystal of $CuSO_4$ with X-rays in 1912 and with this discovery founded the field of X-ray crystallography.[81] While the experimental techniques have developed significantly since then, the method of X-ray diffraction is still one of the most useful crystallographic techniques. Apart from macroscopic single crystals it can also be used on polycrystalline samples, like powders of microscopic crystallites. This corresponding technique is called X-ray powder diffraction (XRD) and is the subject of the first part of this section.

The second part of this section will focus on SAXS where the X-ray intensity at angles close to the primary beam is investigated. This technique is highly useful for the investigation of colloidal quantum dot samples, as the length scales investigated are on the order of magnitude of typical quantum dot diameters.

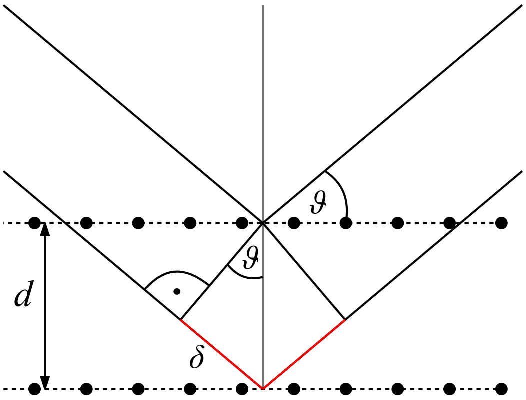

Figure 2.2.: Reflection of parallel X-rays at a family of lattice planes. Constructive interference is only possible if the difference in path length of the incident waves δ is an integer multiple of their wavelength.

X-ray Powder Diffraction

X-rays incident on a crystal are scattered elastically by the crystal's atoms' valence electrons. Since the bond lengths' between the crystal's atoms are on a similar length scale as the wavelength of X-rays, interference between the scattered waves can be observed. The incident X-rays are diffracted by the crystal's lattice.[82]

Analogous to the pattern resulting from the diffraction of a visible light beam by an optical diffraction grating, diffraction of an X-ray beam by a crystal lattice produces a unique pattern of bright spots. These are the result of constructive and destructive interference of the X-rays which are reflected at different lattice planes. Figure 2.2 shows a schematic drawing of parallel X-rays being reflected at a family of lattice planes of a two-dimensional crystal. A path difference of $2 \cdot \delta$ between the two X-rays reflected at the two planes results from to the lattice spacing d. In order for constructive interference to occur between the two waves, i.e. for them to be in phase after being reflected, their path difference needs to be an integer multiple of their wavelength λ.[82]

$$n \cdot \lambda = 2 \cdot \delta \tag{2.5}$$

Application of the law of sines yields $\delta = d \cdot \sin \vartheta$. So equation 2.5 becomes

$$n \cdot \lambda = 2d \cdot \sin \vartheta \tag{2.6}$$

According to equation 2.6 a reflection at a family of lattice planes with lattice spacing d only leads to constructive interference at a specific angle ϑ. Equation 2.6 is known as Bragg's law, named after W.H. Bragg and W. L. Bragg, who first published it in 1913.[83]

The diffraction pattern obtained from a powder of statistically oriented crystallites, e.g. an ensemble of NCs, varies considerably from the one obtained from a single crystal. While in a single crystal sample only the lattice planes determined by Bragg's law show a discrete spot in the diffraction pattern, in the powder case all lattice planes contribute to the diffraction pattern. This is the case, as, due to the statistic orientation and the vast number of crystallites, a statistically significant number of each planes fulfils Bragg's condition at any time. This results in a smeared-out diffraction pattern, which is showing circles instead of discrete spots.[84]

Equation 2.6 shows the reciprocal relation between ϑ and d. As a consequence, small features, like lattice planes in crystals (d on the order of hundreds of pm) , appear at large scattering angles, compared to relatively large objects, like nanoparticles (d on the order of a few nm). Due to that and in order to better differentiate XRD from small-angle X-ray scattering it is sometimes also referred to as wide-angle X-ray scattering.

Small-angle X-ray Scattering

Small-angle X-ray scattering is a measurement technique used for the characterization of colloidal sized objects, e.g. colloidal NCs. The dimensions of such particles ($\geq 1\,\mathrm{nm}$) are at least an order of magnitude larger than the wavelength of the X-rays used in the experiment ($\sim 100\,\mathrm{pm}$). Due to the reciprocal relation between length scale and scattering angle (equation 2.6), scattering intensity from these structures can be observed at angles close to zero scattering angle.[85]

Since the scattering of the X-ray waves at small angles is almost always coherent, the waves scattered at zero scattering angle are exactly in phase, which leads to maximum scattering intensity. As was discussed in the previous sections, waves scattered at large angles, that do not comply with Bragg's condition (equation 2.6), are cancelled out due to destructive interference with another wave possessing a phase shift of exactly $\frac{\lambda}{2}$. At small angles, the phase difference between the scattered waves naturally becomes smaller, which causes some constructive interference to

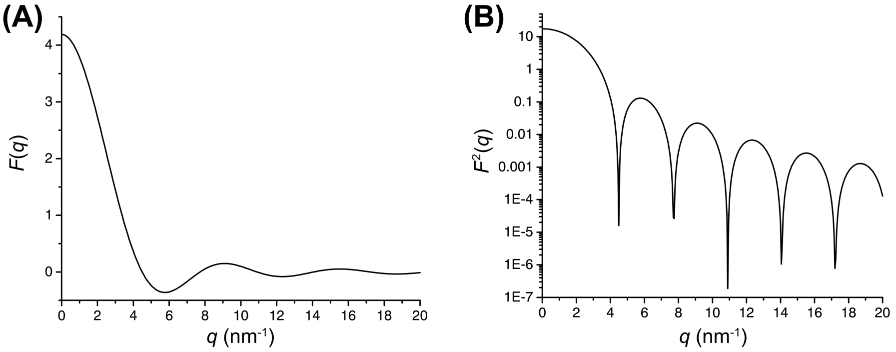

Figure 2.3.: Plot of the small angle scattering amplitude $F(q)$ (A) and $F^2(q)$ (B) for spherical particles with radius of 1 nm, given by equation 2.8.

occur. Hence, there is a continuous scattering intensity at small scattering angles, which decreases with increasing scattering angle.[85]

For the further description of SAXS it is necessary to introduce the scattering vector q. If a monochromatic plane wave with wave vector k_0 and $|k_0| = \frac{2\pi}{\lambda}$ is scattered elastically, the magnitude of the scattered wave vector is $|k_1| = |k_0|$. Following the Fourier transform from real space to reciprocal space the difference between the two vectors is the scattering vector $q = k_1 - k_0$. It can be related to the scattering angle 2ϑ, which is the angle between k_1 and k_0 by[86]

$$q = \frac{4\pi \sin\vartheta}{\lambda} \tag{2.7}$$

As scattering occurs due to electronic oscillation, the total scattered amplitude $F(q)$ depends on the particle's electron density, i.e. the number of electrons per unit volume, $\rho(r)$. As the particle's solvent also possesses a constant electron density ρ_s, the electron density difference $\Delta\rho(r) = \rho(r) - \rho_s$ has to be considered. $F(q)$ is the Fourier transform of $\Delta\rho(r)$. $F(q)$ is related to the scattering intensity $I(q)$, which is measured during a scattering experiment, by $I(q) = F(q)F^*(q)$.[86]

Assuming a spherical particle shape, $I(q)$ can simply be determined by squaring the amplitude, as all orientations in space are equivalent. It can then be expressed as

$$I(q) = F^2(q) = (\Delta\rho)^2 V^2 \left[3\frac{\sin(qr) - qr\cos(qr)}{(qr)^3}\right]^2 \tag{2.8}$$

with the particle volume $V = \frac{4}{3}\pi r^3$.[85] The evolution of $F(q)$ with q is plotted in figure 2.3 (A) together with $F^2(q)$ (B) for a spherical particle with a radius of 1 nm. For the sake of simplicity, an electron density difference of $\Delta\rho = 1$ has been used for the plot. The shape of these curves illustrates the typical oscillating behavior of SAXS patterns.[85]

In an ensemble of identical particles, two limiting cases of particle distribution, which strongly affect the scattering, have to be considered. The particles can be arranged in an ideal single crystal like a NC superlattice. In this case, there is constructive and destructive interference from the scattered waves and the $I(q)$ measured will exhibit Bragg peaks, analogous to WAXS signals.[86]

In the other limiting case the particles don't interact with each other, are distributed randomly and neither their positions, nor their orientations are correlated. In this case the scattered intensities, rather than their amplitudes, can be summed up, as there is no interference. The scattering intensity is then the single particle intensity averaged over all orientations.[86] This type of behaviour can be assumed for dilute solutions of monodisperse NCs.[87] For polydisperse samples, the scattering intensity is given by the weighted average of the scattering from all types of particles in the sample.[86]

At very small angles the shape of the scattering pattern of an ideal monodisperse sample of non-interacting particles can be described by the Guinier approximation

$$I(q) = (\Delta\rho)^2 V^2 \exp\left(-\frac{q^2 R_g^2}{3}\right) \tag{2.9}$$

with R_g being the radius of gyration, which is the root-mean square of the distances of all electrons from their center of gravity.[85] In a so-called Guinier plot ($\ln(I(q))$ versus q^2) a linear function is obtained, from the slope of which R_g can be determined. This plot can also be used as a test for sample polydispersity and particle interactions. The Guinier approximation is only valid in a range of $q < 1.3/R_g$.[86]

At larger angles $I(q)$ can be described by Porod's law, using a power series. An approximation is given by

$$I(q) \rightarrow (\Delta\rho)^2 \cdot \frac{2\pi}{q^4} \cdot S \tag{2.10}$$

with S being the particle's surface. Using the so-called Porod invariant ($Q =$

$2\pi^2(\Delta\rho)^2V$ for homogeneous particles) yields

$$\frac{S}{V} = \frac{\pi}{Q} \lim_{q\to\infty}[I(q)q^4] \tag{2.11}$$

with $\frac{S}{V}$ being the particle's specific surface. This allows the determination of the specific surface directly from the scattering pattern.[85,86] In real samples, internal inhomogeneities often cause deviation from Porod's law, requiring additional correction.[86]

The analysis of real SAXS patterns typically requires the development of a model particle, that fits the experimentally obtained scattering pattern. This is due to the fact, that real samples rarely are monodisperse, perfectly spherical and ideally dilute. Although this can be a tedious process, the wide variety of information that can be gleaned from the analysis makes it worthwhile. Considering the fact, that the investigated length scale makes the technique ideal for characterizing colloidal samples, it is of no surprise, that it has been widely used in the literature, to investigate the formation of colloidal NCs.[42,44,47,48,51,52,88–92]

2.2.3. Transmission Electron Microscopy

Due to their very small size, imaging of nanostructures using a conventional light microscope is not possible. Since the resolution of a microscopy technique is limited by the diffraction limit to approximately half the wavelength of the radiation used to illuminate the sample, it is necessary to use higher energy radiation than visible light to image nanostructures. An ideal candidate for this is a beam of electrons accelerated in an electric field. Using acceleration voltages on the order of several hundred Kilovolts, the wavelength of the electrons becomes sufficiently small to resolve nanostructures.

The setup of a transmission electron microscope (TEM) is in principle analogous to an optical microscope: it possesses a light source and a series of lenses that focus the light on the sample and later magnifies it onto a screen. As a light source, a TEM typically uses either a thermionic or field emitter electron gun. In a thermionic gun, electrons are liberated from a material possessing a relatively low work function (e.g. LaB_6) by applying sufficiently high thermal energy. In a field emitter gun, a very strong electric field is applied to a tungsten needle in order to lower the work function, allowing electrons to tunnel out of the needle. In both gun types, the electrons are then extracted, focused and accelerated into the electron beam by an anode assembly.[93]

As opposed to an optical microscope, a TEM uses magnetic lenses to manipulate the electron beam. Their housing, the TEM column, is under high vacuum in order to prevent oxidation of the emitter and scattering of the electron beam from gas molecules. The column contains a condenser system, consisting of two lenses and an aperture that parallelizes the beam onto the sample. The imaging system, consisting of objective, intermediate and projector lens, as well as several apertures, magnifies and projects the image of the sample onto a scintillating screen (typically coated in ZnS), or a CCD camera. By adjusting the intermediate lens and aperture, as well as removing the objective aperture, it is possible to select between imaging and diffraction mode. In diffraction mode, it is possible to obtain a diffraction pattern of electrons, diffracted by the sample, analogous to the pattern formed by X-rays diffracted from a crystal lattice.[93]

The contrast in a TEM image is generally formed by three processes: scattering, diffraction and interference between transmitted and diffracted electrons. Scattering contrast results from electrons scattered by the atoms in the sample. The thicker an object in the sample is, i.e. the more layers of atoms there are, the darker the object appears on the screen. Diffraction contrast results from diffraction of the electrons from the crystal lattice of the sample. Since the wavelength of the electrons in a TEM is on an order of magnitude with X-rays, they can also be diffracted from crystal lattices, if the Bragg condition is met. Crystalline objects in a sample, that have lattice planes oriented in a Bragg angle to the incident electron beam thus appear darker on the screen. Lastly the interference of diffracted electrons with transmitted electrons due to their phase difference results in the so-called phase contrast. The phase contrast enables the imaging of a crystal's lattice planes in high resolution TEM.[93]

Apart from imaging sample structures directly or imaging their diffraction patterns, there are a multitude of other possibilities to gain information about the sample through use of a TEM. By making use of inelastic scattering of electrons by atomic cores within the sample, it is also possible to detect its elemental composition. This can be done by using an electron energy-loss spectrometer (EELS) to detect the electrons that have lost energy to core electrons in the sample through inelastic scattering. Combining this spectrometry technique with scanning TEM (STEM[2]) allows chemical mapping of the sample, showing the variations of chemical composition over the acquired image. Another approach to measure the chemical composition of the sample is energy-dispersive X-ray spectrometry (EDX). Equipping the TEM with an EDX detector allows the detection of characteristic X-rays emitted by the decay of a "core hole" after a core electron has been excited from the atom by incident electrons.[94]

2.3. Colloidal Synthesis of Semiconductor Nanocrystals

Preparation methods of nanostructures are generally divided into top-down and bottom-up procedures. Top-down procedures are based on the creation of nanometer-sized structures through the application of nanopatterning techniques on larger scale materials, for example nanoparticles obtained from milling of microparticles[95], or nanoscale optical resonators obtained through lithography and etching of bulk semiconductor material.[96] Bottom-up procedures, on the other hand, are based on the aggregation of molecular, ionic, or atomic species into nanoscale structures. This can be for example semiconductor thin films grown via molecular beam epitaxy,[97] the growth of carbon nanotubes via chemical vapor deposition,[98] or the colloidal synthesis of semiconductor NCs.[99]

Due to its numerous advantages, colloidal synthesis has developed into the number one synthetic route to obtain high-quality NCs in the last decades.[30,31,66,87,99–103] Its principles will be discussed in the following section, together with procedures to influence the NC size distribution. Finally, an introduction to magic-sized semiconductor clusters will be given.

2.3.1. Nucleation and Growth of Colloidal Nanocrystals

LaMer Model of Nucleation

The term colloidal NCs generally refers to solution-grown inorganic NCs stabilized in a solvent phase by surfactant molecules, also called ligands, bound to their surface.

---

[2] STEM: The electron beam is focused into a small probe and scanned across the sample.

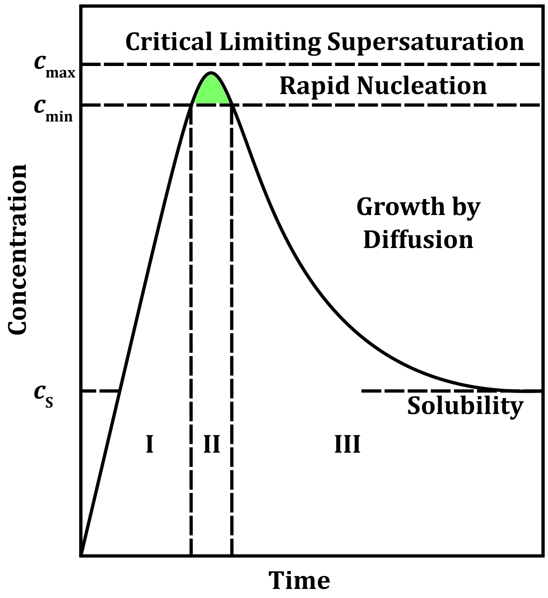

Figure 2.4.: LaMer plot of monomer concentration evolution with time during nucleation and growth of NCs. Nucleation takes place in the highlighted area. Adapted from LaMer *et al.*.[104]

They are formed from precursors, which decompose into reactive monomers under reaction conditions, by a two-step process: nucleation of initial crystallization seeds and subsequent growth of these nuclei into NCs.[100]

The nucleation behaviour of colloidal particles is illustrated by the so-called LaMer diagram, which was published by LaMer and Dinegar in 1950.[104] The diagram, which is shown in figure 2.4, is a plot of the concentration of the particles' monomers as a function of time. Upon initiation of precursor-to-monomer conversion, stage I, the monomer concentration build-up begins. The passing of the monomer's solubility (c_{S}) by the increasing monomer concentration causes no precipitation but instead the solution becomes supersaturated. The supersaturation increases together with the monomer concentration, until a critical minimum concentration of nucleation (c_{min}) is reached. At this point, nucleation (stage II) begins.[105]

While initially the nucleation rate is relatively low, it increases quickly with increasing monomer concentration until it can be considered infinite. At this point, all newly generated monomer is immediately consumed either through nucleation or by incorporation into growing nuclei, causing the monomer concentration to decrease

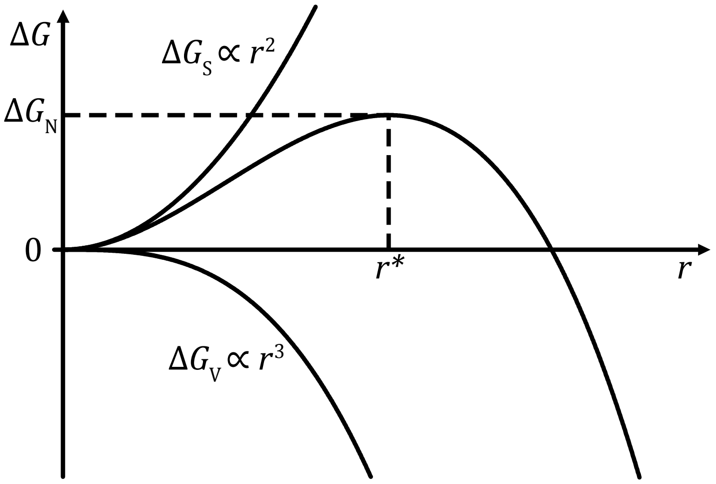

Figure 2.5.: Plot of free energy (ΔG) as a function of particle radius (r) according to classical nucleation theory. In addition, the surface (ΔG_{S}) and volume (ΔG_{V}) contribution to ΔG, critical radius (r^*), and activation energy of nucleation (ΔG_{N}) are shown.

back below c_{min}. With this partial relief of supersaturation the nucleation stage ends and all free monomer is now consumed by growth of the previously formed nuclei (stage III).[104]

Classical Nucleation Theory

Nucleation causes the formation of new surface around newly formed volume. As such, the free energy of a nucleus of radius r, $\Delta G(r)$, is the sum of the free energy increase through surface formation, ΔG_{S}, and the free energy decrease through volume formation, ΔG_{V}. Since classical nucleation theory assumes the nuclei to be spherical, ΔG_{S}, ΔG_{V} and $\Delta G(r)$ are given by

$$\Delta G_{\mathrm{S}} = 4\pi r^2 \gamma \tag{2.12}$$

$$\Delta G_{\mathrm{V}} = -\frac{4}{3}\pi r^3 \frac{RT \ln S}{V_{\mathrm{m}}} \tag{2.13}$$

$$\Delta G(r) = 4\pi r^2 \gamma - \frac{4}{3}\pi r^3 \frac{RT \ln S}{V_{\mathrm{m}}} \tag{2.14}$$

respectively. In equation 2.14 γ is the surface energy, R, T and V_{m} are the ideal gas constant, temperature and molar volume of the bulk monomer respectively.[106] S is the supersaturation given by $S = \frac{[\mathrm{M}]}{[\mathrm{M}]_\infty}$ with [M] being the monomer concentration and $[\mathrm{M}]_\infty$ being the equilibrium monomer concentration of the bulk solid.[102]

Figure 2.5 shows a plot of $\Delta G(r)$ versus r together with the surface and volume contributions, ΔG_S and ΔG_V. At very small radii, $\Delta G(r)$ is dominated by the surface term, which makes the existence of nuclei with such radii energetically unfavorable and causes them to dissolve. At radii larger than the critical radius r^*, the volume term becomes dominant and the slope of $\Delta G(r)$ becomes negative. As a result, nuclei with radii larger than r^* grow by incorporation of additional monomer. The value of r^* can be determined by setting $\frac{\mathrm{d}\Delta G}{\mathrm{d}r} = 0$ at $r = r^*$ and obtaining[102]

$$r^* = \frac{2\gamma V_\mathrm{m}}{RT \ln S} \tag{2.15}$$

The maximum of the free energy curve at r^* is equal to the thermodynamic barrier, or activation energy for the formation of stable nuclei ΔG_N. It is given by

$$\Delta G_\mathrm{N} = \Delta G(r^*) = \frac{16\pi\gamma^3 V_\mathrm{m}^2}{3R^2T^2(\ln S)^2} \tag{2.16}$$

The formation rate of nuclei can then be written in the Arrhenius form as

$$\frac{\mathrm{d}N}{\mathrm{d}t} = A \exp\left[-\frac{\Delta G_\mathrm{N}}{k_\mathrm{B}T}\right] = A \exp\left[-\frac{16\pi\gamma^3 V_\mathrm{m}^2}{3k_\mathrm{B}^3 T^3 N_\mathrm{A}^2 (\ln S)^2}\right] \tag{2.17}$$

with N, A, k_B, and N_A being the number of nuclei, the pre-exponential factor, Boltzmann's constant, and Avogadro's number respectively. The nucleation rate can be influenced experimentally by adjusting the supersaturation, temperature and surface free energy. It is most strongly influenced by the supersaturation however, which makes this parameter most useful in controlling the NC size distribution, as will be discussed in section 2.3.2.[102]

Diffusion- versus Reaction-controlled Growth

Subsequent to the formation of stable nuclei in the nucleation stage, the nuclei grow by incorporating free monomer. For this to occur, the monomer first needs to be transported through a diffusion layer of thickness δ, which surrounds the particle. This mass flow J through a spherical diffusion layer with radius x (from the particle's center) can be described by Fick's first law of diffusion as

$$J = 4\pi x^2 D \frac{\mathrm{d[M]}}{\mathrm{d}x} \tag{2.18}$$

with D being the diffusion coefficient.[105] [M] is at its lowest value $[\mathrm{M}]_\mathrm{s}$ at the particle surface ($x = r$), where the growth reaction occurs, and rises throughout the diffusion layer until it reaches the bulk monomer concentration of the solution $[\mathrm{M}]_\mathrm{b}$ at $x = r + \delta$.[102] Integration of [M] with respect to x in the limits of r and $r + \delta$ yields

$$J = \frac{4\pi D r(r+\delta)}{\delta}([\mathrm{M}]_\mathrm{b} - [\mathrm{M}]_\mathrm{s}) \tag{2.19}$$

Due to the mass balance, the monomer consumption rate of a first-order surface reaction is equal to J and can be described as

$$J = 4\pi r^2 k([\mathrm{M}]_\mathrm{s} - [\mathrm{M}]_\mathrm{r}) \tag{2.20}$$

with $[\mathrm{M}]_\mathrm{r}$ being the solubility of the particle as a function of its radius and k the rate constant of the surface reaction. J is related to the rate of the particle volume change $\frac{\mathrm{d}r}{\mathrm{d}t}$ by

$$J = \frac{4\pi r^2}{V_\mathrm{m}} \frac{\mathrm{d}r}{\mathrm{d}t} \tag{2.21}$$

Combining equations 2.19 and 2.20 yields

$$\frac{([\mathrm{M}]_\mathrm{s} - [\mathrm{M}]_\mathrm{r})}{([\mathrm{M}]_\mathrm{b} - [\mathrm{M}]_\mathrm{s})} = \frac{D}{kr}\left(1 + \frac{r}{\delta}\right) \tag{2.22}$$

Particle growth can be divided into two different growth modes, based on the ratio of $\frac{D}{kr}$ in equation 2.22. If $\frac{D}{kr} \ll 1$, the diffusion step becomes the rate-determining step in the growth reaction whereas every unit of monomer, that is transported through the diffusion layer, reacts immediately in the surface reaction. In this case of diffusion-controlled growth $[\mathrm{M}]_\mathrm{s} \simeq [\mathrm{M}]_\mathrm{r}$ and, according to equations 2.19 and 2.21, $\frac{\mathrm{d}r}{\mathrm{d}t}$ becomes

$$\frac{\mathrm{d}r}{\mathrm{d}t} = D V_\mathrm{m} \left(\frac{1}{r} + \frac{1}{\delta}\right)([\mathrm{M}]_\mathrm{b} - [\mathrm{M}]_\mathrm{r}) \tag{2.23}$$

resulting in a decrease of $\frac{\mathrm{d}r}{\mathrm{d}t}$ with increasing r. In consequence, for constant

$([\mathrm{M}]_\mathrm{b} - [\mathrm{M}]_\mathrm{r})$, particle-size distribution narrows, as smaller particles grow faster than larger ones.[105]

For $\frac{D}{kr} \gg 1$ the surface reaction becomes the rate-determining step and thus $[\mathrm{M}]_\mathrm{b} \simeq [\mathrm{M}]_\mathrm{s}$. In this reaction-controlled growth mode, $\frac{\mathrm{d}r}{\mathrm{d}t}$ can be obtained from equations 2.20 and 2.21 as

$$\frac{\mathrm{d}r}{\mathrm{d}t} = kV_\mathrm{m}([\mathrm{M}]_\mathrm{b} - [\mathrm{M}]_\mathrm{r}) \tag{2.24}$$

In this case, the growth rate is independent of the particle size and the size distribution remains unchanged, as long as $([\mathrm{M}]_\mathrm{b} - [\mathrm{M}]_\mathrm{r})$ is constant.[105]

The Gibbs–Thomson Effect

In order to accurately describe the growth dynamics of colloidal nanoparticles it has to be considered, that their solubility $[\mathrm{M}]_\mathrm{r}$ is a function of particle radius and thus $([\mathrm{M}]_\mathrm{b} - [\mathrm{M}]_\mathrm{r})$ is not in fact constant. The chemical potential μ of a spherical particle with radius r is increased by

$$\Delta\mu = \frac{2\gamma V_\mathrm{m}}{r} \tag{2.25}$$

according to the Gibbs–Thomson relation. As a consequence, a very small particle can have a chemical potential higher than that of its monomers, which results in a dissolution of the particle. A larger particle, with a chemical potential lower than that of its monomers, on the other hand, will grow.[102] The particle's size-dependent solubility $[\mathrm{M}]_\mathrm{r}$ can be expressed as

$$[\mathrm{M}]_\mathrm{r} = [\mathrm{M}]_\infty \exp\left(\frac{2\gamma V_\mathrm{m}}{rRT}\right) \tag{2.26}$$

For $\frac{2\gamma V_\mathrm{m}}{rRT} \ll 1$ the diffusion-controlled growth rate becomes

$$\frac{\mathrm{d}r}{\mathrm{d}t} = K_\mathrm{D}\left(\frac{1}{r} + \frac{1}{\delta}\right)\left(\frac{1}{r^*} - \frac{1}{r}\right) \tag{2.27}$$

with $K_\mathrm{D} = \frac{2\gamma D V_\mathrm{m}^2 [\mathrm{M}]_\infty}{RT}$ and r^* the critical radius at which the solubility of the nanoparticle equals the monomer concentration in solution and the growth rate is zero. Particles with $r < r^*$ are thermodynamically unstable and dissolve, while particles with $r > r^*$ grow.[40] The value of r^* depends on the level of supersaturation

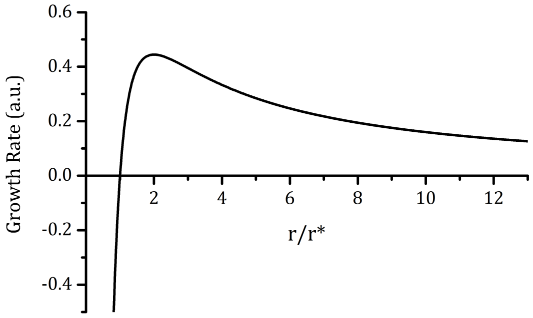

Figure 2.6.: Particle growth rate according to equation 2.27 versus particle radius relative to r^* with $K_\mathrm{D} = 1$.

S according to equation 2.15. A plot of equation 2.27 versus the particle radius relative to r^* with $K_\mathrm{D} = 1$ is shown in figure 2.6. The particle growth rate increases with r for $r \lesssim 2r^*$ and decreases again for larger r. As a consequence, as long as the supersaturation is sufficiently high, smaller particles with $r \gtrsim 2r^*$ grow faster than larger particles, and the particle-size distribution narrows during growth.[105]

With a decreasing level of supersaturation the critical radius shifts to larger values until it reaches the average radius $\tilde{r}$ of the particle ensemble. In this case, smaller particles become unstable, shrink and eventually dissolve, while larger particles keep growing by incorporating the newly available monomer. This process, that leads to a defocusing of the size distribution, is called Ostwald ripening.[40]

A similar observation can be made for the reaction-controlled growth mode. The closer the system is to the reaction-controlled regime (i.e. with increasing ratio $\frac{D}{k}$) the less dependent the growth rate is on the particle radius, i.e. no size-focusing regime exists. As a consequence Ostwald ripening is observed and the size distribution broadens with increasing reaction time.[35]

2.3.2. Controlling Nanocrystal-Size Distribution

Since many properties of NCs are defined by their size, precise control over their size distribution during synthesis is crucial. This can be achieved by a variety of methods, of which two major approaches will be discussed here: burst nucleation and the consequential separation of nucleation and growth, and size focusing. Both approaches rely on controlling the supersaturation level in order to control the particle-size distribution.

As described by LaMer's model, which was discussed in section 2.3.1, nucleation occurs at a high supersaturation level with monomer concentrations above the critical minimum concentration of nucleation. New nuclei form and begin growing until the monomer concentration drops below the critical level. In the ideal case all particles nucleate at the same point in time, grow under the same conditions and subsequently reach the same size after a given reaction time. While this is hardly possible for homogeneous nucleation, a sufficient approximation can be reached by limiting the nucleation stage (stage II in figure 2.4) to as short an amount of time as possible. For this purpose, the monomer concentration has to be increased high above the critical level instantaneously, so that the nucleation rate becomes effectively infinite. Free monomer is then rapidly consumed by nucleation until the supersaturation drops below the critical level again. In this case of burst nucleation, nucleation occurs so rapidly, that it is effectively separated from growth.

The principle described above has been utilized by Bawendi and co-workers in their groundbreaking method for the synthesis of nearly monodisperse cadmium chalcogenide NCs. Their synthetic approach, which was later dubbed the hot-injection synthesis, relies on rapid injection of precursor solutions into a hot coordinating solvent, which leads to immediate burst nucleation. The accompanying rapid monomer consumption and the temperature drop due to the injection limit the nucleation stage and allow slow growth of nanoparticles with a narrow size distribution.[99]

Within the last two decades the hot-injection method has been constantly adapted and improved. Not only regarding the synthesis of cadmium chalcogenide NCs but also for a multitude of other materials. Using the hot-injection method it is possible to obtain uniform NCs of cadmium, zinc, and lead chalcogenides, III-V semiconductors like indium phosphide and arsenide, as well as metals like iron, cobalt and cobalt platinum.[101]

As was discussed in the previous section (2.3.1), smaller particles tend to grow faster than larger particles and the particle-size distribution narrows with elapsing reaction time as long as the supersaturation is sufficiently large. As this size-focusing effect is strongly tied to the level of supersaturation, defocusing of the size distribution can be averted by replenishing the monomer used up during the reaction and thus keeping the supersaturation level high. Additional injections of monomer during the growth phase even allow the refocusing of a particle-size distribution which has already defocused through Ostwald ripening. Ideally replenishment of monomer keeps the supersaturation at a level where the critical size remains smaller than the average particle size at all time, while avoiding additional nucleation.[40]

2.3.3. Magic-Sized Clusters

For the last 30 years authors have published evidence of very small semiconductor NCs, which occurred in the early stages of colloidal NC syntheses and possessed atypically narrow UV/Vis absorption peaks, indicating a near-uniform particle size.[50,56,58,107–110] Direct synthesis protocols were quickly developed and allowed very reproducible synthesis of certain defined sizes of these nanoclusters.[60,111–116]

Further study of the nanoclusters' growth behaviour showed that, unlike regular NCs, they do not grow continuously but instead only exist in discrete sizes. Growth occurs by variation in the population of clusters of different sizes. The population of a cluster of a certain size will increase initially and then decrease in favor of that of a larger cluster, in a type of sequential, or quantized growth process.[60,61,108,112,115,117]

A general mechanism which explains the sequential growth of MSCs has not yet been established. Several authors propose the initial formation of one cluster and subsequent growth by cluster-cluster aggregation.[50,115,118] Others report the growth of clusters by incorporation of free monomer, analoguously to regular NCs, with smaller clusters being unable to dissolve or shrink due to their high stability.[60,61] There are also reports of dissolution of smaller clusters and incorporation of thusly liberated monomer into others to form larger clusters.[57]

The substantial thermodynamic stability which can be deduced from their growth behaviour has coined the term MSCs, in analogy to closed-shell metallic gas-phase clusters.[117] The existence of these MSCs is contradictory to the predictions resulting from classical nucleation theory (section 2.3.1) and the Gibbs–Thomson equation (section 2.3.1) which assume a continuous behaviour of the free enthalpy during the formation of NCs (compare figures 2.5 and 2.6). A modification of these theories through the introduction of local free enthalpy minima reflecting the thermodynamic stability of MSCs becomes necessary. Growth of the clusters would then occur slowly, given sufficient monomer concentration/temperature, by passing of an energy barrier to allow formation of a larger cluster. Similarly dissolution of a cluster would occur slowly, if the monomer concentration was lower than the cluster's solubility.[119]

It has to be noted, that these clusters do not represent critical nuclei as predicted by classical nucleation theory, whose growth to larger size would have to occur very rapidly.[119] MSCs rather exist in sizes below the critical radius,[120] illustrated by the unprecedentedly small sizes at which they have been produced. This is further supported by the fact, that the energy required for their formation is significantly lower than the energy barrier for nucleation of regular NCs, as their synthesis has been reported at temperatures below 100 °C[60,110,113,115] down to room temperature.[57] This is well below typical reaction temperatures required for the formation of regular NCs ($\geq$ 200 °C[99,121]).

Some authors suggest, that the formation of regular NCs from MSCs requires dissolution of the MSCs to release sufficient monomer for the NCs' nucleation. The MSCs then act as a monomer reservoir, for example during the formation of CdSe nanorods[109] and InP quantum dots, for which they can be used as a single-source precursor.[58]

A generalized description of the growth behavior and the role of MSCs in the formation of regular NCs is made difficult by the fact, that the stability of a certain MSC or certain groups or families of MSCs has been reported to be strongly influenced by the reaction conditions and especially the composition of the reaction medium.[112–114,117,118] Accordingly, a selection for specific families MSCs and between the formation of MSCs and regular NCs through a variation of the ligand environment has been reported.[112,113,118]

3. Scope

The aim of this project was the time-resolved investigation of nucleation and growth of colloidal semiconductor NCs, with specific attention to the role of MSCs during NC development. For this purpose, a CFD was to be developed and set up based on the layout of preparative reactors developed by Jan Niehaus, Daniel Neß, Katharina Poulsen and Tobias Jochum in their respective PhD theses.[122–125]

The time resolution was to be attained through the use of defined-length heated delay lines and subsequent quenching of the reaction. Characterization of the forming NCs was to be done using a UV/Vis absorption spectrometer, connected to the flow system. The online recording of absorption spectra was to enable direct tracking of the size and concentration evolution of the NCs.

To enable the use of synchrotron-based X-ray scattering techniques for *in situ* NC characterization, the setup was to be adapted for the use at synchrotron beamlines by the development and construction of a specialized heatable X-ray flow cell.

Based on these technical developments, the NC formation reaction was to be studied in the CFD. CdSe was selected as a model system, due to the extensive empirical knowledge about its nucleation and growth dynamics and the ease of its characterization using optical spectroscopy, due to its band gap in the visible range.

In a first step, a suitable precursor system for the CdSe synthesis in the CFD was to be found, as the reaction rate had to fit the attainable time resolutions of the device. Subsequently, the influence of nucleation and growth temperature, and reaction time on the nucleation and growth of CdSe NCs, as well as MSCs was to be studied.

Finally, the growth behavior of the MSCs was to be studied in more detail with emphasis on the evolution of the MSC populations with time. This was to be done to evaluate, whether or not the particles exhibited a sequential growth behavior. Additionally, their growth behavior in the presence, and absence, of additional monomer was to be compared.

4. Achieving Nucleation and Optimization of the Continuous-Flow Device

4.1. Conceptualization of Continuous-Flow Device

At the beginning of this project stood the idea of observing colloidal quantum dot formation *in situ* and learning about the role MSCs play during this formation process. In order to quickly be able to start working on the chemistry involved and to have a controlled and standardized environment, the initial approach was to set up a commercial stopped-flow device. These devices generally offer very fast and high-quality mixing, combined with very low dead times and, if used with a rapid characterization technique, very good time resolutions. Their applicability to the study of nanoparticle formation processes has been reported numerous times in recent years.[43,45,46,126–128]

A major drawback of these systems, however, stems from what is principally their main advantage, that is, that the processes can be literally studied *in situ*. For this to be possible, the reaction, which is being studied, has to occur in the same place as the characterization. Typical systems use quartz cuvettes, connected to the flow system. While quartz glass itself can withstand high temperatures without issues, the thermal durability of the connections and glues used in the construction of the cuvettes greatly limit the usability of the aforementioned commercial setups for the high-temperature colloidal synthesis routes which were to be investigated in this project. And indeed, their previously mentioned use has been reported for ZnS,[43,126,127] PbS,[45] and gold nanoparticles[46,128], all of which have been prepared around room temperature.

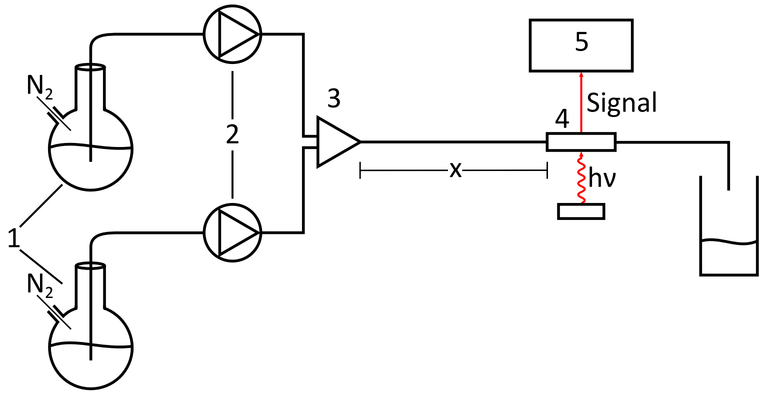

Figure 4.1.: Schematic drawing of the CFD concept.

While the development of a high-temperature cell for a stopped-flow device compatible with optical spectroscopy, as well as X-ray scattering techniques, would have been a possibility, it was deemed as significantly more time-efficient, to utilize the knowledge already present within the lab to pursue a different approach. Based on the concept of a continuous-flow reactor for the production of colloidal quantum dots developed by Jan Niehaus[122] and further advanced by Daniel Neß[123], Katharina Poulsen[124] and Tobias Jochum[125] (all CAN GmbH) in their respective PhD theses, a continuous-flow device for the characterization of the formation processes of colloidal quantum dots was to be set up.

A schematic drawing of the proposed CFD concept is shown in figure 4.1. It is divided into a precursor, reaction, and characterization stage. The precursor stage comprises the precursor solutions, stored under nitrogen, (1) and the continuous pumps (2) which were to be used to pump them into a mixing chip (3). In the mixing chip, which was to be heated to reaction temperature, the reaction was supposed to be initiated and as such it represents the beginning of the reaction stage. For proper *in situ* study of the nanoparticle formation, the reaction stage would have to end directly at the measurement cell (4), which, together with the detector (5) and light source compose the characterization stage. The crude product of the reaction would eventually be collected to allow further *ex situ* analysis. In this concept the reaction time would directly correspond to the time the reaction mixture spends between mixing chamber and measurement cell and as such be a

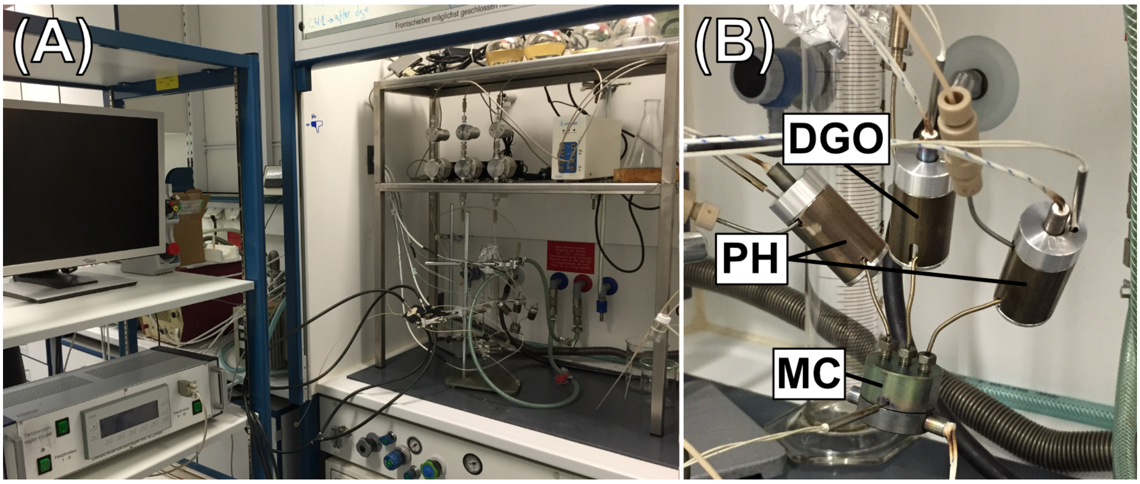

Figure 4.2.: Photographic depiction of the CFD setup: (A) the complete setup in the lab, (B) enlarged view of the reaction stage.

function of the flow rate and the length x of the tubing in between.

Figure 4.2 (A) shows the practical implementation of the CFD concept in the lab. The precursor stage can be seen on the two upper levels of the rack, with the precursors at the top and the pumps below. The reaction and characterization stage are located in the lower level of the rack. An enlarged view of the reaction stage is shown in figure 4.2 (B). For the practical application a preheating stage was added, composed of two preheating ovens (PH). Additionally, a delay growth oven (DGO) was attached to the mixing chamber (MC). An exploded 3D rendering of the growth oven (in-house design) is shown in figure 4.3 (A). It consisted of tubing coiled around a heated core, varying its length allowed the variation of the length x. In consequence these oven lengths are mentioned throughout this work, as they, in conjunction with the flow rate, defined the residence time.

Figure 4.3 (B) shows an exploded 3D rendering of the mixing chamber (acquired from micro 4 industries), highlighting the interdigitated mixing structure sandwiched between the heated bottom and the top in which the temperature was measured. A graphite gasket ensured sealing of the mixing chamber to the outside and improved heat conduction from the bottom to the top. The very small inner volume of the mixing chamber (8.4 µL measured from the point of mixing to the outlet) resulted in a very short residence time (below 1 s) compared to the growth oven.

This disparity between residence times made the setup very promising in order

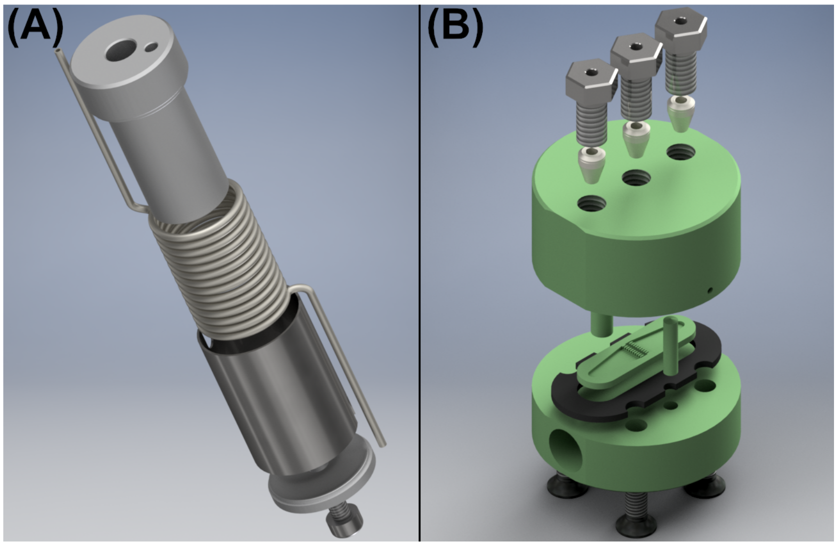

Figure 4.3.: Exploded 3D renderings of a growth oven (A) and a mixing chamber (B) as they are used in the CFD.

to separate nucleation and growth, a prerequisite to form high-quality NCs. This would be achieved by setting the mixing chamber temperature high enough to allow nucleation, while heating the growth oven to a temperature below the nucleation threshold, thus ensuring no secondary nucleation in the growth oven. In consequence, the terms nucleation and growth temperature are used synonymously with mixing chamber and growth oven temperature throughout this work. While this nomenclature is not completely accurate, as, for example, under most circumstances, some growth already occurs within the mixing chamber, it represents a convenient simplification of terminology.

Due to the same thermal limitations discussed earlier with regard to the stopped-flow measurement cells, a heat exchanger was introduced to the final setup, to quench the reaction (thus definitely defining the residence time and the end of the reaction zone) by cooling the reaction mixture and at the same time saving the measurement cells. This represents a compromise between the possibility of true *in situ* measurements and the conduction of high-temperature colloidal NC syntheses.

Measurement of UV/Vis spectra was possible using flow cells with 0.5 mm or 3 mm optical path length, the latter allowing the detection of lower analyte concentrations. A more detailed description of the CFD setup is given in section 8.1.1, together with a detailed account of the standard procedure of the CFD experiments applied throughout this work in section 8.1.2.

4.2. Preliminary Experiments: Choice of Precursor System

After completion of the preliminary CFD setup, the CdSe quantum dot synthesis had to be achieved in the device. The goal was to find reaction conditions, that allowed study of nucleation and growth kinetics in the CFD. For this purpose, the reaction rate had to be compatible with the time resolution of the CFD. In initial experiments a precursor system previously tested in batch reactions was used. The Cd precursor contained CdO and octadecylphosphonic acid (ODPA) dissolved in Cyanex, while the Se precursor consisted of elemental Se dissolved in pure trioctylphosphine (TOP). Experiments were conducted using a growth oven of a set length at a set temperature and varying the residence time through variation of the flow rate. After several unsuccessful attempts at CdSe preparation using a Cd-to-Se ratio of 1:2, the use of a Se precursor with higher concentration (Cd-to-Se ratio 1:10) resulted in the first successful NC synthesis in the newly commissioned CFD.

UV/Vis absorption spectra obtained using the online absorption spectrometer during one of the first successful CdSe syntheses, using a growth oven of 30 cm, are shown in figure 4.4 (A). The spectra show a distinct absorption maximum between around 500 nm after 0.75 s and around 625 nm after 2.76 s at 350 °C. The continuous shift in wavelength of the absorption maximum with time highlights the continuous growth of the NCs with reaction time. After 2.76 s a broadening of the absorption feature, accompanied by a reduction in peak optical density (OD) was observed, indicating a broadening of the particle-size distribution. The growth in size accompanied by the observed broadening of the size distribution is indicative of Ostwald ripening, i.e. the growth of large particles via dissolution of smaller ones.

These first results showed the complete reaction, nucleation, growth and complete consumption of free monomer leading to Ostwald ripening, to occur within a time frame detectable in the CFD. Moreover, the very fast reaction rate points out the advantage of the CFD compared to the conventional method of reaction tracking of taking samples from batch reactions. Control over reaction time and access to early stages of the reaction are very limited in that approach. A fact highlighted by

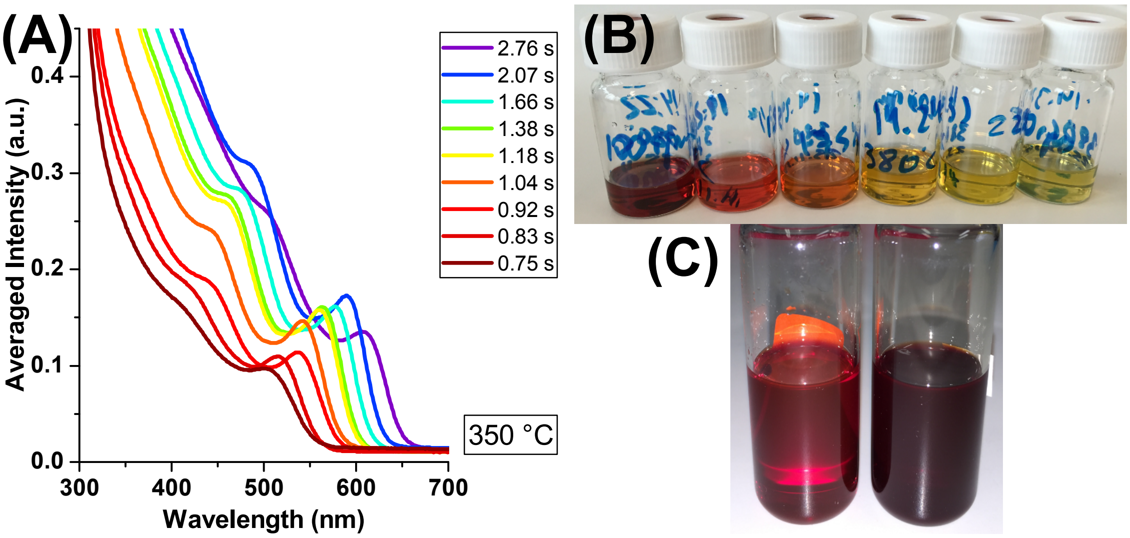

Figure 4.4.: Successful commissioning of the CFD: (A) UV/Vis absorption spectra obtained during one of the first successful growth experiments using CdO precursor and Cd:Se ratio of 1:10, (B) samples collected during a CFD growth experiment, (C) samples collected during batch NC synthesis.

the contrast between the samples obtained from a similary experiment as the one previously discussed (figure 4.4 (B)) and the samples taken as quickly as possible during a batch synthesis conducted under comparable conditions (C). The dark red to brown colour of the batch samples clearly shows the advanced stage of the reaction and the large size of the particles in these solutions.

In order to investigate the influence of TOP on the reaction rate, a Se precursor in which a large part of TOP was replaced with Cyanex was prepared. As the reduction of ligand was expected to increase the reaction rate, the previously discussed reaction conditions appeared to be unsuitable, as the reaction was already very fast. As a result the Cd-to-Se ratio was increased back to 1:2 as it was in the initial tests.

Figure 4.5 shows UV/Vis absorption spectra obtained during an experiment at a temperature of 380 °C in both mixing chamber and growth oven (10 cm), using the aforementioned precursor. The residence time was again varied by varying the flow rate. Within the time frame studied in this experiment, the formation of an absorption maximum, its continuous shift to larger wavelength, as well as its eventual broadening and reduction in peak OD were observed. This showed, that using the reduced TOP precursor it was possible to observe nucleation, growth as well as

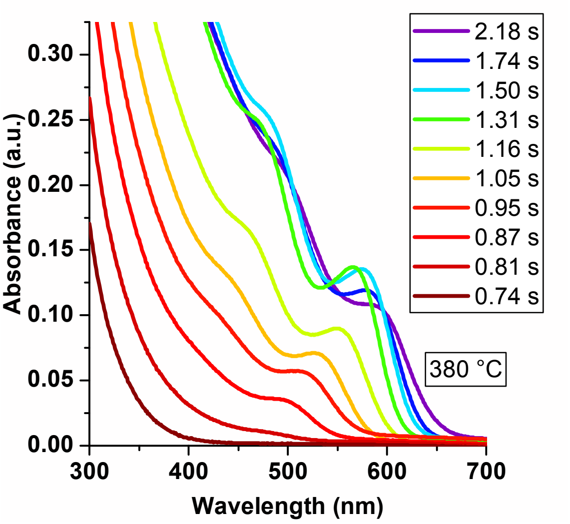

Figure 4.5.: UV/Vis absorption spectra obtained during growth experiment using CdO precursor, a Cd:Se ratio of 1:2 and a reduced amount of TOP.

onset of Ostwald ripening within an observable time frame. Further preliminary experiments, utilizing precursors with different TOP content, appeared to exhibit varying growth rates, indicating an interesting subject of study.

Both precursor systems investigated exhibited very fast reaction rates, resulting in the formation of precipitate as a byproduct of the reaction. As this could cause blockage of the flow system, another precursor system was required. In consequence, the previously employed precursor systems were abandoned, in favor of the well established precursor system used by Tobias Jochum (CAN GmbH) in his PhD thesis.[125] The Cd precursor was based on $Cd(OAc)_2$ and ODPA dissolved in Cyanex and TOP and the Se precursor was elemental Se dissolved in octadec-1-ene (ODE) and TOP. The Cd-to-Se ratio was again 1:10. This precursor system was used throughout the rest of this work with slight variations. In addition to the change in precursor, pressure sensors were introduced into the CFD setup, to allow early detection of blockage of the flow system.

In a standard CFD experiment using a 90 cm growth oven and a reaction temperature of 350 °C in both mixing chamber and growth oven, the UV/Vis absorption spectra shown in figure 4.6 (A) were obtained at different flow rates. All spectra show a very narrow and well defined first absorption maximum, together with additional well defined maxima related to higher energy transitions. As opposed to the pre-

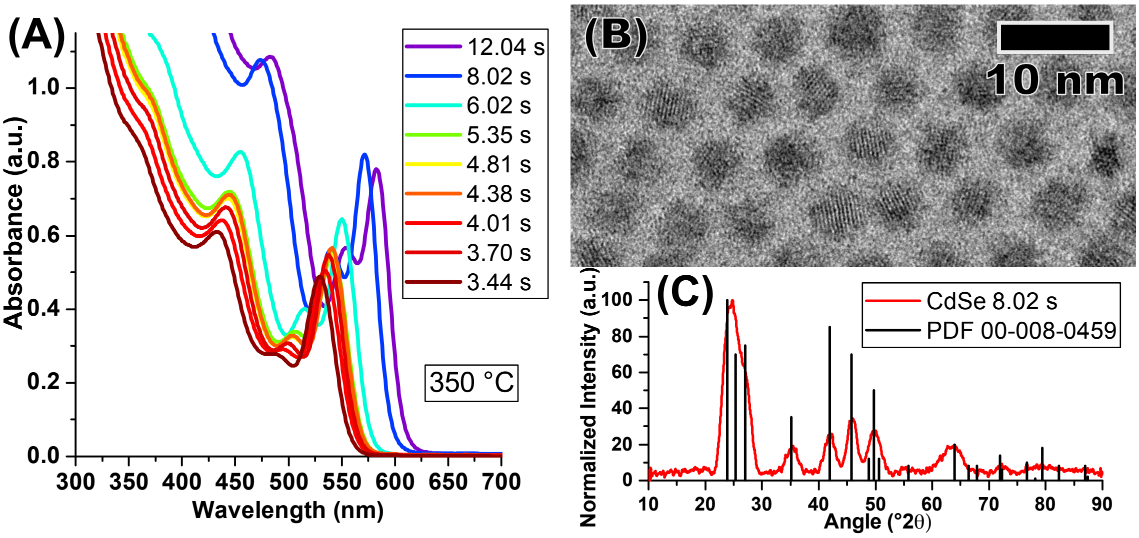

Figure 4.6.: Introduction of $Cd(OAc)_2$ precursor: (A) UV/Vis absorption spectra obtained during growth experiment using $Cd(OAc)_2$ precursor, (B) transmission electron micrograph of CdSe NCs prepared in the CFD during a residence time of 8.02 s, (C) X-ray diffractogram of the same sample of CdSe NCs plotted together with reference reflexes for hexagonal CdSe from ICDD's PDF database.

vious experiments, the long growth oven resulted in relatively long residence times compared to previous experiments. As a result even after the lowest residence time, the spectra exhibits a clear and well defined peak at a wavelength above 500 nm, indicating that the nanoparticles have formed earlier and already grown. After 12.04 s of residence time, no significant peak broadening due to Ostwald ripening could be observed.

Figure 4.6 (B) shows a TEM image of the second largest sample of CdSe NCs, obtained after a residence time of 8.02 s. The crystals appear to have a uniform shape and size and the visibility of lattice planes indicates high crystallinity. An X-ray diffractogram of the same NC sample is shown in figure 4.6 (C), together with reference reflexes of hexagonal CdSe (PDF 00-008-0459). The reflexes in the measured diffractogram appear broadened due to the small size of the NCs, but their angular position is in good agreement with the reference diffractogram, giving confirmation, that the material is indeed wurtzite CdSe.

The new precursor system evidently causes a significant reduction in reaction rate, compared to the previous, CdO based ones. This is highlighted by the plot

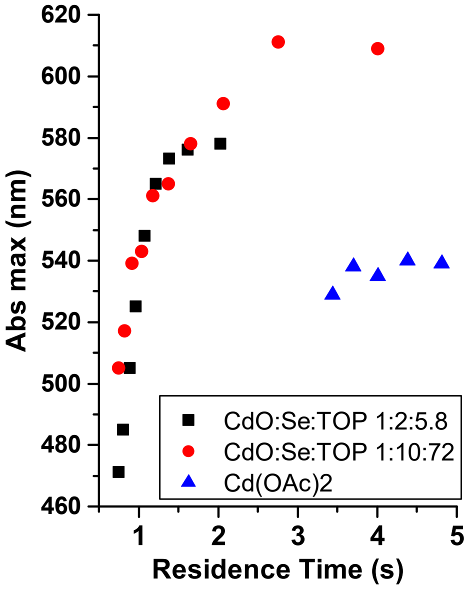

Figure 4.7.: Comparison of reaction rate for different precursor systems: Plot of absorption maxima against residence time for experiments discussed in this section.

of absorption maxima versus residence time for all three experiments discussed in this chapter, which is given in figure 4.7. The initial experiment is plotted in red, labelled CdO:Se:TOP 1:10:72, while the second one is plotted in black, labelled CdO:Se:TOP 1:2:5.8. The third one, using the $Cd(OAc)_2$ precursor is plotted in blue. The growth rate observed during the first two experiments appears to be very similar, despite the difference in precursor and reaction temperature. While this might be just coincidence, the difference to the third experiment, in which a much lower reaction rate was observed, is clearly visible.

The switch to the $Cd(OAc)_2$ precursor resulted in a significant reduction in reaction rate. This allowed a higher flexibility, making the earlier stages of the reaction more easily accessible. The NCs formed with this precursor are of high quality, which is an additional advantage. The observations made in the experiments discussed within this chapter set the stage for the rest of the project, regarding the definition of standard experimental parameters for the CFD experiments. The reduced reaction rate led to the use of lower flow rates, to achieve longer reaction times, making the experiments easier handleable.

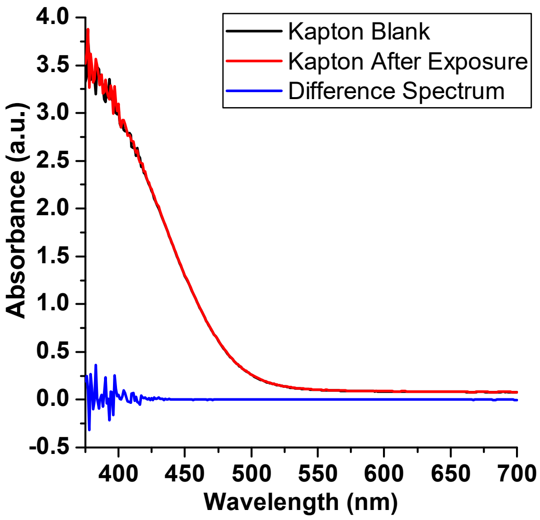

Figure 4.8.: UV/Vis absorption spectra of Kapton foil before and after exposure to CdSe NC solution, as well as the difference spectrum.

4.3. Adaptation to Synchrotron Beamlines

In order to use X-ray scattering techniques for the characterization of NCs formed in the CFD, it was necessary to develop an X-ray flow cell. This flow cell needed to be transparent to X-rays and also compatible to the flow system. In addition, to allow *in situ* measurements, it had to possess sufficient thermal stability and be chemically inert.

The most promising material to construct the flow cell from was Kapton, a polyimide material developed by DuPont. Being a material used for the construction of X-ray windows, medical tubing and environmental shielding of space craft, made it appear quite suitable for the intended application. In fact, it possesses virtually no scattering background for X-rays and retains most of its mechanical properties at temperatures up to 400 °C.[129]

In an initial test of the material's suitability, a piece of Kapton foil was submerged in a solution of CdSe NCs, previously prepared in the CFD, over several days. The UV/Vis absorption of the foil was measured before and after the experiment, in order to probe for potential adhesion of NCs to the surface. The spectra obtained in this measurement are shown in figure 4.8. The blue line plotted in the figure is the difference between the two spectra. Evidently, the absorption spectrum of the foil had not changed, during the exposure to the NCs and their solvent, indicating that no changes had occurred to the material and no NCs had adsorbed to it.

In order to use the material in an X-ray flow cell, commercially available Kapton tubing was acquired. The connection of this tubing to the flow system was realized by inserting a piece of titanium tubing and sealing it with HPLC-style titanium fittings, the bore of which had been enlarged to 1.8 mm (the outer diameter of the Kapton tubing). An exploded 3D rendering of the complete Kapton flow cell (KFC) showing the individual components is given in figure 4.9. The newly constructed device was incorporated into the CFD between the growth oven and heat exchanger during CdSe NC synthesis, in order to test the applicability of the design. As it showed no leakage at all investigated temperatures (up to 260 °C), the design was considered suitable.

Using the KFC at a synchrotron beamline required a possibility to mount it in a defined orientation, without applying too much force on the fragile Kapton tube. Additionally, the mounting solution had to be heatable, in order to allow *in situ* measurements. For this purpose, a two-piece sample holder, composed of an aluminium block, containing bores for a heating cartridge and resistance temperature detector (RTD) and an aluminium lid, was designed. An exploded 3D rendering of the prototype of this design, capable of accommodating a single KFC is shown in figure 4.10 (A). The sample holder possesses a central bore for the Kapton tube and additional cut-outs for the fittings. When the KFC is mounted in the sample holder, the fittings at either end are clamped by the two pieces of the holder, without applying force to the Kapton tube. Finally the sample holder possesses a central window through the block, allowing the incident X-rays to pass through without interaction. The window in the lid possesses a chamfered edge, corresponding to an angle of 120°, the vertex of which coincides with the center of the Kapton tube. This feature allows the light scattered within the KFC to be detected unhindered. An engineering drawing of the prototype sample holder including all dimensions is given in the appendix (A.1).

Temperature distribution in the prototype sample holder was sufficiently homogeneous, with a maximum of +1 °C difference between the temperature measured in the KFC channel and in the RTD bore between 250 °C to 330 °C. Further tests, with a mounted KFC, during NC synthesis in the CFD, placing the sample holder between growth oven and heat exchanger, proved the design to work well at tem-

Figure 4.9.: Exploded 3D rendering of the X-ray flow cell based on commercially available Kapton tubing.

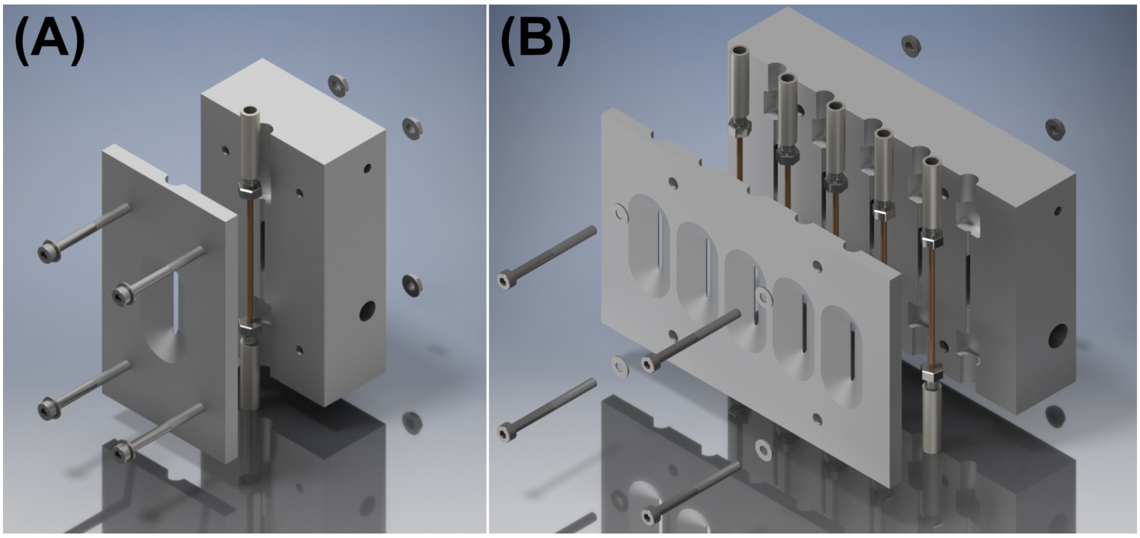

Figure 4.10.: Exploded 3D renderings of the heatable sample holder for the KFC: (A) single-cell prototype, (B) multi-cell design ”Apollo”.

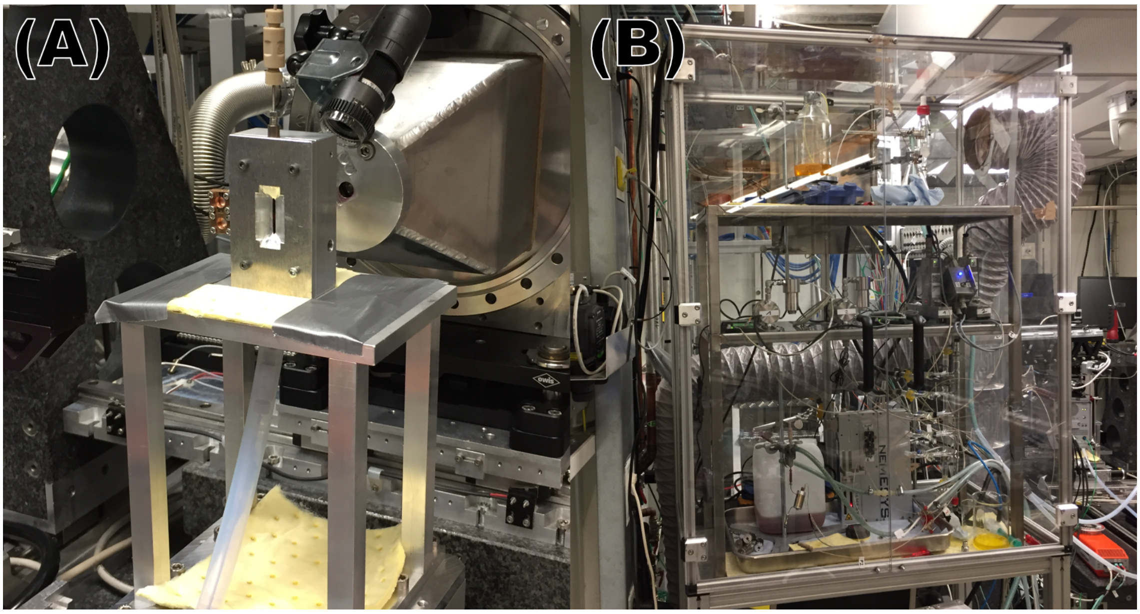

Figure 4.11.: Practical setup at beamline P03 at DESY: (A) a KFC mounted in the prototype sample holder in the beam path at P03, (B) the vented cover containing the remainder of the CFD setup.

peratures up to 330 °C, without any leaks.

In order to allow time-resolved *in situ* measurements an alternative multi-cell sample holder design was devised. An exploded 3D rendering is shown in figure 4.10 (B). This design, dubbed "Apollo" due to the increased complexity of the setup, featured slots for five KFCs. These were to be linked via growth ovens, while the mixing chamber was to be connected at the inlet and the heat exchanger at the outlet of the system. Measurement of SAXS or WAXS patterns in each of the positions would then allow the investigation of different stages of the reaction. An engineering drawing of the Apollo sample holder including all dimensions is given in the appendix (A.2).

Initial tests in the lab showed no leaking of a three-KFC assembly, connected to mixing chamber, two ovens and heat exchanger, in the Apollo holder at pressures up to 6 bar and temperatures up to 230 °C. Its practical application remained limited, however, due to the increased complexity of the resulting setup.

As opposed to the Apollo holder, the prototype holder was used successfully in multiple beamtimes. Figure 4.11 (A) shows a photograph of the holder being set up at beamline P03 at DESY, where it was used as an *ex situ* X-ray flow cell (being

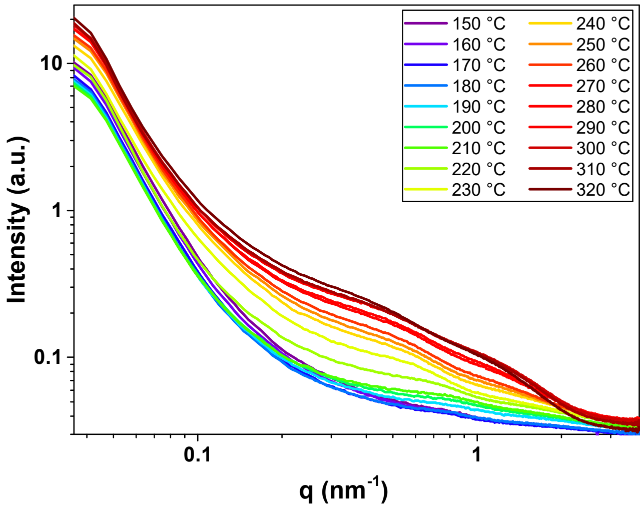

Figure 4.12.: Synchrotron SAXS scattering curves obtained in the Kapton flow cell at different temperatures during a CdSe growth experiment carried out at ID02 at ESRF.

placed downstream of the heat exchanger). Note the custom support on which it is mounted, including an opening for the flow connection. A comparable support was developed for all beamline applications, considering the beam height, as well as local fastening options. Figure 4.11 shows the cover, which was constructed to house the rest of the CFD during the same experiments. It was connected to the exhaust system, in order to initially contain and subsequently vent fumes resulting from potential leakages.

As a final example illustrating the successful application of the prototyp sample holder, synchrotron SAXS scattering curves obtained during an *in situ* growth experiment at beamline ID02 at ESRF are shown in figure 4.12. All scattering curves have been collected in the KFC mounted in the prototype holder, which was heated to a range of growth temperatures. The variation in reaction progress at the different temperatures can be seen from the shape variation of the SAXS curves, with the shift of maxima to smaller q with increasing temperature indicating growth of the NCs. The in-depth evaluation of the data shown here, and obtained from all other beamtimes is still carried out at the time of writing of this work.

In conclusion an X-ray flow cell based on commercially available Kapton tubing was developed in conjunction with two sample holders, allowing mounting and heating of the flow cell. While the multi-cell sample holder design saw limited use, the single-cell design was used successfully both in *in situ* measurements as well as as an *ex situ* X-ray flow cell in four beamtimes to date.

5. Characterizing Nucleation and Growth of CdSe NCs in the CFD

In order to employ the CFD properly in the investigation of nucleation and growth dynamics of CdSe NCs, it was necessary to characterize the nucleation and growth of CdSe NCs within the device. The idea was to find the lowest temperature at which nucleation occurs, in order to be able to differentiate the two processes within an experiment. In addition, finding this critical nucleation temperature was expected to allow studying the earliest nucleation events, by setting nucleation temperatures slightly below and above this threshold value.

The first part of this chapter covers the efforts made to find the critical nucleation temperature. Subsequently, results of experiments varying the nucleation and growth temperature, in order to characterize the growth process are discussed, highlighting the discovery of absorption features related to species of magic-sized CdSe clusters during these experiments. Finally, an overview of the experimental conditions under which these clusters were observed is given.

Throughout this chapter, all experiments were conducted at the same flow rate, varying only nucleation and growth temperature, as well as oven length. This was done in an effort to simplify the interpretation of experimental results, as a variation of the flow rate not only varied the residence time in the growth oven, but as well in the mixing chamber. In consequence, variation of the total residence times shown in the data throughout chapter 4 lead to variation of the time, the reaction mixture spent at nucleation temperature. This makes comparison of the individual results much more complicated. In addition, this modification of experimental procedure results in a reduction of variable parameters in the investigation of this highly complex system.

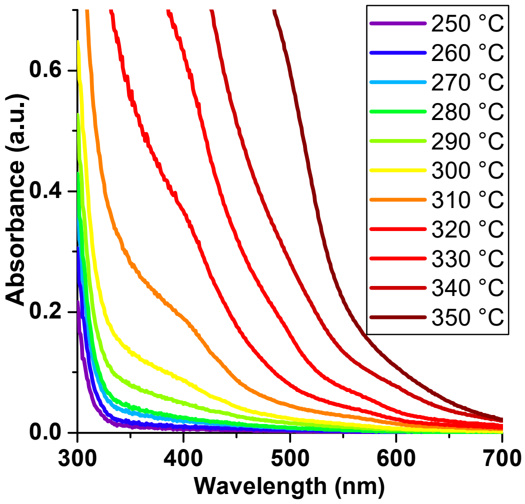

Figure 5.1.: Determining the critical nucleation temperature in the mixing chamber: UV/Vis absorption spectra obtained after 0.46 s in the mixing chamber at different temperatures and subsequent quenching.

5.1. Determining Critical Nucleation Temperature

5.1.1. Nucleation in Mixing Chamber

In order to determine the onset of nucleation in the mixing chamber alone, a heat exchanger was directly connected to the mixing chamber. Utilizing a flow rate of 2 mL/ min, a residence time of 0.46 s was realized between the point of mixing and the quenching in the heat exchanger. In previous experiments, it was determined, that at higher flow rates NC concentration after the mixing chamber was insufficient to yield detectable OD. The temperature of the mixing chamber was then varied to find the lowest temperature, where concrete evidence of nucleation could be observed.

Figure 5.1 shows UV/Vis absorption spectra obtained during a nucleation experiment in which the nucleation temperature was varied during the experiment. With increasing temperature the slope of the absorption spectrum increases. Very slightly between 250 °C and 280 °C. Starting at a nucleation temperature of 290 °C, the increase becomes more significant with every 10 °C increase. Starting at 310 °C, a broad absorption feature was observed, located at around 400 nm. A further increase of temperature led to an additional increase in OD and eventually to a shift of the absorption onset to longer wavelength.

The UV/Vis absorption spectra shown in figure 5.1 are representative for all spectra obtained in mixing-chamber-only experiments. Generally no well resolved absorption features were observed, while experiments under similar conditions using a growth oven yielded spectra exhibiting distinct absorption peaks (compare figure 4.6 (A) and spectra shown in section 5.2 and following). This indicates, that a longer residence time is required to obtain a population of NCs with a well-focussed size-distribution. Nevertheless, particles already form within the first half-second of the reaction.

Determining the critical temperature for this to occur with precision is difficult, due to the absence of well-defined absorption maxima. From the spectra obtained in the present experiment, it can be clearly said, that nucleation must have occurred at 310 °C, as an absorption feature could be observed. The changing slope of the spectrum obtained at 300 °C, suggests, that nucleation has also occurred at this temperature, despite the absence of a distinct absorption feature. At lower temperatures, a definite statement, whether nucleation has occurred cannot be made, as all spectra, starting at 270 °C, exhibit an increasing slope.

In summary, nucleation in the mixing chamber was not clearly observed at temperatures below 300 °C.

5.1.2. Nucleation in Growth Oven

In the mixing chamber alone, concrete evidence of nucleation could not be observed at temperatures below 300 °C. Considering that spectra obtained at lower temperatures also showed increasing OD compared to the initially recorded spectra, it appeared reasonable, to assume that nucleation can occur at even lower temperatures. In order to verify this assumption, experiments were carried out at longer residence times by using a growth oven in addition to the mixing chamber.

Figure 5.2 shows UV/Vis absorption spectra obtained in a standard CFD experiment using a 50 cm growth oven, a flow rate of 2 mL/ min, a nucleation temperature of 260 °C and varying the growth temperature. Even at a growth temperature of 180 °C, well below the temperature range where nucleation was observed, a broad absorption feature could be observed. With higher growth temperature, the feature became better resolved, while OD increased significantly, and additional maxima were observed. This clearly shows, that even from nucleation at 260 °C, CdSe NCs

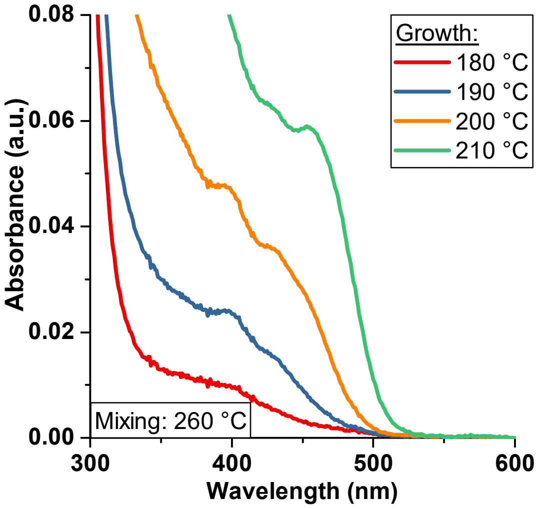

Figure 5.2.: Evidence of nucleation at lower temperature: online UV/Vis absorption spectra obtained at different growth temperatures after a nucleation at 260 °C. Total residence time was 15 s.

could be grown and that the critical nucleation temperature must be lower than the values observed in the mixing chamber alone.

The point of determining the critical nucleation temperature was to avoid nucleation in the growth oven, where residence times are multiples of that in the mixing chamber. In consequence, it appeared sensible to investigate the nucleation threshold in a growth oven. The added residence time would give the formed NCs additional growth time. In consequence, the onset of NC formation was expected to be detectable more clearly.

The experiment was first attempted in a 10 cm oven. Both precursors were pumped through preheating ovens and mixing chamber into the growth oven in which the temperature was varied. In experiments, where mixing chamber and preheating ovens were at room temperature, no nucleation was observed in the oven regardless of growth temperature. It was assumed, that the liquid in the growth oven had not reached the set temperature. Preheating to 50 °C, 90 °C and 150 °C had resulted in nucleation at temperatures above the threshold previously observed in the mixing chamber alone. As a result the preheating temperature was increased further to 200 °C. UV/Vis absorption spectra obtained at three different oven temperatures are shown in figure 5.3 (A).

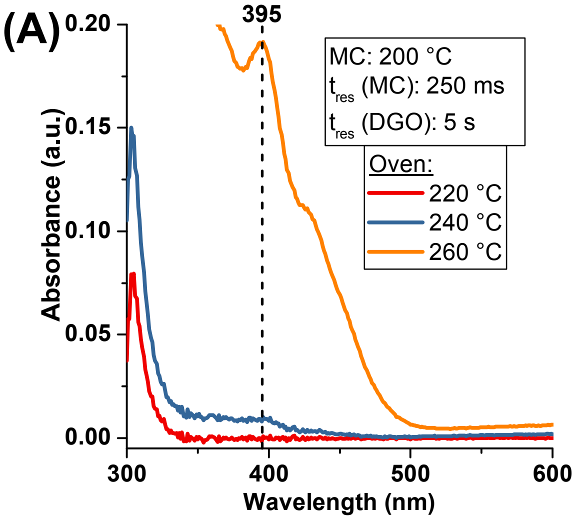

Figure 5.3.: Determining critical nucleation temperature in a growth oven: UV/Vis absorption spectra obtained at different growth temperatures in a (A) 10 cm oven after preheating of mixing chamber and preheating ovens to 200 °C, (B) 90 cm oven without preheating.

At a temperature of 220 °C and below (spectra omitted for clarity), a plain spectrum without features was obtained. Increasing the oven temperature to 240 °C resulted in an absorption spectrum with a very low intensity absorption feature. Further increase of the temperature to 260 °C resulted in a significant increase of OD. At this temperature, the spectra exhibited a distinct and narrow peak centered at 395 nm featuring a shoulder at around 430 nm. The recorded spectra suggest, that the nucleation threshold in this case is at or slightly below 240 °C.

The experiment was repeated using a 90 cm growth oven. In this case, no preheating was done, as it was expected that the residence time of 24 s was sufficient to achieve the desired temperatures. This was assumed, considering that 90 cm ovens were also typically used as preheating ovens. As a result, it has to be noted, that the residence time of the oven is not identical with the total time the reaction mixture spent at temperature. The absorption spectra obtained in this experiment are shown in figure 5.3 (B).

At an oven temperature of 230 °C, the spectrum exhibits no features and is slightly curved. This curvature is due to the reference spectrum, which was obtained in a previous experiment. Spectra obtained at lower temperature (not shown) show the exact same shape, indicating, that no nucleation had occurred at this point.

Increasing the temperature in the oven to 235 °C led to an increase in OD and formation of low intensity absorption features. A further increase of the temperature to 240 °C led to an increase in resolution of these features, while the OD increased simultaneously. At an oven temperature of 250 °C the spectra already exhibited a broad absorption feature close to 500 nm and significantly increased OD compared to the initial spectra.

In the present experiments an onset of nucleation in a temperature range of 235 °C to 240 °C was observed. Due to the increased residence time compared to the mixing-chamber-only experiment, the absence of any indications of nucleation in spectra obtained at lower temperatures and the good agreement of results from 10 cm and 90 cm oven, it seems likely that this temperature is indeed the critical temperature for the nucleation of CdSe NCs from the employed precursor system.

In both experiments, the first species to form possesses its absorption maximum at around 395 nm. Upon increasing the temperature, the population of this species seems to increase, before (or while) larger species, indicated by broad maxima at longer wavelength, form. A similar observation was made in the previously discussed experiment (spectra in figure 5.2). This could indicate a mechanism in which the species of CdSe absorbing at 395 nm forms as an intermediate in the formation of larger NCs. The fact that it additionally possesses a very narrow size distribution after growth at 260 °C, could indicate that it is a species of MSC. A notion supported by the fact, that a cluster of $(CdSe)_6$, possessing an absorption maximum at 395 nm, was previously reported in the literature.[130]

5.1.3. Separation of Nucleation and Growth

The critical nucleation temperature determined here is especially relevant for experiments, where the temperature in the mixing chamber and growth oven are completely decoupled. This is possible, by cooling the reaction mixture in a heat exchanger as soon as it exits the mixing chamber and reheating it in the oven, separating nucleation and growth between the two components. If this is not done, the hot reaction mixture that exits the mixing chamber enters the growth oven and cools down slowly, assuming that nucleation temperature is chosen higher than growth temperature. As a consequence, nucleation can be observed in the growth oven, even if its temperature is set below the critical value. This is so, as the oven temperature is measured in the core of the oven and not directly in the liquid.

Measurements of the temperature at the exit of the oven have shown, that even in 10 cm ovens the set temperature is eventually reached. However, the time it takes to reach this temperature varies, depending on the nucleation temperature. As a result, the residence time of the oven does not equal the time spent at the desired temperature. Generally, this offset is probably small and not a significant issue. It has to be considered, though, that it is not constant, but varies with the difference between nucleation and growth temperature, resulting in deviations from expected behavior in experiments where this temperature difference becomes very large. In such cases, the differentiation between nucleation in the mixing chamber and growth in the growth oven becomes blurred, as both processes can occur simultaneously. As long, as nucleation temperature is chosen sufficiently high, to allow burst nucleation (at or above critical values determined within this section), the chance of secondary nucleation in the oven should be minimal, however, as the monomer concentration drops below the critical minimum concentration of nucleation.

5.1.4. Low Temperature Modification of Precursor Structure

Finding of critical nucleation temperature has been complicated by variations in OD in absorption spectra obtained at temperatures below the onset of nucleation. Often, the spectrum appeared somewhat sloped, even in the absence of NCs. The shape of the spectra, especially the low-intensity ones, was of course strongly influenced by the shape of the reference spectrum. In an ideal case, there would be no absorption from a mix of the precursors, before the reaction, so that a reference spectrum would be completely flat. Unfortunately, this was not the case with the present precursor system, making the choice of when to obtain the reference spectrum rather difficult.

In many experiments, a behavior of the absorption spectra as shown in figure 5.4 (A) was observed. In this case, a reference was recorded at room temperature, and the mixture of the two precursors was heated in the mixing chamber only. While the shape of the spectrum had already varied between the moment of recording the reference and recording the room temperature spectrum, it changed even more drastically upon heating the precursor mixture, evident as a drop in OD across the spectrum, until a curved spectrum was obtained at 100 °C. This is of course an artifact, due to the higher OD of the reference spectrum. In fact, this spectrum is

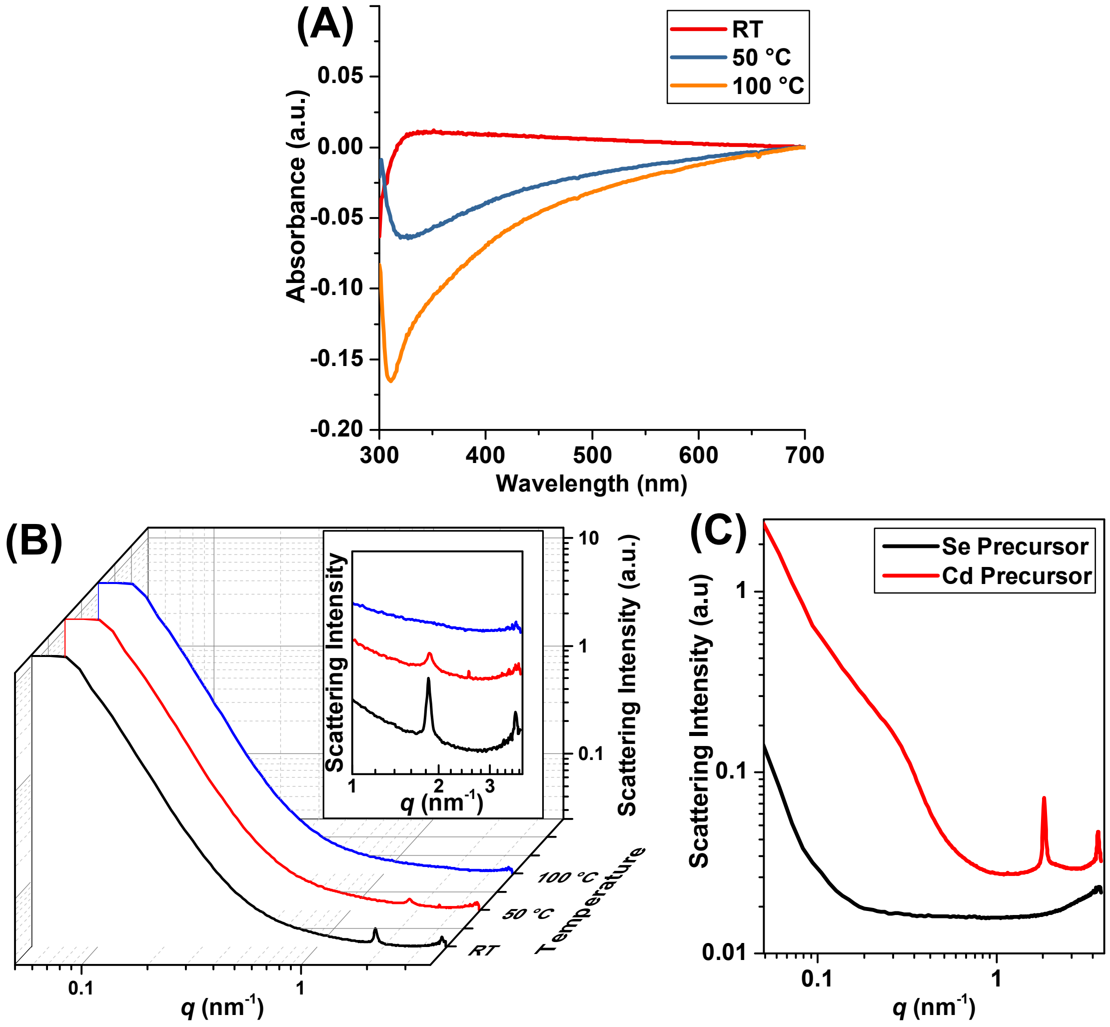

Figure 5.4.: Low temperature modification of precursor structure: (A) online UV/Vis absorption spectra obtained at the same nucleation temperatures, (B) synchrotron SAXS curves obtained at beamline ID02 at ESRF during nucleation experiment in mixing chamber, the inset showing a magnified representation of the Bragg peaks observed above $1\,\mathrm{nm}^{-1}$, (C) scattering curves of the individual precursors used in the nucleation experiment.

a negative of the reference spectrum.

It has to be considered, that the spectra recorded with the online UV/Vis absorption spectrometer were always taken at room temperature, as the reaction mixture was cooled down in the heat exchanger before entering the measurement cell. As a result, the change in OD cannot be a result of the temperature, at which it was measured. Rather, it has to be due to a change in the precursor mixture, caused by the heating in the mixing chamber.

The synchrotron SAXS patterns (figure 5.4 (B)) acquired alongside the absorption spectra tell a similar story. The scattering curve obtained at room temperature shows distinct Bragg peaks at $1.84\,\mathrm{nm}^{-1}$ and $3.69\,\mathrm{nm}^{-1}$, indicating the presence of a periodic structure in the precursor mixture. These peaks diminish significantly after heating to 50 °C and vanish completely at 100 °C. The scattering curves were also obtained after quenching, directly downstream of the optical flow cell.

These observations fit well with the observations made by Abécassis *et al.*, who have reported the presence of a lamellar mesophase in Cd myristate solution at room temperature, which melts upon heating to 100 °C. They also report the presence of two distinct Bragg peaks, with the second, smaller one, located at twice the q value of the first peak, being the second order reflection of the same periodicity. As the same correlation between the two peaks exists in the present scattering curves, the same conclusion can be drawn. The difference in scattering vector between the literature report and the present data can be attributed to the different composition of the reaction mixture and subsequently different period of a structure formed by the precursor.

Additional synchrotron SAXS patterns recorded for the precursors individually (figure 5.4) show, that the structure is indeed formed in the Cd precursor. The increased scattering intensity of the Cd precursor below $1\,\mathrm{nm}^{-1}$ with a broad maximum at around $0.2\,\mathrm{nm}^{-1}$ to $0.3\,\mathrm{nm}^{-1}$ indicates the presence of additional structure.

The present observations suggest, that the Cd-ODPA complex forms similar structures in solution as have been reported for Cd myristate. These structures also dissolve upon heating to 100 °C. It appears, that this assembly of Cd octadecylphosphonate possesses some OD in the visible range, resulting in negative spectra upon dissolution of the assembly, if the reference was recorded at room temperature. As a consequence, reference spectra should be obtained at temperatures above 100 °C. Nevertheless, this issue shows, that there are some variations in OD in the precursor mixture, which do not correlate with CdSe NC formation. A fact, that strongly influences the interpretation of low temperature absorption spectra.

5.2. Formation of Magic-Sized Clusters during CdSe Nanocrystal Growth

This section details the observation of MSCs as intermediates of the formation and growth of regularly growing CdSe NCs during this work. All experiments conducted were nucleation and growth experiments, i.e. CdSe NC synthesis experiments in the CFD, where a combination of mixing chamber and growth oven was used. The experiments entailed variation of the growth oven length, as well as nucleation and growth temperature.

Throughout this section, species of MSCs will be designated by the center wavelength of their respective UV/Vis absorption feature. For example, the species $CdSe_{437}$, which appeared repeatedly in experiments during this work. The position of the absorption maxima was determined manually, by eye, from the recorded absorption spectra, which introduces a certain margin of error, considering that the spectrometer's precision was no more than 1 nm. Additionally, the position of the absorption maxima was influenced by the general shape of the spectra, e.g. its background slope. As a result, peak positions vary by ± 1 nm to 2 nm between experiments. Nevertheless, the underlying clusters are still the same. In order to simplify discussion of the cluster species, the individual moieties will be given only one designation, regardless of the exact position of the absorption maximum, as long as it appears reasonable to assume that only one species is observed. The species discussed in this section are therefore designated $CdSe_{403}$ and $CdSe_{437}$.

5.2.1. Postulated Growth Mechanism

Based on the experiments conducted throughout this work and available literature, a reaction mechanism for the formation of continuously growing NCs via MSC intermediates has been postulated. A schematic representation is shown in figure 5.5. The thickness of arrows in the scheme represents the relative reaction rate of the respective step. The different pathways are selected for via nucleation temperature,

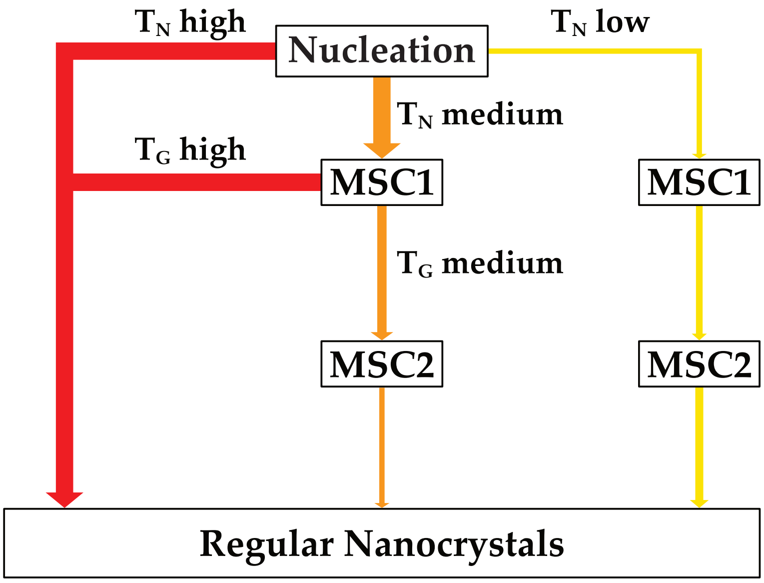

Figure 5.5.: Schematic representation of postulated growth mechanism of regularly growing NCs via MSC intermediates at different reaction temperatures.

which directly affects the number of nuclei formed within the mixing chamber. This in turn determines the formation rate of the first cluster species, as it depends, among other things, on both, the concentrations of nuclei, as well as monomer, according to

$$r_{MSC1} = k[\mathrm{N}][\mathrm{M}] \tag{5.1}$$

with r_{MSC1} being the growth rate, k being the rate constant under the respective conditions, [N] the nuclei concentration and [M] the monomer concentration. A similar rate equation can be formed for the growth of the clusters into the second cluster species, and their growth into regular NC under incorporation of free monomer. In both cases, [N] has to be replaced by the cluster concentration of the previous cluster species.

If the nuclei concentration is sufficiently high (at intermediate T_N in figure 5.5), the nuclei grow quickly through incorporation of free monomer into the first MSC species, as both, [N] and [M] are high. Their subsequent growth into larger clusters occurs slower, in comparison, as [M] has been reduced by the large number of growing clusters. The formation of regular NCs from the second cluster species occurs much more slowly and increasingly via Ostwald ripening, as more of [M] has been depleted at this stage of the reaction. In consequence, these reaction conditions result in an intermediate accumulation of the cluster species.

At low nucleation temperatures, the nucleation rate in the mixing chamber is low, and only a comparatively small amount of nuclei enter the growth oven. This results in a significant decrease of the formation rate of the first MSC species as per equation 5.1, as [N] is small. The subsequent growth into the second cluster species and then into the regular NCs is also relatively slow, due to the small total number of clusters. A slight acceleration of the two later reaction steps (indicated by the wider arrows in figure 5.5) compared to the formation of the first cluster species can be assumed, considering the larger size and consequentially larger reaction cross section of the first cluster species compared to the initial nuclei and of the second compared to the first cluster species. Due to the small number of clusters formed under these conditions, a large excess of monomer is still available once the largest cluster size is reached. This, combined with the increasing reaction rate due to the increased reaction cross section of the larger species, causes an early depletion of the intermediate cluster population under these conditions. The onset of Ostwald ripening occurs only at very late stages of the reaction, during the continuous growth of the NCs, due to the large excess of free monomer at its onset.

At high nucleation temperatures, a large number of nuclei is formed in the mixing chamber. The very high growth rate, due to both the elevated temperature, as well as the large [N] and [M], causes the onset of growth already within the mixing chamber (compare section 5.1.1). The large number of nuclei, and subsequently clusters, that are formed, consume a large amount of monomer in their growth, resulting in an earlier onset of Ostwald ripening. A comparable growth process occurs at lower nucleation temperatures, when high growth temperatures are chosen, as Ostwald ripening strongly benefits from elevated temperatures.

The continuously growing NCs observed in this work are always formed via different species of sequentially growing MSCs. Two of these are repeatedly observed. It can be assumed, that the formation of the first of these cluster species also occurs via additional magic-sized intermediates, as was previously reported.[60] This could not be observed under the present reaction conditions. Through a variation of the nucleation temperature, the presence of these clusters is shifted to earlier and later stages of the reaction. As a higher cluster concentration increases the amount of monomer

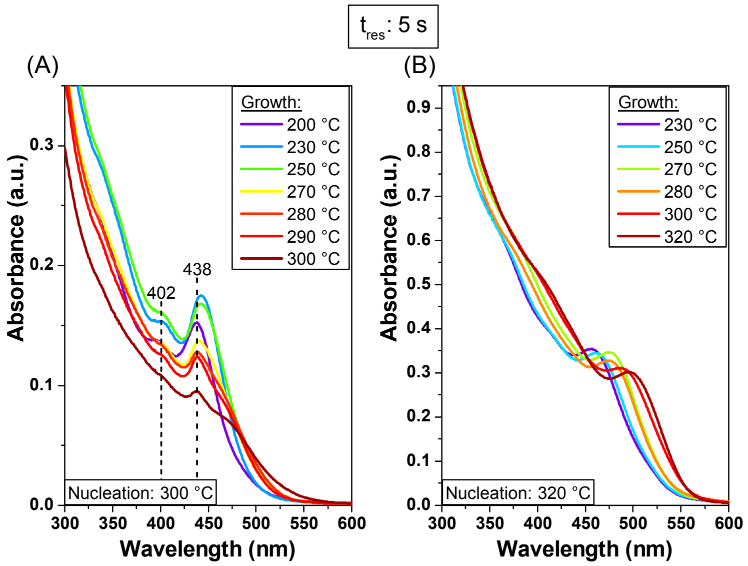

Figure 5.6.: UV/Vis absorption spectra obtained during variation of temperature in a 10 cm growth oven: mixing chamber at (A) 300 °C and (B) 320 °C.

consumed during the different growth steps, the onset of Ostwald ripening occurs earlier with increasing nucleation temperature. In the following, the experiments leading to the postulation of this reaction mechanism are presented.

5.2.2. Influence of Nucleation and Growth Temperature on CdSe Nanocrystal Growth

Following the nucleation experiments, a combination of mixing chamber and growth oven (10 cm) was used to investigate the growth behavior of the CdSe NCs. The flow rate of 2 mL/ min resulted in a residence time of approximately 5 s in the growth oven. Two different nucleation temperatures (300 °C and 320 °C) were investigated and the growth temperature was varied for each. The UV/Vis absorption spectra obtained during the experiment are shown in figure 5.6.

At a nucleation temperature of 300 °C and 5 s at 200 °C growth temperature, a spectrum containing two peaks, one with a relatively low intensity centered at 402 nm and one with a much higher intensity at 438 nm, was obtained. With increasing growth temperature these features did not shift in wavelength, but only in intensity. This suggests, that these species $CdSe_{403}$ and $CdSe_{437}$ are species of MSCs, formed as intermediates in the formation of regular nanocrystals. Considering the presence of their absorption features in all obtained spectra, it is evident, that the growth of nuclei into the first cluster species, as well as of the first into the second cluster species, as discussed above, occurs at all investigated growth temperatures.

Increasing the growth temperature above 250 °C resulted in a reduction in intensity of the peak at 438 nm and the formation of an additional broad absorption feature at its long wavelength flank, indicating the onset of the formation of regular NCs from $CdSe_{437}$. This absorption feature shifted its low energy absorption onset with increasing temperature, indicating the continuous growth of the regular nanocrystals. At the same time, the intensity at 402 nm decreased, when the growth temperature was increased to 300 °C, indicating that the population of this cluster in the sample was nearly depleted at this temperature.

From the recorded data it is apparent, that at a nucleation temperature of 300 °C sufficient nuclei are formed in the mixing chamber, to allow fast growth into the different cluster species at all investigated growth temperatures, according to the intermediate pathway in figure 5.5. Above a growth temperature of 250 °C, the growth of the largest cluster species into regular NCs sets in, which occurs mostly via Ostwald ripening. The increased growth temperature yields sufficient activation energy for this process, which is higher than the one needed for the previous growth within the size-focussing regime. At a growth temperature of 300 °C, the growth of the smaller cluster species into regular NCs is also possible, resulting in further reduction in the population of $CdSe_{437}$, as a competing pathway to its formation is opened up.

The cluster species, which were observed, are consistent with the ones reported by Kudera *et al.* in their study of the sequential growth behavior of CdSe MSCs at low temperatures. They reported the last two species of clusters, that show no continuous growth behavior, to possess absorption maxima located at 406 nm and 431 nm.[60] It has been reported, that the observation of specific cluster species is highly dependent on the reaction environment, especially the available ligands[113,117] Considering this and that the present synthesis features no amine and carboxylic acid, as opposed to the one reported by Kudera *et al.*, but instead phosphonic acid and phosphine oxides, it is no surprise, that the absorption maxima of the observed clusters in the present case differs slightly.

At a nucleation temperature of 320 °C (spectra in figure 5.6 (B)), there was no evidence of the cluster species in the recorded spectra. A continuous growth of

NCs was observed, as the absorption peak shifted continuously to longer wavelength with increasing growth temperature. This nucleation temperature falls into the high temperature category in figure 5.5. At this temperature the reaction had already progressed past the formation of clusters within the mixing chamber, due to the very large number of nuclei formed.

To gain a more comprehensive overview, the experiment was repeated using a 50 cm growth oven, allowing an increased residence time of approximately 15 s in the oven. A larger range of nucleation temperatures ranging from 260 °C to 330 °C was investigated. Growth temperatures were again kept below the nucleation temperature and varied. The lowest growth temperatures investigated were the result of technical limitations, as the oven temperature could not be set lower than 80 °C to 100 °C below the temperature of the mixing chamber due to heating of the oven by the already hot liquid (compare section 5.1.3). The UV/Vis absorption spectra obtained in this experiment are shown in figure 5.7.

At a nucleation temperature of 260 °C continuous growth of NCs was observed. The center of the main absorption feature shifted to longer wavelength with increased growth temperature, as the growth rate increased. Only at very low growth temperatures (180 °C to 200 °C) evidence of MSCs was seen in the shape of an absorption peak at 395 nm (see figure 5.2).

At this comparatively low nucleation temperature only a small amount of nuclei are formed in the mixing chamber. In consequence, the formation of clusters via sequential growth is slow. In the presence of a large amount of unreacted monomer, they grow into larger crystals directly. As a result, the clusters formed as intermediates could not be observed after the reaction time of 15 s, as they had already been consumed. Only at low growth temperatures, where the reaction rate was slow, some of the intermediates could be observed. These observations are typical for growth after nucleation at low temperatures, as outlined in section 5.2.1.

At intermediate nucleation temperatures (270 °C, 280 °C, 290 °C and 300 °C) the intermediate cluster species were observed, in this case, as absorption peaks at 404 nm and 437 nm. This slight variation in peak position compared to the previous experiment is most probably due to the variation in background intensity, influencing the perceived maximum of the absorption features. For all four nucleation temperatures, an increase in cluster population with growth temperature, indicated by an increase in peak intensity was observed. Similarly a continuous growth of regular

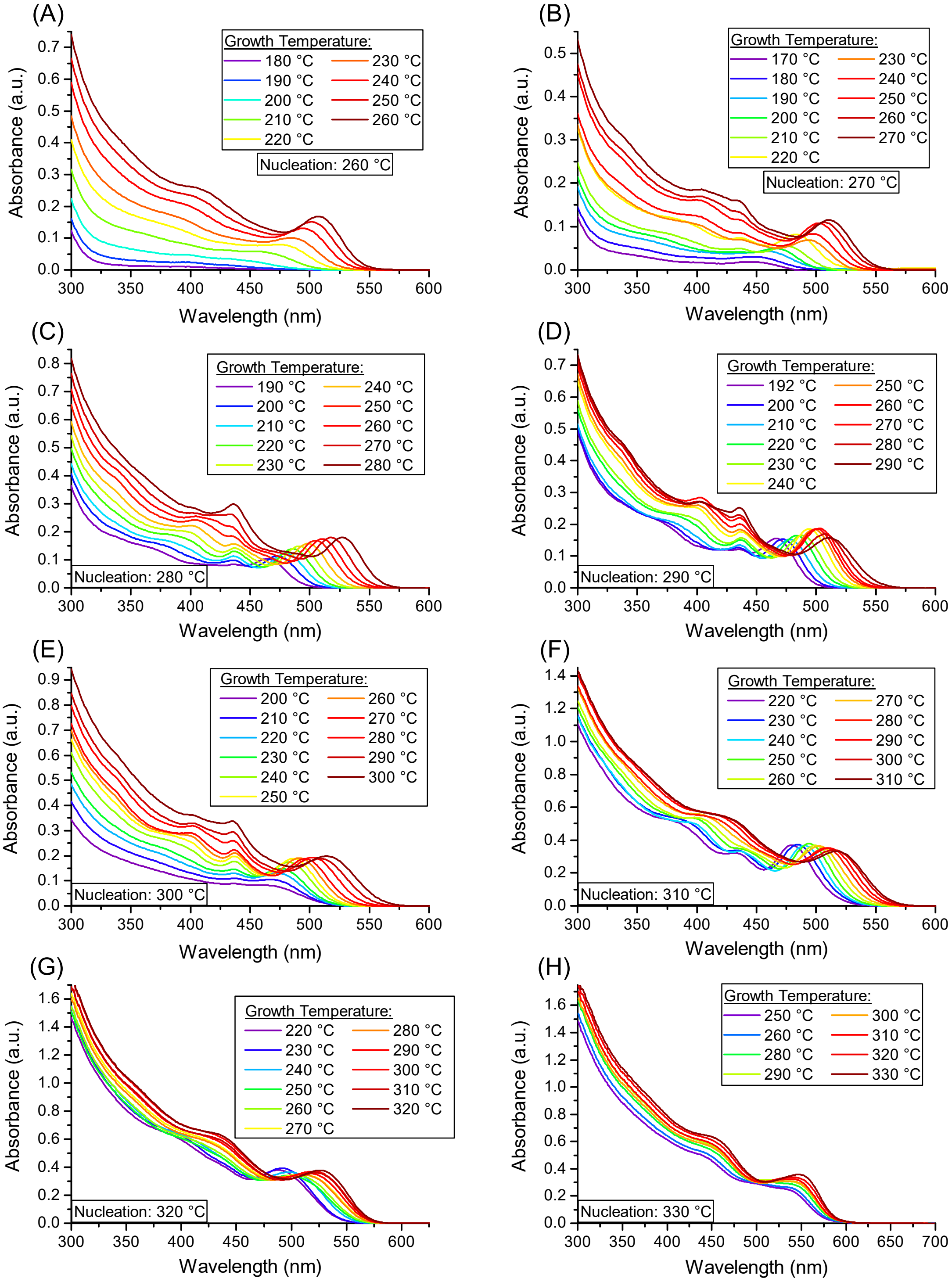

Figure 5.7.: Growth series experiment: UV/Vis absorption spectra obtained during variation of temperature in a 50 cm growth oven for mixing chamber (nucleation) temperatures from 260 °C to 330 °C (A-H).

nanocrystals was observed in all of these experiments, indicated by the continuous shift of peak center wavelength with temperature.

At these nucleation temperatures, NC growth followed the intermediate temperature pathway outlined in figure 5.5. The number of nuclei formed in the mixing chamber was sufficient, to allow fast growth into the first and then second cluster species. As a consequence of the high number of clusters, more intermediate could still be observed after the same reaction time at the same growth temperature than at the lower nucleation temperature. An increase in growth temperature again caused an increase in growth rate. This resulted in an increase in size of the regular nanocrystals with temperature. Since the MSCs grow sequentially, an increased growth rate causes an increase in the population of the larger sizes of MSCs, as was observed in the experiment.

Due to the increased amount of nuclei with increasing nucleation temperature, the first cluster species, $CdSe_{403}$, could only be observed at 290 °C and 300 °C. Firstly, this is simply the result of the higher number of clusters formed from a higher number of nuclei. This is so, as the formation of MSC1 accelerates directly, as a function of the number of nuclei, as per equation 5.1, resulting in a increase of [MSC1] with nucleation temperature. Secondly, however, the growth of the first cluster species into the second one is slowed down with increasing nucleation temperature, allowing the observation of the first cluster species. Its formation rate r_{MSC2}, in analogy to equation 5.1, depends on the concentration of MSC1, [MSC1], and the monomer concentration, [M], by k[MSC1][M]. An increase in [MSC1], causes a disproportionate decrease in [M], however, as every additional nucleus requires several units of monomer to grow into the first cluster species.

While this effect is negligible at lower nucleation temperatures (270 °C and 280 °C), due to the very high monomer concentration in the reaction mixture, it eventually becomes prominent starting at 290 °C. This also becomes evident from the growth behavior of the regular NCs with increasing nucleation temperature. While a rapid increase in peak intensity of the NC absorption feature with growth temperature was observed at a nucleation temperature of 270 °C, it slowed down at 280 °C and the intensity stayed constant at 290 °C.

This behavior is a result of the onset of monomer depletion, due to the larger number of clusters which have grown during the 15 s of residence time. In consequence, the final reaction step in figure 5.5, the growth of the second cluster species into the regular NCs and their subsequent continuous growth, occurs increasingly via Ostwald ripening, rather than size focussing. This is especially evident from the spectra obtained at high growth temperatures at a nucleation temperature of 290 °C. Here, a dissolution of the first cluster species, $CdSe_{403}$, was observed, while $CdSe_{437}$ was still formed (increase in peak intensity). At the same time, the size distribution of the regular NCs broadened, as represented by their absorption peak.

The experiment conducted at a nucleation temperature of 300 °C deviates slightly from the previously discussed trend, but is shown here for the sake of completion. Interestingly, both processes were observed in this experiment, as initially an increase in NC peak intensity with growth temperature was observed, while at higher growth temperatures, a broadening of the NC absorption feature occurred, as growth via Ostwald ripening was increasingly favored.

At higher nucleation temperatures the reaction followed the high temperature pathway shown in figure 5.5. At these nucleation temperatures, no magic-sized intermediates were observed. Instead, continuous growth of NCs with increasing temperature was observed in the studied time frame. As a result of the very high concentration of nuclei formed in the mixing chamber at these temperatures, the growth rate of the first growth steps was so fast, that the reaction had already progressed past the MSC intermediates. Considering the observation of the depletion of free monomer and subsequent onset of Ostwald ripening at lower nucleation temperatures, it can be assumed, that particle growth mainly occured via Ostwald ripening at these temperatures.

While an absorption feature was observed at around 430 nm at a nucleation temperature of 310 °C and a growth temperature of 220 °C (figure 5.7 (F)), it appeared broader than the previously observed cluster peak and shifted to longer wavelength with increasing growth temperature. This indicates, that it did not belong to a MSC, but instead represented a higher energy transition in the regularly growing NCs.

At a nucleation temperature of 330 °C continuous growth of the NCs with temperature was slowed down, while the intensity of the absorption peak increased strongly. This could be an effect of Ostwald ripening at a late reaction stage, assuming that at this stage all smaller NCs have dissolved and all particles have reached a similar size. This would slow down growth, as less and less smaller particles are available for dissolution.

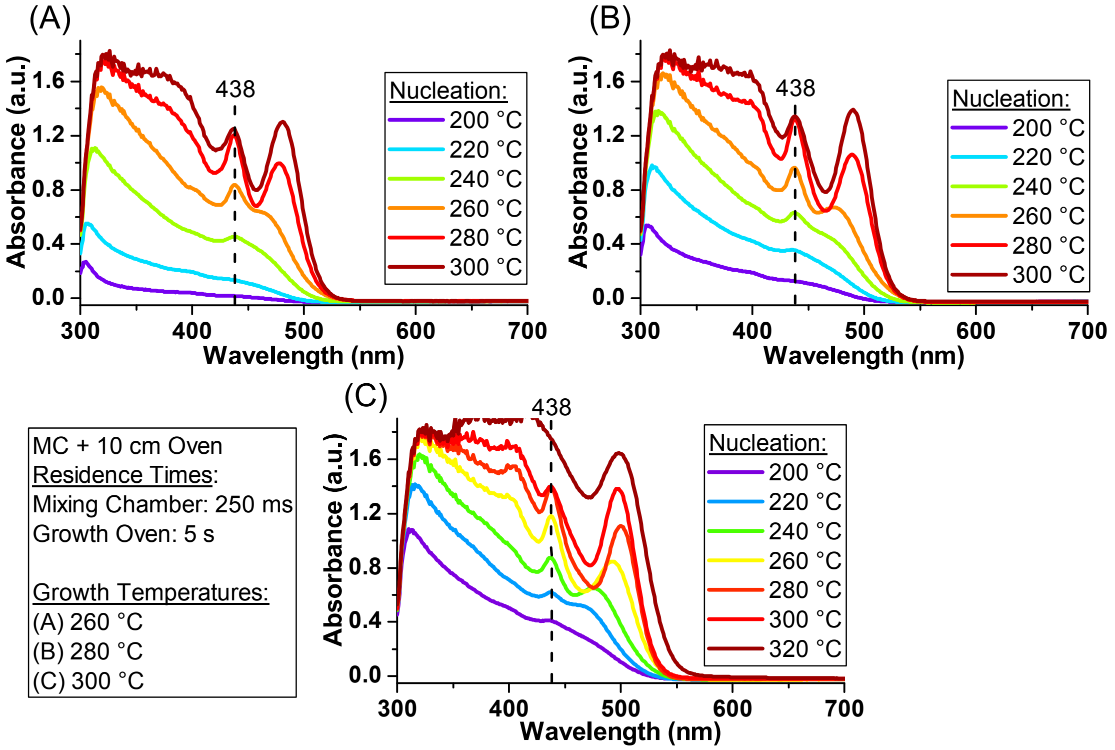

Figure 5.8.: Dependence of $CdSe_{437}$ formation on nucleation temperature: UV/Vis absorption spectra obtained during variation of nucleation temperature, while keeping a constant growth temperature of (A) 260 °C, (B) 280 °C and (C) 300 °C in a 10 cm growth oven.

In summary, an increase of the growth temperature caused an increase in growth rate. In the case of MSCs this caused an increase in population, as the growth of nuclei into the first and then second cluster species was accelerated. The regular NCs, which formed from the MSCs, grew to larger sizes with increased growth temperature and while free monomer was still available, their population also increased, as their formation from the clusters was accelerated. As a result of the increased growth rate, the depletion of free monomer and subsequent Ostwald ripening was observed at high growth temperatures.

An increase of the nucleation temperature caused an increase in concentration of nuclei formed in the mixing chamber, which could then grow within the growth oven. As a result, the MSCs formed as intermediates in the formation of regular NCs, could only be observed in a certain temperature window, where the concentration of nuclei was sufficient, to cause an intermediate accumulation of the MSCs but not so high, that their growth caused a depletion of the concentration of free monomer.

This effect of the nucleation temperature is further highlighted by the results of another experiment, using a 10 cm growth oven, set at a specific growth temperature, while the nucleation temperature was varied. The UV/Vis spectra obtained in this experiment are shown in figure 5.8 for a growth temperature of (A) 260 °C, (B) 280 °C and (C) 300 °C. Based on the total flow rate of 2 mL/ min, a residence time of 5 s was realized. As a consequence, an earlier time in the reaction was investigated than in the previously discussed experiment.

In this experiment an optical flow cell with a path length of 3 mm was used, resulting in much higher ODs than in the previous experiment. In consequence, the presence of $CdSe_{403}$ could not be observed unequivocally, as, especially at high temperatures, the spectra were saturated at this wavelength.

At a growth temperature of 260 °C, the variation of the nucleation temperature between 200 °C and 300 °C caused a significant increase of OD throughout the whole spectrum, indicating the higher concentration of NCs, due to the more rapid nucleation at higher temperature. As was previously discussed, low nucleation temperatures (below 240 °C) led to a low amount of clusters (indicated by the low intensity of the cluster peak). With increasing nucleation temperature above that threshold, the number of clusters increased, as a function of the increasing number of nuclei formed in the mixing chamber. Correspondingly, the formation of regular NCs from the largest cluster species leads to a larger number of NCs of a larger average size being formed with increasing nucleation temperature.

At this comparatively low growth temperature and reaction time, monomer concentration is apparently sufficient, to allow the regular NCs to grow under size focussing, as their size distribution narrows with increasing nucleation temperature. Within the focussing regime, the growth rates of the nuclei into the clusters, the different-size clusters into each other and the largest cluster species into the regular NCs directly depend on the initial nuclei concentration, as is evident from the evolution of the present spectra. With increasing nuclei concentration (=increasing nucleation temperature) the steps in this reaction cascade are accelerated, causing initially the increase in cluster population from 240 °C to 280 °C. The acceleration of the formation of regular NCs from the largest cluster species and subsequently continuous growth is evident from the initial shift of the particle peak to longer wavelength with increasing nucleation temperature under simultaneous increase in intensity compared to the cluster peak. Finally, with an increase of nucleation temperatures from 280 °C to 300 °C the shift from intermediate nucleation temperature into high nucleation temperature regime (as discussed in section 5.2.1) began. The increased number of nuclei further accelerated the growth cascade, as shown by the increase in relative intensity of particle and cluster peak, indicating the larger number of regular NCs as compared to MSCs. At the same time, the higher number of particles undergoing the growth cascade caused a sufficient reduction in monomer concentration, to slow down the continuous growth of NCs, so that no larger size was attained. In consequence, NC growth occurred increasingly via Ostwald ripening.

An increase in the growth temperature to 280 °C and then to 300 °C increases the growth rate, as observed and discussed before. As the reaction progresses further within the 5 s of reaction time, the cluster intensity increases further at lower nucleation temperature (as smaller clusters grow faster into larger moieties) and larger average diameters of regular NCs are reached. The spectrum obtained at a nucleation temperature of 320 °C at 300 °C of growth temperature shows clear signs of the onset of Ostwald ripening as the NCs' growth mechanism, as the MSC population has been completely depleted and the NC size distribution broadened. This coincides with the previous observation of nanoparticle growth at high nucleation temperatures, as discussed before.

The observations made during this experiment clearly confirm the previously postulated growth mechanism. As in the previous experiment, an increase of reaction rate of the sequential growth of nuclei into clusters and then into regular NCs with increasing nuclei concentration could be observed. Again, the magic-sized intermediates could be observed most prominently at intermediate nucleation temperature, where reaction rate, nuclei and monomer concentration cause their intermediate accumulation within the investigated reaction time.

5.2.3. Variation of Residence Time

Figure 5.9 shows UV/Vis absorption spectra obtained under comparable reaction conditions in the two previously discussed experiments. The spectra have been normalized to their respective absorption maximum, since their intensity was vastly different. This was due to the use of the flow cell with 3 mm optical path length in the second experiment (variation of nucleation temperature). While, as a result,

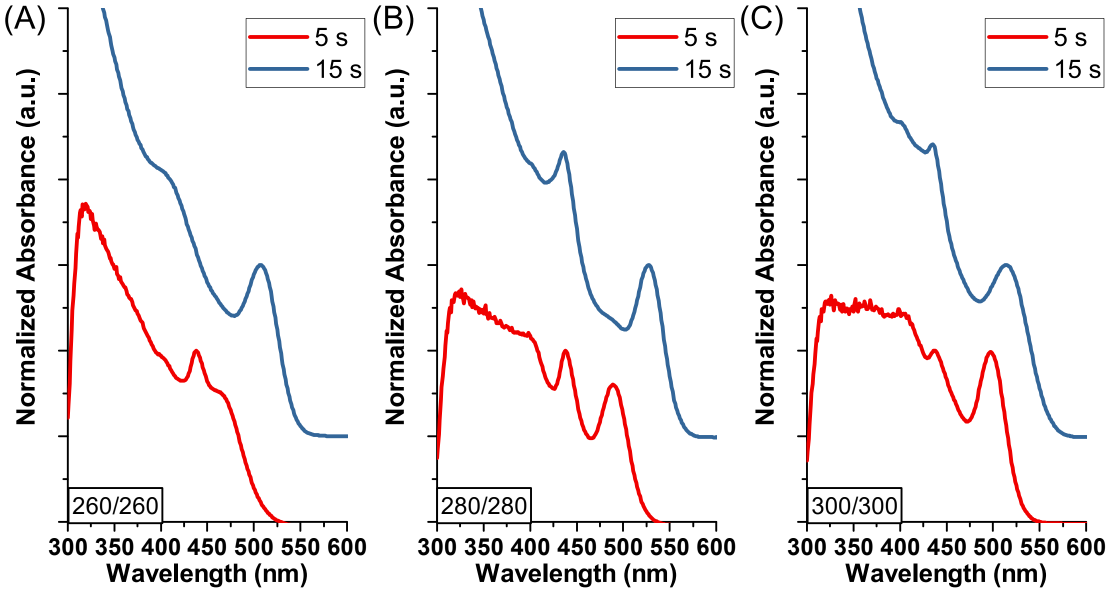

Figure 5.9.: Effect of residence time on cluster formation: UV/Vis absorption spectra obtained for different combinations of nucleation and growth temperature in a 10 cm and 50 cm oven, yielding residence times of 5 s and 15 s. Mixing chamber/growth oven temperatures of: (A) 260 °C/260 °C, (B) 280 °C/280 °C, (C) 300 °C/300 °C.

their intensities and thus concentration changes cannot be compared, the evolution of the respective peak positions within the 10 s residence time difference between the two experiments can be discussed.

In the panel (A) of the figure, the absorption spectra obtained at a nucleation temperature of 260 °C and after 5 s and 15 s at a growth temperature of 260 °C are shown. After a residence time of 5 s, the spectrum exhibits a distinct and well-defined maximum at 437 nm, accompanied by a low-intensity feature at 403 nm and a broad peak at around 475 nm. According to previous observations, the first two features can be assigned to MSCs, while the latter belongs to regularly growing nanocrystals. After 15 s at the growth temperature, the two cluster peaks were not observed any more, while the particle peak appears at longer wavelength, slightly above 500 nm. This further corroborates the previously postulated reaction pathway at low nucleation temperatures. In this case, the small population of magic-sized intermediates, grown from the small number of nuclei formed in the mixing chamber, is depleted by the growing NCs within the first 15 s of the reaction.

At higher nucleation and growth temperatures ((B) 280 °C and (C) 300 °C both), the complete depletion of $CdSe_{437}$ population within 15 s of growth was not observed, due to the significantly higher number of nuclei formed in the mixing chamber. Analogously to the lower nucleation and growth temperature, additional growth of the regular NCs was observed, when the spectra after 5 s and 15 s were compared. In the case of the intermediate temperature combination (B), the size distribution of the regular NCs did not seem to change significantly within the additional 10 s of residence time, while the cluster population remained high. This indicates, that under these reaction conditions, all growth steps occur via size-focussing, rather than Ostwald ripening, as the monomer concentration remains high and cluster formation from previously formed nuclei is faster than the formation of regular NCs.

In the case of the higher temperature combination (C), the onset of Ostwald ripening was observed, as discussed in the previous section. The growth of the high amount of nuclei formed at this nucleation temperature, causes a sufficient depletion of monomer concentration, to significantly impede NC growth. In consequence, continuous growth is slowed, while the NCs' size distribution broadens. As this process is still relatively slow at this temperature, some magic-sized intermediates still remain within the first 15 s of the reaction. This time-resolved comparison corroborates, that this temperature combination is on the verge of the high-temperature

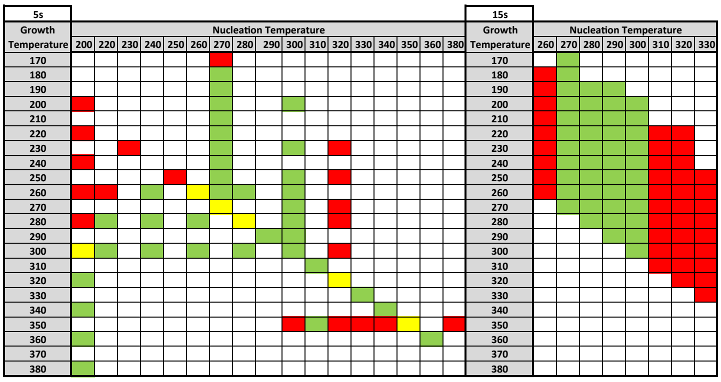

5s																	
Growth Temperature	Nucleation Temperature																
	200	220	230	240	250	260	270	280	290	300	310	320	330	340	350	360	380
170							🟥										
180							🟩										
190							🟩										
200	🟥						🟩			🟩							
210							🟩										
220	🟥						🟩										
230			🟥				🟩			🟩		🟥					
240	🟥						🟩										
250					🟥		🟩			🟩		🟥					
260	🟥	🟥		🟩		🟨	🟩	🟩		🟩							
270							🟨			🟩		🟥					
280	🟥	🟩		🟩		🟩		🟨		🟩		🟥					
290									🟩	🟩							
300	🟨	🟩		🟩		🟩		🟩		🟩		🟥					
310											🟩						
320	🟩											🟨					
330													🟩				
340	🟩													🟩			
350										🟥	🟩	🟥	🟥	🟥	🟨		🟥
360	🟩															🟩	
370																	
380	🟩																

15s								
Growth Temperature	Nucleation Temperature							
	260	270	280	290	300	310	320	330
170		🟩						
180	🟥	🟩						
190	🟥	🟩	🟩	🟩				
200	🟥	🟩	🟩	🟩	🟩			
210	🟥	🟩	🟩	🟩	🟩			
220	🟥	🟩	🟩	🟩	🟩	🟥	🟥	
230	🟥	🟩	🟩	🟩	🟩	🟥	🟥	
240	🟥	🟩	🟩	🟩	🟩	🟥	🟥	
250	🟥	🟩	🟩	🟩	🟩	🟥	🟥	🟥
260	🟥	🟩	🟩	🟩	🟩	🟥	🟥	🟥
270		🟩	🟩	🟩	🟩	🟥	🟥	🟥
280			🟩	🟩	🟩	🟥	🟥	🟥
290				🟩	🟩	🟥	🟥	🟥
300					🟩	🟥	🟥	🟥
310						🟥	🟥	🟥
320							🟥	🟥
330								🟥
340								
350								
360								
370								
380								

Figure 5.10.: Formation conditions of $CdSe_{437}$: combination of nucleation and growth temperature at which $CdSe_{437}$ was observed after growth in 10 cm (A) and 50 cm (B) oven. Green boxes indicate observation of the respective absorption feature, red boxes indicate no observation. Yellow boxes indicate, that the absorption feature has been observed in some experiments and in others not.

regime discussed in section 5.2.1.

5.2.4. Formation Conditions of MSC Species

Within the previous sections, it became clear, that cluster species were primarily observed within a certain temperature window. In order to summarize, and visualize these observations, an overview of the combinations of nucleation and growth temperatures, at which MSCs were observed in this work, is shown in figure 5.10. This overview is limited to the presence of $CdSe_{437}$, as the absorption peak of $CdSe_{403}$ could not always be definitely identified.

The presence of an absorption peak corresponding to $CdSe_{437}$ in the recorded spectra is denoted with a green box in the figure, while its absence under these conditions are denoted with a red box. A yellow box indicates, that the feature were observed in some experiments and not in others. The figure contains information for both the 10 cm and 50 cm oven, corresponding to residence times of 5 s and 15 s respectively.

Generally, temperatures between 260 °C and 300 °C were beneficial for cluster observation within the respective time frames. At nucleation temperatures within this range, even at growth temperatures far lower, some magic-sized intermediates were observed, as the nuclei concentration resulted in suitable cluster formation rates. At very low nucleation temperatures, clusters were also observed at growth temperatures up to 380 °C. This could possibly due to secondary nucleation, however, as the number of nuclei formed at the respective temperatures should be negligible.

While the cluster species also form as intermediates in the growth of regular NCs at different temperatures, the combination of oven and nucleation and growth temperatures shown in the figure, allowed direct preparation of NC solutions containing significant populations of MSCs.

5.2.5. Conclusion of Nucleation and Growth Experiments

In the nucleation and growth experiment presented within this section, evidence of MSCs formed during the formation of and growth of regularly growing NCs was observed repeatedly. The evolution of UV/Vis absorption spectra with variation of nucleation and growth temperature, as well as reaction time, suggested a reaction pathway starting with the formation of nuclei in the mixing chamber and subsequent sequential growth of different-size moieties of MSCs and ending in the formation and subsequent continuous growth of regular NCs.

Through variation of the nucleation temperature, the nucleation rate in the mixing chamber could be influenced, resulting in larger nuclei concentrations being formed at higher nucleation temperatures. Based on the level of nuclei concentration, larger - or smaller - populations of MSC intermediates could be observed after the residence time at a given growth temperature. More importantly, though, higher nuclei concentrations resulted in increased growth rates for all reaction steps in the sequential growth mechanism.

Based on this, three different growth regimes could be identified:

- A low nucleation temperature regime, where MSC intermediates were only observed at early reaction times, as their low number, accompanied by a high monomer concentration, resulted in fast depletion of MSCs through growth into regular NCs under size-focussing conditions.
- An intermediate nucleation temperature regime, where a high number of nuclei caused fast growth of MSCs and their comparably large number caused sufficient depletion of monomer during their sequential growth,slowing down the

subsequent growth into regular NCs. This resulted in intermediate accumulation of the MSCs and subsequent observation after the investigated residence times.

- A high nucleation temperature regime, where the very large number of nuclei formed caused rapid growth into regular NCs. The larger number of growing particles resulted in rapid depletion of monomer concentration, and subsequent onset of growth via Ostwald ripening.

While the observation of MSCs at low nucleation temperatures is possible at short reaction times, their observation at high nucleation temperatures is very difficult due to their extremely rapid growth into regular NCs and their rapid depletion due to the NCs' growth via Ostwald ripening. The progress between these two extreme cases within the intermediate temperature regime occurs continuously. With increasing nucleation temperature and subsequent increase of nuclei concentration, the onset of Ostwald ripening can be observed at earlier stages.

Variation of the growth temperature affected the NC growth less drastically. As expected, an increase in growth temperature led to an increase in reaction rate over all steps of the sequential growth process. As a consequence, population increases of larger cluster species and regular NCs, as well as growth to larger average size of regular NCs was observed with increasing growth temperature. At the same time, the onset of Ostwald ripening could be observed earlier at higher growth temperatures, due to the faster monomer consumption.

Finally, the combinations of reaction time, and nucleation and growth temperature at which maximum cluster populations were observed, could be identified as suitable conditions to directly prepare cluster solutions.

5.3. Optical Characterization of Cluster Solutions

In order to confirm the assignment of the different absorption features, observed in previous experiments, to independent species, attempts were made to isolate them. For this purpose, a CdSe NC solution was synthesized under reaction conditions previously determined to yield different absorption features, including the ones assigned to MSCs (see section 8.3.1, cluster preparation experiment 1). The UV/Vis absorption spectrum of the resulting yellow solution after separation from its colorless precipitate by centrifugation and subsequent filtration is shown in black in figure 5.11 (A). It possesses three distinct absorption features at 384 nm, 437 nm and 467 nm and one broad feature at around 350 nm.

A size-selective precipitation procedure (section 8.3.2) comprising stepwise addition of nonsolvent (ethanol in this case) and subsequent centrifugation yielded five fractions (F1 through F5) the normalized UV/Vis absorption spectra of which are shown in figure 5.11 (A). The spectral position of the peaks is given in table 5.1. The reduction of intensity and subsequent disappearance of the longer-wavelength absorption features with increasing amount of nonsolvent and centrifugation steps indicates that the initial sample is indeed composed of different-size species of nanoparticles, giving rise to the different absorption features.

The features at 437 and 467 nm can be assigned to two distinct species of different-size nanoparticles, as their intensity ratio varies between F1 and F2 and they are absent in later fractions. The features around 405 nm appear to be caused by several species of similar size, causing the irregular shape and broadness of the peak and the shift of the maximum to a shorter wavelength between F3 and F4. These features coincide with literature reports of CdSe MSCs which have been reported between 408 nm and 418 nm.[117] However, the simultaneous presence of several of these species has not been reported.

The high-energy features of the spectrum of the initial fraction also appear in the spectrum of F5, albeit shifted to longer wavelengths. CdSe MSCs have been reported around 350 nm, as well as in the range of 380 nm to 393 nm coinciding with the absorption maxima observed in the present spectra. The dual nature of these features is reminiscent of the families of MSCs first reported by Ouyang *et al.*.[112] It is unclear however, what is the cause of the observed shift between Fi and F5, although a transformation from $CdSe_{384}$ to $CdSe_{393}$ caused by a change in equilibrium due to the removal of the larger clusters could be conceivable.

In order to further differentiate between the different species contributing to the absorption spectrum, PL spectra of the different fractions were obtained. Figure 5.11 (B) shows the PL spectra of fraction F1 at excitation wavelengths corresponding to the two main absorption features (435 and 465 nm)[1] and at one much shorter

---

[1] The slight shift of the absorption maxima compared to the values in table 5.1 can be attributed to surface oxidation, as the sample was stored in air for 20 days between the measurements.

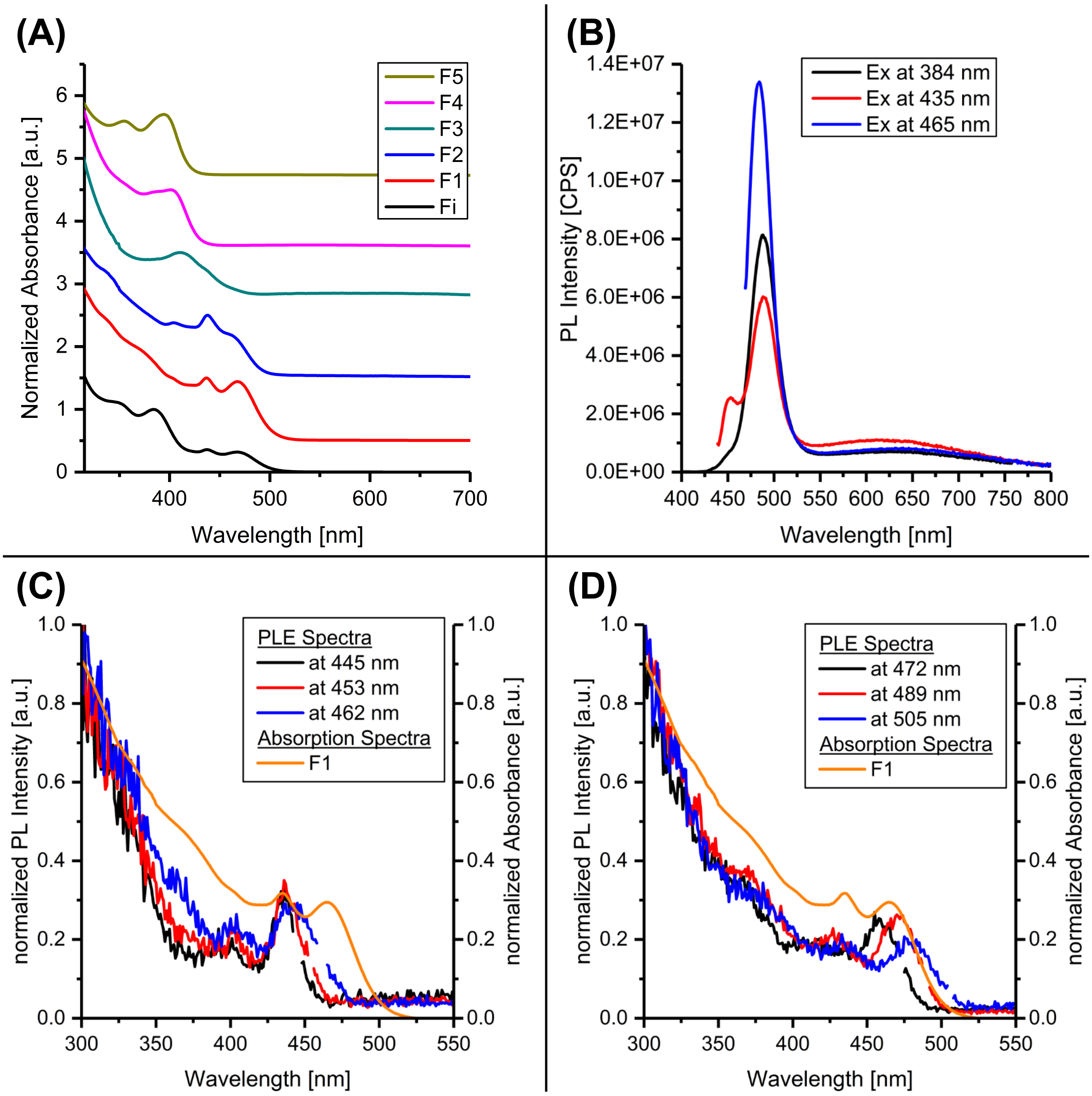

Figure 5.11.: Evidence of MSC species: (A) UV/Vis absorption spectra of the different fractions of a CdSe nanocluster solution obtained via size-selective precipitation, (B) PL spectra of fraction F1 at different excitation wavelengths, (C) and (D) PLE spectra at different wavelengths and absorption spectrum of fraction F1.

Table 5.1.: UV/Vis absorption peaks in spectra of different fractions in figure 5.11 (A). Values marked with an asterisk (*) indicate broad features likely composed of multiple peaks.

Fraction	λ_{max} / nm
Fi	350*, 384, 437, 467
F1	437, 467
F2	405, 437, 467
F3	405-415*
F4	405*
F5	355, 393*

wavelength (384 nm). While excitation at all three wavelengths yielded an emission peak at 489 nm, excitation at 435 nm resulted in an additional emission peak at 453 nm. A similar observation was made for fractions Fi and F2, although the ratio of $\frac{I_{453}}{I_{489}}$ was higher for F2, corresponding to the higher intensity ratio of the respective peaks in the absorption spectrum. Fractions F3 and higher showed little to no emission, indicating that the emission observed from samples Fi to F2 is only due to the larger species.

As the presence of the emission peak at 453 nm in the PL spectrum obtained at 465 nm excitation wavelength can not be ruled out, the sample F1 was further investigated using PLE spectroscopy. PLE spectra were obtained at both observed PL maxima, as well as at both HWHM wavelengths each. In the case of the PL peak at 453 nm the longer-wavelength HWHM could not be determined, due to its overlap with the larger emission peak. As a result the PLE spectrum was recorded at 462 nm, the lowest point of the overlap between the two peaks. All six PLE spectra are shown in figure 5.11 (C) and (D). The measured intensity at and around the respective detection wavelength was masked, resulting in the visible gaps in the spectra.

The PLE spectra obtained at 445 nm, 453 nm and 462 nm show their maxima at or very close to 435 nm, the second maximum in the UV/Vis absorption spectrum, whereas the maxima of the PLE spectra obtained at 472 nm, 489 nm and 505 nm are spread out over a range of over 20 nm around the first maximum in the UV/Vis absorption spectrum at 465 nm. While this clearly shows the correlation of the two emission peaks with their respective absorption features and thus further confirms the presence of two distinct species, it could even be interpreted as an indication to the size distribution of the two species. The emission peak at 453 nm shows maximal intensity if the sample is irradiated with light possessing a wavelength very close to 435 nm, indicating that it originates from a single species of NC of narrow size distribution, like a MSC. The emission intensity at the flanks of the peak at 489 nm however can be maximized by exciting at wavelengths different from the absorption maximum, indicating that the emission is due to a population of NCs with a broader size distribution.

In conclusion: using a size-selective precipitation technique, it could be shown, that the different features in the UV/Vis absorption spectra of so-called cluster solutions were in fact due to a series of different-size species of NCs. The spectral position of their absorption peaks fits previous reports of MSCs, which could be formed as intermediates during the formation of the first cluster species observed in the nucleation and growth experiments in this section. The broad full width at half-maximum (FWHM) of the respective features casts doubts on this assignment, however, making the role of these species in the previously discussed growth mechanism unclear.

Analysis of the emission properties of the two largest species of NCs further confirmed that separate species were observed. Interpretation of PLE spectra of these species additionally suggests that the absorption feature observed at 435 nm/437 nm is due to a species of MSC, while the feature observed at 465 nm/467 nm is due to regular NCs. Alone, the results of the PLE measurements might not be sufficient proof for this assignment, they do, however, support the previously made assumptions based on the observed growth behavior of the respective species of CdSe NCs.

6. The Growth of Magic-Sized CdSe Clusters

In the nucleation and growth experiments presented in the previous chapter, UV/Vis absorption peaks were observed that did not shift in wavelength with reaction temperature or time, but only in intensity, relative to each other and to the continuously growing NCs. Due to this behavior, they were assigned to species of MSCs formed as intermediates in the formation of continuously growing NCs. Based on the variation of the nucleation temperature and the resulting difference in nuclei concentration, three different reaction pathways via two observed magic-sized intermediates were identified. Resulting from the increased monomer consumption of a higher number of growing nuclei, as well as their faster growth rate, the shift from particle growth under pure focussing conditions towards growth via ripening occurred earlier at higher nucleation temperatures.

In order to study the sequential growth of one MSC species into another in more detail, a variation of the previously employed nucleation and growth experimental procedure was implemented. This cluster growth procedure avoided the significant influence of the nucleation temperature, by pumping a preprepared NC solution containing MSCs directly through a growth oven heated to the desired growth temperature. This allowed a direct variation of the growth rate via the growth temperature, without the influence of varying nuclei concentrations. Instead the focus of the experiments was to investigate the growth progress in a time-resolved approach by using different growth ovens.

Using this revised protocol, the refined concept of the sequential growth behavior of the MSCs is presented in the following. In the first part of this chapter, this experimental procedure is applied to CdSe NC solutions containing MSC intermediates, following the sequential growth of the MSCs. In the second part, a NC solution containing no magic-sized intermediates is used, and the consequential continuous growth of the NCs following the classical growth model is discussed.

6.1. Time-resolved Study of Magic-Sized CdSe Cluster Growth Behavior

Initially, the growth of CdSe MSCs in presence of excess monomer was studied. The presence of free monomer allowed growth under incorporation of monomer, i.e. within the focussing regime. For these experiments, a CdSe NC solution containing MSC intermediates was prepared in the CFD and used as precursor solution in the previously described cluster growth experiment. Subsequently, cluster growth in the absence of excess monomer, i.e. under pure ripening conditions, was studied using a cluster solution previously purified by several cycles of precipitation and redispersion using the same experimental protocol.

6.1.1. Cluster Growth in the Presence of Excess Monomer

A CdSe NC solution, previously preprared in a separate nucleation and growth experiment using a 10 cm growth oven and collected over an extended time period, was used as a precursor solution in this experiment. The solution was prepared under conditions previously determined to yield magic-sized intermediates alongside regular NCs within the crude product. This product was used directly, without prior purification. In consequence, it still contained a significant excess of free monomer and a similar growth behavior as observed in the previous nucleation and growth experiments was expected. This means a sequential growth of several different-size species of MSCs into each other and subsequently the continuous growth of the largest cluster species into the regularly growing NC. If any nuclei remained within the solution, after the initial growth during the cluster synthesis, they would be expected to grow into the first cluster species.

The cluster solution (cluster solution 1 in section 8.3.1) was pumped using a continuous pump, set at a flow rate of 1 mL/ min in order to conserve cluster solution. The solution was pumped through a growth oven with a length of 10 cm and in a separate experiment through one with a length of 50 cm, resulting in residence times of 7.84 s and 26.68 s. The temperature of the ovens was varied throughout the

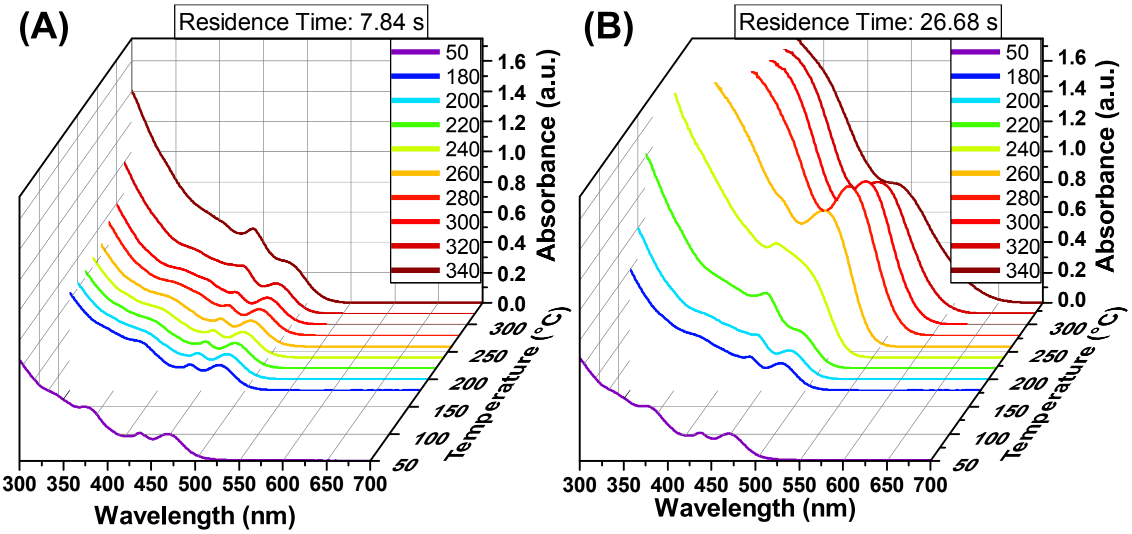

Figure 6.1.: UV/Vis absorption spectra of CdSe cluster solutions after growth at different temperatures at a total flow rate of 1 mL/ min: (A) in a growth oven of 10 cm resulting in a residence time of 7.84 s, (B) in a growth oven of 50 cm resulting in a residence time of 26.68 s.

experiment in order to vary the growth rate. The crude product of the reaction was investigated using UV/Vis absorption spectroscopy in the optical flow cell with a path length of 0.5 mm.

Figure 6.1 (A) shows the UV/Vis absorption spectra obtained after growth in the 10 cm growth oven and figure 6.1 (B) after growth in the 50 cm growth oven. After both 7.84 s and 26.68 s at 50 °C the spectra exhibited a peak at 380 nm, 437 nm and 470 nm and some modulation at lower wavelength potentially indicating the presence of smaller cluster species.

The increase in OD and the variation in relative intensity between the individual absorption features with an increase in temperature shows the increase of the growth rate with temperature already after a reaction time of 7.84 s. Due to the short residence time, this effect is small at temperatures below 300 °C. After an additional 18.84 s of growth the influence of the temperature is more evident, as definite signs of continuous growth of regular NCs can be identified at growth temperatures above 220 °C. At lower temperatures, mostly sequential growth from smaller cluster species to larger ones was observed, indicated by the variation in relative intensity of the absorption peaks. Figure 6.2 gives a more detailed overlook of the experiment. In it the UV/Vis absorption spectra obtained after both residence times are plotted together for each growth temperature, allowing a more direct comparison of the reaction progress with time.

No significant change with reaction time was observed at a growth temperature of 50 °C, with the spectra exhibiting absorption peaks at 380 nm, 437 nm and 470 nm (figure 6.2 (A)). Increasing the growth temperature to 180 °C yielded a different result (figure 6.2 (B)). While the spectrum obtained after 7.84 s of reaction time had not changed significantly, the measurement conducted after 26.68 s saw a flattening of the peak at 380 nm together with a simultaneous increase of OD at 437 nm. The reason for this is the growth of $CdSe_{380}$ into $CdSe_{437}$, which occurs more rapidly at elevated temperature, while some formation of $CdSe_{380}$ from smaller species appears to occur still. A slight increase of intensity at the particle peak indicates that growth into regular NCs occurs only slowly at this temperature.

At 200 °C of growth temperature the spectra (figure 6.2 (C)) showed a significant increase in OD at 437 nm and below, with progressing reaction time. Some evidence of the smaller species $CdSe_{380}$ could still be observed after 26.68 s, indicating that the smaller species growing into this species had not yet been depleted. At the same time, the accelerated growth into $CdSe_{437}$ caused the further flattening of the absorption feature at 380 nm, while the one at 437 nm gained in intensity. A slight increase in intensity of the peak at 470 nm indicated the onset of continuous growth based on this species at this temperature.

A further increase of growth temperature to 220 °C (figure 6.2 (D)) caused a significant increase in OD at 437 nm in the investigated time frame. Simultaneously the remaining absorption feature around 380 nm had disappeared and the peak at 470 nm had increased in OD and appeared broadened and shifted to longer wavelength. This observation suggests a complete depletion of $CdSe_{380}$ and the previously existing smaller species. At the same time, the formation of $CdSe_{437}$ from the smaller species appears to be greatly favored at this temperature and in this time frame. The subsequent growth into the continuously growing species is also accelerated.

While a further increase in growth temperature to 240 °C still caused no significant change in the spectrum obtained after 7.84 s, the one obtained after 26.68 s showed a picture of a much more advanced reaction state than the previous spectra (figure 6.2 (E)). The OD at 470 nm had increased significantly and the absorption peak present after 7.84 s appeared significantly broadened to a point where no clear maximum could be discerned, as the peak appeared to intersect with the one at 437 nm, which

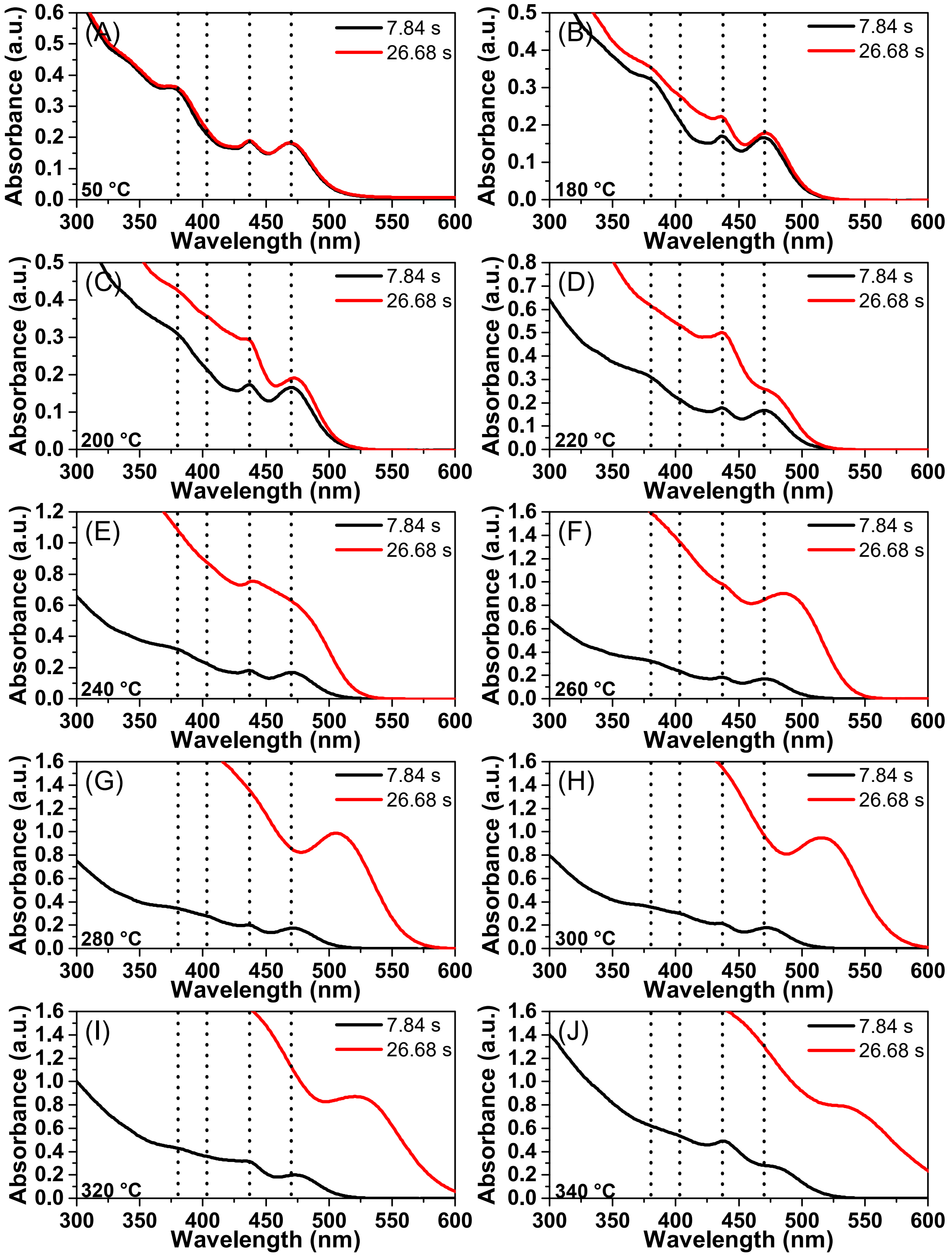

Figure 6.2.: Comparison of UV/Vis absorption spectra of CdSe cluster solutions at both residence times and at different growth temperatures. The dashed markers indicate the absorption maxima of CdSe species observed in the experiment. They mark 380 nm, 403 nm, 437 nm and 470 nm.

appeared less pronounced. Evidently, continuous growth of the regular NCs under incorporation of free monomer sets in at this temperature (within the observed time frame), as the absorption onset is shifted considerably towards longer wavelength with increasing residence time.

At higher growth temperatures the spectra obtained after 26.68 s showed a distinct absorption peak, which was continuously shifted to longer wavelength with increasing temperature. While its maximum OD increased up to a growth temperature of 280 °C (figure 6.2 (G)) it decreased with increasing growth temperature above that, simultaneous with an increase in width of the absorption feature. Clearly, at this stage, the free monomer still available had already been consumed by the very rapid growth reaction at this temperature. In consequence, particle growth occurred via Ostwald ripening, rather than size-focussing.

At a growth temperature of 280 °C, the growth of $CdSe_{437}$ into larger species is fast enough, to cause a complete depletion of its population with in the 26.68 s of residence time. At this temperature, the sequential growth cascade already starts within the first 7.84 s of the reaction, as the spectrum shows increased OD around 400 nm, indicating the formation of an intermediate cluster species. With a further increase in growth temperature, the growth rates along the sequential growth pathway are sufficiently high, to shift large portions of this reaction cascade into the first 7.84 s of the reaction. As a consequence, the sequential increases and decreases of different-size cluster species populations could be observed within the respective spectra with increasing growth temperature between 280 °C and 340 °C.

The cluster solution used in this experiment was produced in a nucleation and growth experiment using a 10 cm growth oven, a total flow rate of 2 mL/ min and a nucleation, as well as growth temperature of 280 °C. This means, the particles had already undergone growth in the intermediate temperature growth regime, as discussed in the previous chapter, for 5 s before the cluster growth experiment commenced. In consequence, the additional residence time in the growth ovens during this experiment, was an extension of the growth period compared to the results discussed above. Based on this, it is not surprising, that the magic-sized intermediates have been depleted at lower temperatures than in the experiments discussed in section 5.2.2, as the reaction time has been much longer and their concentration is already reduced due to the previous growth. Nevertheless, sequential growth of one cluster species into the other could be observed in this experiment, as postulated in the growth mechanism in section 5.2.1.

The MSC intermediates observed in this and the previous experiments possess a lower chemical potential than particles of slightly larger, or smaller, size. In consequence, in a plot of chemical potential versus radius (like figure 2.5), distinct minima exist at the radii of the MSCs. The depth of these potential wells depends on the stability of the respective cluster. In general, a smaller cluster will be less stable than a larger one, due to the higher surface-to-volume ratio. As a result, less energy is required to promote growth of a small cluster into a medium-size one than to promote growth of a medium-size cluster into a larger one. Correspondingly, growth of $CdSe_{380}$ into $CdSe_{437}$ is observed within the investigated time frame at temperatures as low as 180 °C. Further growth of $CdSe_{437}$ is then only observed at temperatures above 200 °C.

Continuous growth of regular NCs clearly set in at 240 °C during this experiment. But also after 26.68 s at 220 °C a slight red shift of the absorption peak at 470 nm accompanied by an increase in intensity indicates continuous growth of the corresponding species of CdSe under incorporation of free monomer. Based on observations during previous experiments (e.g. section 5.2.3), it can be assumed, that this species of $CdSe_{470}$ is a species of regular NCs formed during the cluster synthesis. With the onset of continuous growth, both the largest cluster species, $CdSe_{437}$, as well as these previously formed NCs begin to grow. This is especially evident from the spectrum obtained after 26.68 s of growth at 240 °C. Here, an odd shape of the absorption maxima is observed, as the spectrum exhibits the distinct peak of $CdSe_{437}$, together with the broad maxima of the regular NCs growing from it and the equally growing preformed regular NCs. As long as the NCs grow under focussing conditions, i.e. in the presence of sufficient free monomer, the sizes of the two populations of NCs are eventually focussed into one, as the smaller NCs grow faster. This is indicated by the formation of one distinct absorption peak after growth at 260 °C, the FWHM of which narrows, after the growth temperature was increased to 280 °C. As stated before, at higher temperatures, the reaction progresses so quickly, that the free monomer had been used up after 26.68 s of growth, so that further growth had to occur via Ostwald ripening, as indicated by the broadening size distribution after growth at 320 °C and 340 °C.

The onset of continuous growth based on $CdSe_{437}$ was observed at higher temperatures than the previous sequential growth of the different-size MSCs. This was on the one hand, due to the high stability of the cluster requiring higher temperature to promote further growth (as stated above) and on the other hand due to the increased growth rates at higher temperature allowing the observation of this last step in the sequential growth process within the observed time frame. However, the onset of the growth of the regular NCs was also observed at higher temperatures than the growth of the small clusters, although its growth rate was not affected by the previous sequential growth process. It stands to reason, that the activation energy of this process is also larger than that of the growth of the small clusters, due to the latter's large chemical potential.

6.1.2. Cluster Growth in the Absence of Excess Monomer

In order to directly study the growth of the NCs under pure ripening conditions, a growth experiment was carried out using a purified cluster solution, instead of the crude product used in the previously described experiment. Initially, preliminary experiments were carried out to find a suitable solvent for the clusters after purification, as an earlier attempt to isolate individual cluster species via size-selective precipitation had failed due to the long-term insolubility of the NCs in the selected solvent (ODE). In a second step, the particles' ability to grow in the absence of free monomer had to be established.

A solubility test showed that NCs from cluster growth solution 2 (compare section 8.3.1), purified as described in section 8.3.4, could be dispersed readily in a mixture of solvents (Cyanex, TOP, and ODE) of equal composition as the reaction mixture used in the CFD, and in ODE after some agitation. Both resulting solutions were used in a batch growth experiment, in which the solution in ODE showed no particle growth, whereas the solution in the solvent mix showed significant growth of the particles. TEM images showed the particles to be agglomerated into large aggregates. Subsequently the experiment was repeated with shorter reaction times: 30 s and 60 s instead of five minutes at 250 °C in the flask.

Figure 6.3 (A) shows the UV/Vis absorption spectra of the cluster solution after purification and redispersion in the solvent mix (black trace, as well as after 30 s and 60 s of growth at 250 °C. Growth of the previously existing multiple species of clusters into regular NCs (including an absorption maximum related to a higher energy transition in the spectrum) could be observed. No indication towards a

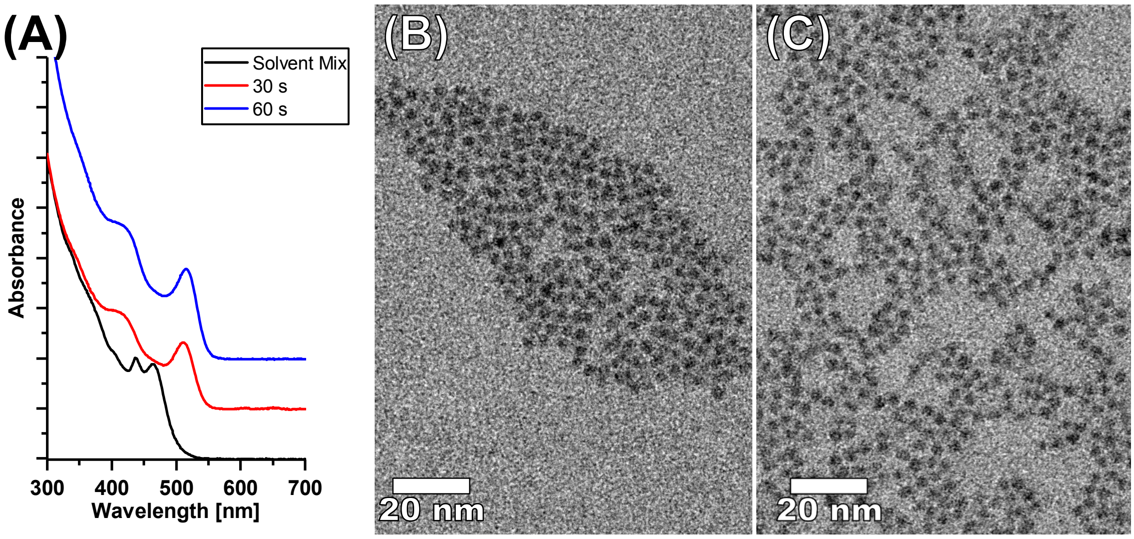

Figure 6.3.: Results of preliminary purified cluster growth experiment: (A) UV/Vis absorption spectra of CdSe nanoparticles in solvent mix and after 30 s, 60 s and five minutes at 250 °C; (B) and (C) TEM images of CdSe nanoparticles after 30 s and 60 s at 250 °C.

variation in size between 30 s and 60 s of growth time could be determined. TEM images after both reaction times (figure 6.3 (B) and (C)) showed roughly spherical NCs of narrow size distribution exhibiting no signs of agglomeration.

Following the successful growth of purified CdSe clusters in a batch experiment, the growth experiment in the CFD was repeated using cluster growth solution 3 (section 8.3.1) purified via three cycles of precipitation, centrifugation and redispersion as described in section 8.3.4. The UV/Vis absorption spectra of the solution before and after the purification is shown in figure 6.4. According to these, the solution contains a population of $CdSe_{437}$ as well as a second species at around 465 nm. The purification procedure resulted in a reduction in optical density, which can probably be correlated with a reduction in scattering due to turbidity in the sample prior to purification. Apart from that only a very slight shift to longer wavelength of the peak previously centered at 437 nm could be observed.

The growth experiment was conducted analogously to the previous one with a continuous pump, set to a flow rate of 1 mL/ min in order to save cluster solution and an optical flow cell of 0.5 mm optical path length. In order to obtain a comprehensive overview of the reaction progress, this experiment saw the use of four different growth ovens with lengths of 10 cm, 30 cm, 50 cm and 90 cm resulting in residence

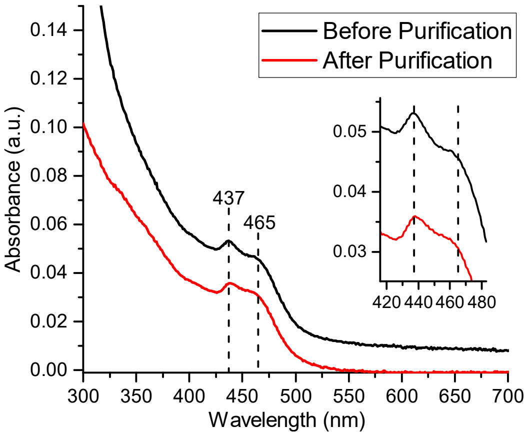

Figure 6.4.: UV/Vis absorption spectra of cluster solution 3 before purification (black trace) and after purification and redispersion in solvent mix (red trace). The inset shows an enlarged view of the absorption features. Highlighted are the wavelengths assigned to the maximum of the absorption features before purification.

times of 7.84 s, 17.26 s, 26.68 s and 45.52 s. The UV/Vis absorption spectra obtained after these four reaction times at different growth temperatures are shown in figure 6.5. The dashed lines mark the previously observed absorption features centered at 437 nm and 465 nm. Note that the drop in OD at wavelengths below 325 nm is due to the use of a previously obtained reference spectrum.

At 50 °C no significant deviation from the previously obtained spectrum (figure 6.4) could be observed (figure 6.5 (A)). Increasing the growth temperature to 150 °C resulted in an improved resolution of the two absorption features, with no significant difference between the four residence times (figure 6.5 (B)). The feature at 437 nm showed a higher intensity than the one at 465 nm. At a growth temperature of 200 °C the onset of the growth reaction could be observed (figure 6.5 (C)). After 45.52 s of reaction time a slight reduction in the population of $CdSe_{437}$ is observed as a decrease in peak OD of the respective absorption feature. The increase of the growth temperature by an additional 20 °C led to further reduction of the OD_{437} along with a slight shift of the peak previously located at 465 nm after a residence time of 45.52 s (figure 6.5 (D)). In addition a change in the slope of the OD at wavelengths between 300 nm and 400 nm could be observed. No changes were observed for the lower residence times at this temperature.

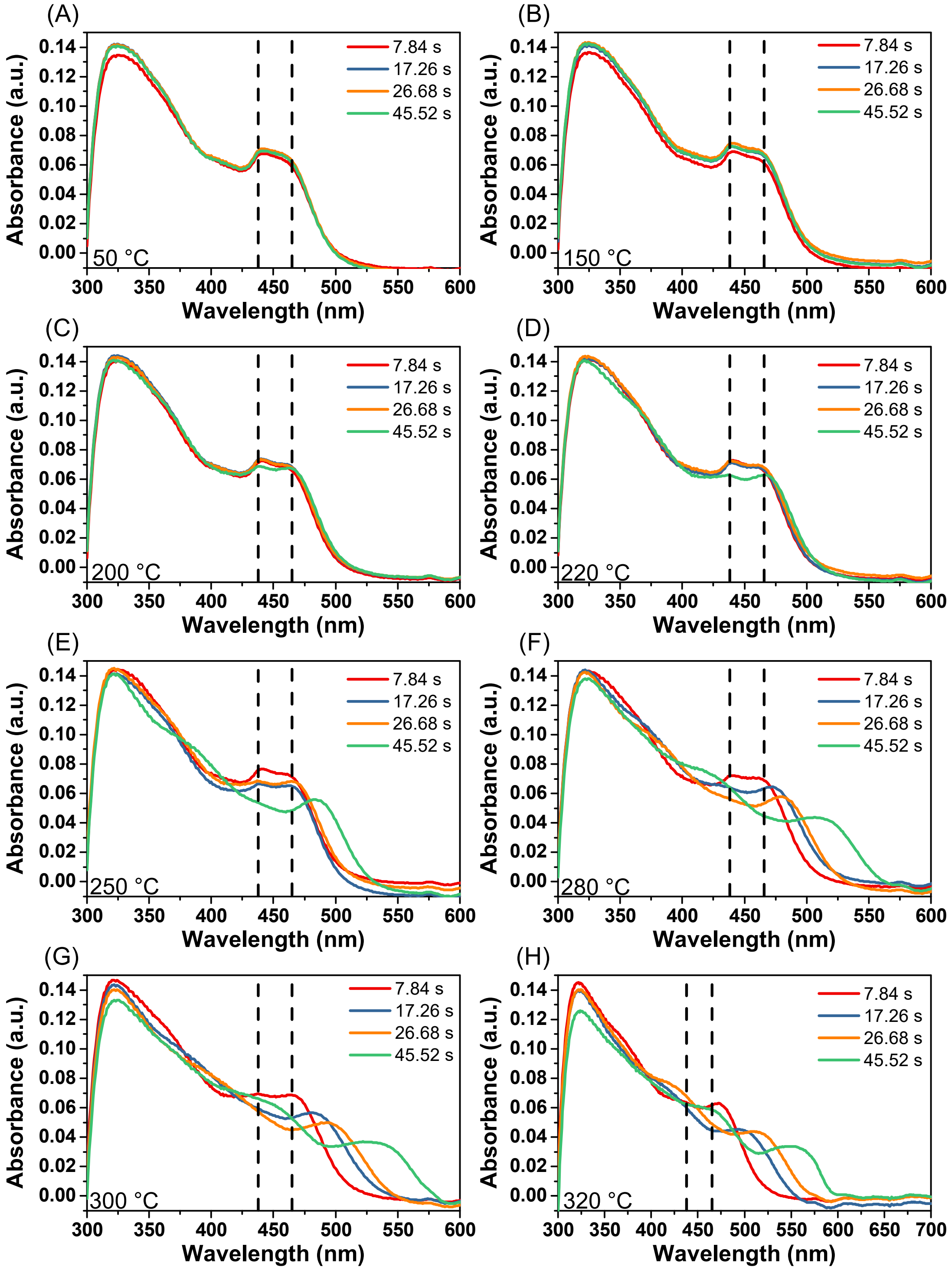

Figure 6.5.: UV/Vis absorption spectra of purified cluster solution after four different reaction times at eight different temperatures. Dashed lines mark the previously observed absorption features at 437 nm and 465 nm.

At a growth temperature of 250 °C the absorption maximum at 437 nm has disappeared, whereas the lower energy peak has strongly shifted to longer wavelength after a reaction time of 45.52 s Additionally a second excitonic transition was easily discernible on the absorption spectrum, a feature which had so far only been observed for regular NCs and not for MSC. At lower reaction times the onset of the reaction could be observed as well at this temperature. While, after 7.84 s at 250 °C no significant difference to the original spectrum could be observed, after 17.26 s the OD at the two maxima had approximately equalled, and after 26.68 s the OD at 465 nm exceeded that at 437 nm. This observation could indicate that the population of $CdSe_{465}$ grows, following the dissolution of $CdSe_{437}$ and prior to the onset of continuous growth.

At higher growth temperatures continuous growth accompanied by broadening of the absorption peak was observed with increasing residence times. This observation is characteristical of Ostwald ripening, which is due to the absence of free monomer, as all monomer liberated from the dissolution of the smaller clusters has been consumed by the growing particles at this stage. For the lower residence time a decrease in OD_{437} was observed at 280 °C, which had nearly vanished at 300 °C. Continuous growth was then finally observed clearly at 320 °C.

Under pure ripening conditions, growth of larger particles is faster than growth of smaller particles. Due to the shift of the critical radius to high values at low monomer concentrations, smaller particles dissolve, while the thusly liberated monomer is incorporated into the growing larger particles. This behavior is observed directly in the present experiment. At sufficiently high temperatures, to activate the dissolution of $CdSe_{437}$, the larger species of CdSe NCs begins to grow continuously. This happens slowly at lower temperature (200 °C and 220 °C) and more rapidly at higher temperatures (250 °C and above), as the thermal energy accelerates the dissolution of the magic-sized intermediate.

A pivotal experiment is the one conducted at a growth temperature of 250 °C, where the onset of this reaction can be observed in the investigated time frame. Initially, the dissolution of the smaller cluster liberates monomer (between 7.84 s and 17.26 s) which is subsequently incorporated into the larger NCs, evident by the increasing intensity of the absorption feature at 465 nm. From the evolution of the spectra, it can be deduced, that the dissolution occurs slightly faster than the incorporation of the liberated monomer into the larger crystals. Within the final

18.84 s of the investigated reaction time, the population of $CdSe_{437}$ is completely depleted and the NCs continue growing via the ripening mechanism. As is evident from the vastly broadening size distribution with reaction time at higher growth temperatures, the depletion of the monomer liberated from the dissolved MSCs causes the smaller NCs to dissolve, while the growth of the larger ones is significantly accelerated.

This growth mechanism is very different from the growth under focussing conditions. In the presence of a larger species of nanoparticles, the MSC $CdSe_{437}$ dissolves and the liberated monomer is incorporated into the larger CdSe species, in a continuous growth process. Under focussing conditions, continuous growth of this largest cluster species occurs directly under incorporation of free monomer, even in the presence of a larger species of regular NCs, as was discussed in the previous section (section 6.1.1). This distinct differentiation between focussing and ripening regime, supports the previously made assumptions about the onset of the ripening phase based on the presence of the cluster peaks.

6.2. Time-resolved Study of Regular CdSe Nanocrystal Growth Behavior

As a frame of reference, the growth experiment from preprepared NC solution was also conducted using a solution containing no MSCs but only regular NCs. In this experiment, an unpurified CdSe cluster growth solution (solution 4 in section 8.3.1) was pumped through growth ovens with a length of 10 cm, 16 cm, 30 cm, 50 cm, 75 cm and 90 cm at a flow rate of 1 mL/ min, resulting in residence times of 7.84 s, 10.67 s, 17.27 s, 26.68 s, 38.46 s and 45.52 s. As the solution was not purified before use, it contained significant amount of free monomer, allowing growth under focussing conditions.

Figure 6.6 (A) shows the UV/Vis absorption spectrum of the NC solution obtained at 80 °C in the CFD before any evidence of reaction was observed. The spectrum exhibited a distinct absorption maximum at 454 nm with additional maxima related to higher energy transitions but none of the characteristic absorption peaks of the MSC species observed in the other experiments.

At a temperature of 120 °C in the growth oven no variation in the absorption

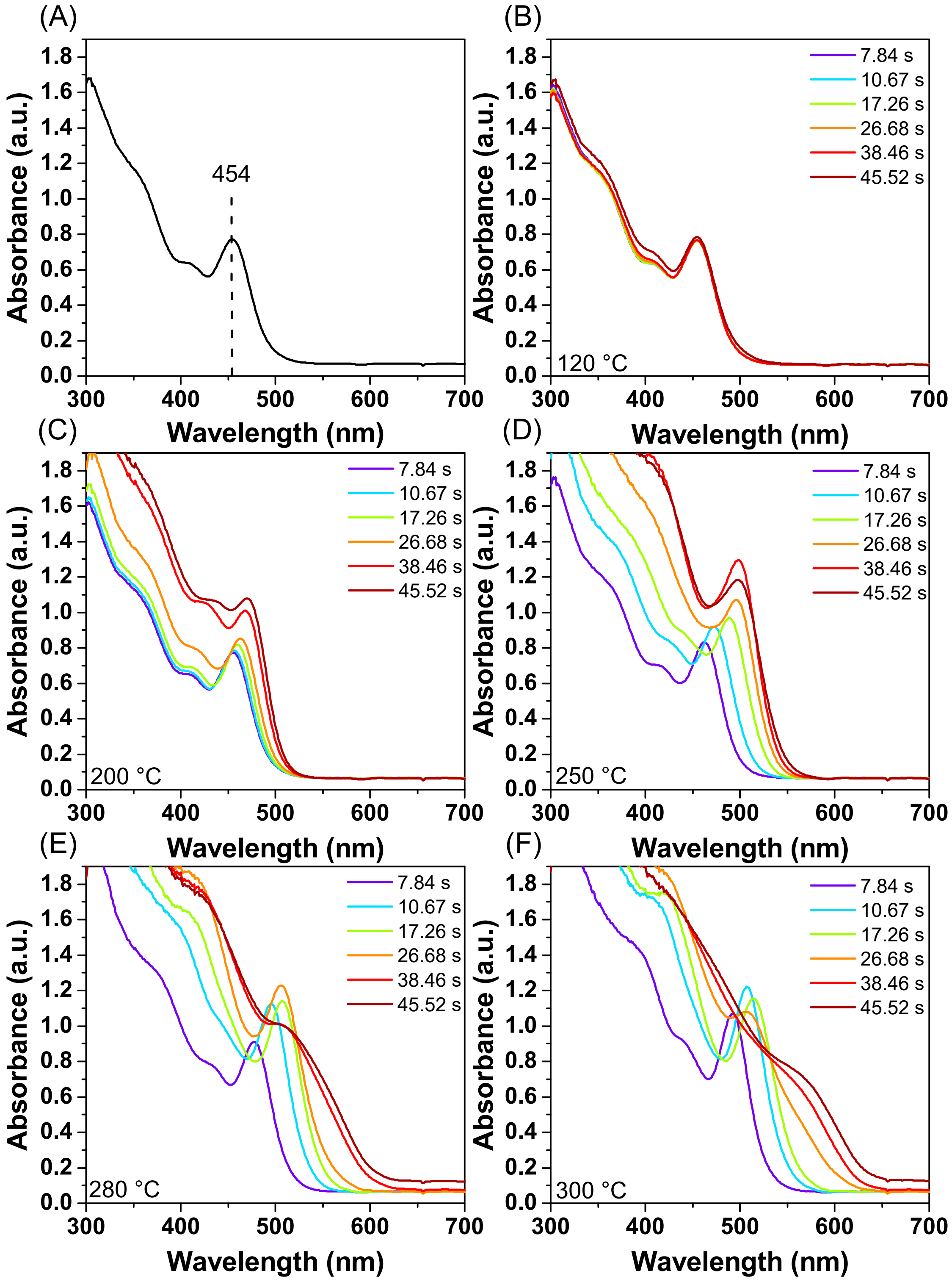

Figure 6.6.: UV/Vis absorption spectra of CdSe NC solution during growth experiment: (A) absorption spectrum of the solution before the reaction; (B)-(F) evolution of absorption spectra with reaction time for different growth temperatures.

spectra was observed with increasing residence time. An increase of the growth temperature to 200 °C initiated the reaction, indicated by an increase in OD together with a shift of the absorption peak center to longer wavelength. This corresponds to the continuous growth of the NCs through incorporation of free monomer.

Increasing the growth temperature further to 250 °C resulted in a significantly increased growth rate, as shown by the longer wavelength of the peak absorbance for all residence times, compared to the spectra obtained at 200 °C. After 26.68 s of growth the particles seemed to have reached a maximum size, as the absorption peak did not shift in wavelength with increasing residence time. With further progress of the reaction, the peak intensity increased after 38.46 s and decreased again, accompanied by a very slight shift to longer wavelength and a slight broadening of the absorption feature after 45.52 s of reaction time.

A further 30 °C increase in growth temperature to 280 °C shed some light on the cause of the apparent maximum size observed during growth at 250 °C. At this temperature the same maximum size was reached after only 17.26 s. A similar subsequent increase in peak OD as before was observed after 26.68 s. At higher residence times the peak OD dropped significantly, accompanied by a significant broadening of the absorption peak with reaction time. It can be concluded, that the maximum size, observed during this experiment, is a result of the depletion of free monomer in the CdSe solution. As the growth mechanism shifts to Ostwald ripening, the reaction rate is much slower, as small particles have to dissolve, before larger ones can grow. The consequence is a defocussing of the size distribution, as is evident from the present spectra. In this case, the population of particles that has reached the maximum size under focussing growth decreases through dissolution with increasing reaction time, while the particles on the larger end of the size distribution grow by incorporating the liberated monomer. This is indicated by the shift of the absorption onset to longer wavelength.

At a growth temperature of 300 °C the dissolution of the small particles occurs sufficiently quickly, so that further growth of the NCs is observed in the investigated time frame. In this case, a complete depletion of the final product of focussing growth can be observed after 38.46 s of residence time. Subsequently, a very broad absorption peak is observed at much longer wavelength, as the large particles continue to grow under dissolution of the smaller ones. At growth temperatures of 320 °C and 350 °C (spectra not depicted here) growth via Ostwald ripening is observed even earlier, while even larger particle sizes are reached after 45.52 s of growth.

A slow onset of continous growth was observed at a growth temperature of 200 °C, followed by faster growth in the focussing regime at 250 °C. This is clearly consistent with the previous experiments, where continuous growth was generally observed in a similar temperature range, while sequential growth of smaller clusters could be observed at lower temperatures.

It is possible, that the present NC solution contained smaller species than the NCs absorbing at 454 nm, suggested by the strong intensity increase of the excitonic absorption peak between 26.68 s and 38.46 s at 250 °C, while the peak position is nearly identical. This could be explained by the more rapid growth of smaller species under focussing conditions, while larger ones grow much more slowly, while the overall growth rate has decreased due to the waning monomer concentration.

The subsequent onset of Ostwald ripening is slow at temperatures of 250 °C and also 280 °C, allowing the observation of the first signs of ripening growth after 38.46 s and later. Subsequently it is a lot faster at 300 °C. These observations are also consistent with the previous experiments, where first signs of ripening growth were observed at similarly elevated temperature (compare section 5.2). Only in the pure ripening growth experiment discussed in section 6.1.2, fast ripening growth was observed at lower temperature. This is unsurprising though, due to the absence of free monomer in that experiment, making Ostwald ripening the dominant growth mechanism.

The growth process observed in this experiment followed traditional NC growth kinetics. The size evolution of the NCs occurred continuously, without any signs of quantized or sequential growth. In this regard, it differs significantly, from the growth behavior observed in many different experiments. Nevertheless, it can be assumed, that the NCs used in this experiment have also grown via magic-sized intermediates. The CdSe NC solution used here, has been prepared at nucleation and growth temperatures of 280 °C in a 10 cm growth oven using a Cd precursor solution with a reduced Cd concentration (0.06 M instead of 0.07 M). As this reduced concentration certainly decreases the nucleation rate in the mixing chamber, it stands to reason, that under these conditions, a nucleation temperature of 280 °C falls under the low nucleation temperature regime discussed in section 5.2.1. That means, that the nuclei concentration and subsequent cluster concentration was so low, that it had already been depleted after the 5 s of growth at 280 °C.

Furthermore, the fact that the onset of continuous growth, as well as the continuous growth behavior of the NCs observed in this experiment, is consistent with previous experiments, where MSC intermediates were observed, supports the previously-made assumption, that the CdSe NCs are always formed via magic-sized intermediates.

6.3. Conclusion of Cluster Growth Experiments

In the present line of experiments, the sequential growth behavior of the MSCs was to be investigated in more detail than in the previous nucleation and growth experiments. For this purpose, NC solutions containing MSC intermediates were prepared in nucleation and growth experiments and subsequently heated to given growth temperatures within a growth oven. This was done using crude solution from the CFD, as well as a solution previously purified by precipitation and redispersion. A comparison of the growth behavior of the clusters in these two solution allowed the comparison of growth behavior under focussing, as well as ripening conditions.

Under focussing conditions, the sequential growth of the different cluster species from one size to another, which was observed in the nucleation and growth experiments could be reproduced. In addition, another species of MSC, smaller than the first previously observed species of $CdSe_{403}$ could be identified. While the latter was not distinctly observed, hints of its presence in the shape of increased OD in the respective spectral region were detected. Following the sequential growth process, the formation of regular NC from the largest cluster species and subsequent continuous growth could be observed. The sequential growth process followed the order of $CdSe_{380} \rightarrow CdSe_{403} \rightarrow CdSe_{437} \rightarrow$ continuously growing NCs. The continuous growth based on the largest cluster species occurred simultaneous with the one of the regular NCs already present in the cluster solution before the experiment.

At the same time, a temperature dependance of the individual steps of the sequential growth process could be observed, with later steps occurring only very slowly at low temperature, while earlier steps occurred very rapidly at high growth temperatures. This effect is due to the increasing stability of the clusters with size, as the chemical potential of a smaller particle is higher than that of a larger particle due to its larger surface-to-volume ratio. Evidently, this is only relevant under pure focussing conditions, as a large excess of free monomer is available. With decreasing monomer concentration, the reaction rate of the subsequent steps is reduced by the monomer consumption of the previous steps, as discussed in section 5.2.1.

Under pure ripening condition, i.e. in the growth experiment conducted with the purified cluster solution as a precursor, the onset of continuous growth was different from the one observed before. As the cluster solution contained both, $CdSe_{437}$ and a previously formed population of regular NCs, continuous growth of the regular NCs occurred under dissolution of the cluster species, as no free monomer was available. In this ripening growth reaction, the dissolution of the cluster species started some time before the onset of the growth of the larger species, as shown by the time-resolved experiment. This delay served the accumulation of the monomer liberated from dissolving clusters until the concentration was sufficient for the growth of the larger NCs.

In a final experiment, the growth of regular nanocrystals in the presence of excess monomer was studied using the same, time-resolved experimental procedure. In this experiment, traditional continuous size evolution with time and temperature was observed, together with the shift from focussing growth to ripening growth after the excess monomer had been depleted by the growing NCs. The growth behavior of these regular NCs was consistent with that observed in other experiments, where magic-sized intermediates were present. This further supported the hypothesis, that all CdSe NCs synthesized within this project have grown via magic-sized intermediates.

7. Summary

At the outset of the project stood the previous reports of individual species of MSCs being formed as intermediates in NC synthesis,[56,58] and the report of sequential growth at low temperatures, followed by continuous growth of regular NCs based on these MSCs.[57,60] Based on the sequential growth mechanism it appeared likely, that the clusters formed as intermediates during high temperature colloidal NC synthesis formed via a similar mechanism. This prospect appeared as a sensible area of study, as it had not been previously reported.

In order to test the hypothesis, that colloidal semiconductor NCs prepared via high temperature hot-injection-like synthesis formed via sequentially growing MSC intermediates, a CFD coupling NC synthesis capabilities with online UV/Vis absorption spectroscopy for product characterization, was developed and set up. The modular setup, comprising mixing chamber and variable length growth ovens, together with variable flow rates allowed time resolutions between 0.5 s and 1 min.

After some testing, a suitable precursor system for the synthesis of CdSe NCs, which were to be studied as a model system, was found in the well-established precursor system developed by T. Jochum in his PhD thesis.[125] Serendipitously, using this precursor system at reaction temperatures suitable for the CFD yielded reaction rates which moved the relevant stages of NC formation directly into the observable time window.

After additional development work, a flow cell and heatable sample holder, compatible with synchrotron X-ray scattering experiments, were constructed. The benefit of these designs is evident from their successful use in three synchrotron beamtimes over the course of this work. In one of the beamtimes, *in situ* measurements in the heated sample cell were conducted successfully, while in the others *ex situ* measurements were conducted.

During nucleation and growth experiments conducted in the CFD, substantial evidence for the previously postulated sequential growth mechanism was observed. In a variation of nucleation and growth temperature, as well as residence time, magic-sized intermediates, of which the moiety $CdSe_{437}$ was observed most prominently, were detected. Under the investigated reaction conditions, a reaction pathway starting at the formation of the nuclei in the mixing chamber, followed by subsequent sequential growth of different-size moieties of MSCs and ending in the formation and subsequent continuous growth of regular NCs, seemed likely.

Based on the nucleation temperature and consequentially number of nuclei formed in the mixing chamber, a variation of the reaction rate of the individual steps of this reaction pathway could be observed. In consequence, the shift from focussing growth into ripening growth, after depletion of the monomer concentration, could be controlled by the concentration of the growing NCs. Based on these observations, suitable reaction conditions for the preparation of cluster solutions, i.e. CdSe NC solutions containing large amounts of MSC intermediates, could be identified.

Size-selective precipitation and subsequent optical characterization of the cluster solutions helped to identify some of the MSC moieties, formed as intermediates during NC formation. With reasonable certainty, species absorbing at around 350 nm and 385 nm were identified, alongside the previously assigned species of MSCs, $CdSe_{403}$ and $CdSe_{437}$.

Further characterization of this sequential growth process was done in specific cluster growth experiments, in which previously prepared cluster solutions were heated to defined growth temperatures. In these experiments, the growth behavior via magic-size intermediates, which was observed in the nucleation and growth experiments, could be confirmed. The more defined experimental conditions and the more comprehensively time-resolved layout of the experiment allowed a preliminary identification of the reaction pathway $CdSe_{380} \rightarrow CdSe_{403} \rightarrow CdSe_{437} \rightarrow$ NCs. In addition, a temperature dependance of the individual steps of this reaction pathway could be observed, which was correlated to the difference in chemical potential of the MSCs as a function of their size.

A cluster growth experiment performed in the absence of excess monomer, using a previously purified cluster solution showed the direct conversion of $CdSe_{437}$ into regular NCs via Ostwald ripening. In this experiment, a distinction between continuous growth of regular NCs from the largest cluster species under focussing and ripening conditions could be observed. Based on this, the cluster growth experiments corroborated the previously postulated reaction pathway.

In conclusion, the initial hypothesis, that NC formation at high temperatures can occur via a sequential growth pathway, starting at nucleation, finishing at continuously growing NCs and exhibiting a series of different-size MSCs as intermediates, could be substantiated with this work. To the author's knowledge, the application of a sophisticated time-resolved experimental procedure for the elucidation of the sequential growth process has not been reported before. Using the data collected within this work, expanded by only a few additional experiments, a complete kinetic analysis of this reaction pathway is possible.

In addition, the setup developed over the course of this project represents a superb toolbox for the time-resolved study of not only nucleation and growth of other NC systems, but also for other dynamic processes at the nanoscale, like cation exchange. This was already shown in preliminary experiments, using the CFD in conjunction with its X-ray flow cell to study the evolution of the cation exchange of ZnSe to CdSe using synchrotron extended X-ray absorption fine structure (EXAFS) at beamline P65 at DESY. Evidently, the establishment of the CFD setup facilitates the access to time-resolved analysis of dynamic processes in NC systems considerably.

8. Experimental Methods

8.1. The Continuous-Flow Device

Clearly, the most central experimental method applied in this work was the synthesis of NCs using the CFD. The standard procedure for which, together with the setup, are explained in this section.

8.1.1. Setup

Before discussing the NC synthesis in the CFD it is necessary to explain its setup, which was developed in collaboration with Jan Niehaus (CAN GmbH). It can basically be divided in three stages: precursor stage, reaction stage and characterization stage. The precursor stage comprises precursor storage, pumps, as well as sensors to measure flow parameters (flow rate, fluid density, pressure). The reaction stage contains all heated zones and covers the preheating, mixing and growth zone. In this stage the actual reaction is taking place and it ends with the quenching of the reaction. Finally in the characterization stage the product is characterized via online spectroscopy or X-ray scattering and collected for external characterization. In the following the components of the three stages are described in detail on the basis of figure 8.1 which shows a schematic drawing of the CFD's setup.

Within the precursor stage, the precursor solutions (1) stored in Sigma-Aldrich Sure/Stor flasks connected to a constant nitrogen supply (Schlenk line) are pumped via two HNP mzr-6355 micro annular gear pumps (2), which are fitted with upstream inline filters (10 µm pore size) to protect them, into the flow system. The pumps are controlled via Bronkhorst Mini Cori-Flow digital flow controllers (F1, F2). These measure the mass flow downstream of the pumps and set the pump rate via an analogue signal (between 0 and 10 V) in order to achieve the flow rate set via the computer. In addition they also measure the density of the fluid in the system,

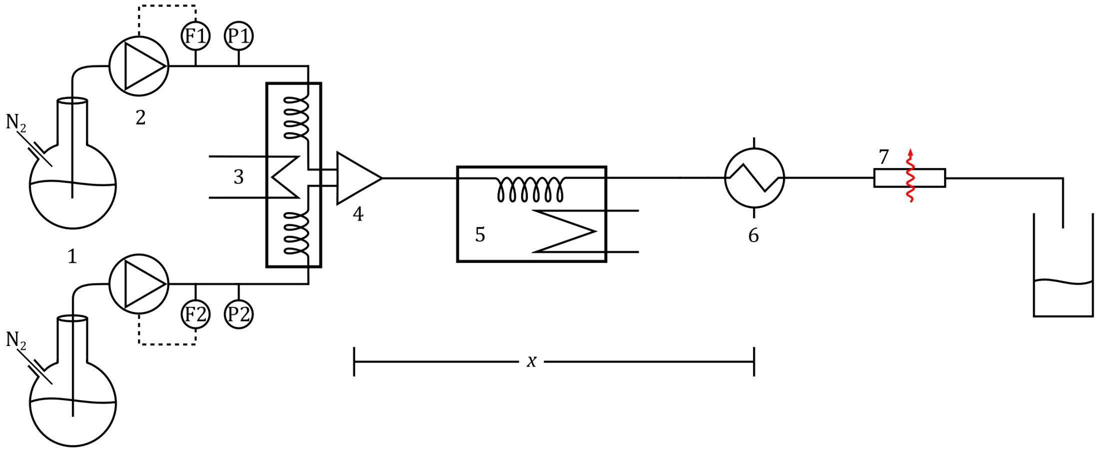

Figure 8.1.: Schematic drawing of the standard setup of the CFD.

which can also be read out via the computer.

The flow controllers are connected to pressure sensors (P1, P2; cetoni Qmix P module with two measurement channels) which measure the pressure in both fluid streams separately and are read out by the computer. Up to the pressure sensors all flow connections are made with ⅛ in (OD) PEEK tubing, unions, nuts and ferrules (Upchurch Scientific). As an alternative to the continuous pumps, syringe pumps (cetoni neMESYS mid-pressure module) can be used.

The pressure sensors are connected to the reaction stage, which starts with the preheating ovens (3), which are an in-house design made by the machine shop in the Institute of Physical Chemistry (University of Hamburg). The ovens consist of titanium tubing (Ethen Rohre, 1.6 mm OD) which is coiled around an aluminium core and covered with an aluminium sleeve. The core possesses two holes, one for a heating cartridge (HS-Heizelemente, 125 W, 230 V) and one for a RTD (Unitherm, PT-100, two-wire configuration).

The preheating ovens connect to the mixing chamber (4; slit inderdigital micromixer (SIMHEX) made from titanium by micro4industries) where both fluid streams are combined. It comprises a bottom half – with a hole for a heating cartridge – and a top half which contains the entrance and exit bores for the flow connections, as well as a hole for an RTD. An interdigitated titanium mixing structure, enclosed by a graphite seal is sandwiched between the two halves.

A growth oven (5; identical design as the preheating ovens) is connected downstream of the mixing chamber, directly followed by a micro tube bundle heat exchanger (6; micro4industries). Within the heat exchanger the flow is split up into ten separate, narrower tubes and later recombined. Water, cooled to 18 °C, is pumped by a chiller (Julabo F25-MC) through the outer part of the heat exchanger, thus cooling down the fluid within the inner tubes. Due to the elevated temperature within the reaction zone (up to 380 °C) all connections are made using titanium unions, and ferrules and stainless steel nuts in 1⁄16 in dimension (Vici Valco fittings). All temperatures are controlled using a 16-zone PID controller (Elotech R2500) which is connected to the computer.

Following the heat exchanger begins the characterization stage (7), where the fluid enters an optical flow cell (Knauer A4096 and A4047) in which its UV/Vis absorbance is measured using the online absorption spectrometer (see section 8.4.1 for details). Additionally an X-ray flow cell (in-house design) can be connected, which allows the measurement of X-ray scattering patterns at synchrotron beamlines (see section 4.3 for details). The central piece of the X-ray flow cell was a Kapton tube of 1.638 mm inner diameter and 1.803 mm outer diameter, manufactured by IWG High Performance Conductors. Afterwards the fluid exits the flow system and can be collected for further characterization.

Residence times reported within this work always indicate the time spent by the reaction mixture within the actual reaction volume. For the sake of simplifying the residence time calculation the reaction volume is defined as the volume starting with the exit slit of the mixing chamber, where the two liquids first meet, and ending with the inlet distributor of the heat exchanger, whereafter the reaction is quenched by cooling. All non-heated tubing connections between components in the reaction stage, including union inner volumes are considered part of the reaction volume.

Most components are controlled using proprietary software provided by the manufacturer. The flow controllers are controlled using FlowPlot and FlowView communicating with the controllers via FlowDDE (all provided by Bronkhorst). The syringe pumps as well as the pressure sensors are controlled using QMix Elements (cetoni). The spectrometer is controlled via MultiSpec Pro (tec5). The remote control of the temperature controller is realized using a home-made LabView program, that allows setting and reading out the parameters of all heatable zones individually.

The setup described serves as the basis of all experiments done within this work. Nevertheless, several experiments rely on a different composition of components.

Especially the setup of the reaction stage varied significantly, based on the aim of the specific experiments. These variations are noted explicitly, however, within the respective sections.

8.1.2. Standard CFD Experiment

In a standard CFD experiment, the device was set up as described in the previous section. The pumps were always used in parallel, pumping at the same flow rates. If the Cd-precursor solution to be used in the experiment was turbid, it was placed on a hot plate set to 60 °C. Prior to the experiment, it was stirred until the turbidity had dissolved. During the pumping, the stirrer was deactivated in order not to interfere with the suction of the pump.

The flow system was initially flushed with Cyanex to check for leaks. For safe operation the flow rate was chosen so, that the pressure did not exceed 10 bar. Before commencing the experiment, the system had to be purged of the Cyanex and filled with precursor solution. Since the filter housings of the continuous pumps constituted the largest part (by an order of magnitude) of the dead volume of the device with approximately 30 mL of inner volume each, the system was flushed with both precursor solutions (connnected to an open nitrogen line) at 1 mL/ min each for at least 30 min (a single residence time of the pump filters). Once the Cyanex was replaced by precursor solution, a drop in pressure due to the precursor's lower viscosity could be detected. This flushing step was carried out whenever the precursor solution was changed.

A reference spectrum was taken with the online UV/Vis absorption spectrometer, before the reaction stage was heated. Subsequently the heated zones (preheating, mixing and growth) were heated to the desired temperatures. Typically the preheating zone would be heated to the same temperature as the mixing chamber in order to make sure, that the precursor solutions were at reaction temperature upon mixing. The growth temperature was typically selected lower than or equal to the mixing temperature (or nucleation temperature).

After the temperature in all heated zones had stabilized, it was necessary to wait for the liquid which was in the reaction stage to reach the optical flow cell, before UV/Vis absorption spectra were collected. Typically spectra were obtained after between one and two residence times of the intermediate volume. The same delay was applied after each variation of a reaction parameter (temperature, flow rate).

After finishing the experiment, the heated zones were allowed to cool down to room temperature. In order to avoid blockage of the flow system, the system was continued to be flushed with precursor solution until all zones had cooled below 200 °C. Below that temperature, the pump inlets were switched into Cyanex and the system was again flushed for at least one residence time of the pump filter housings.

All small components of the CFD (fittings, unions) were cleaned by 15 min sonication cycles in toluene and afterwards in EtOH. The titanium parts of the mixing chamber were additionally sonicated in water, HNO_3 (20 %), water, and EtOH in that order. If necessary, the sonication steps were repeated.

8.2. Precursor Synthesis

This section details the precursor synthesis protocols used in this work. Both precursor syntheses were modified several times during the course of this work. Three different cadmium salts – CdO, $Cd(OAc)_2$, and $Cd(OAc)_2 \cdot 2\,H_2O$ – were used as a precursor, resulting in adaptations of the synthesis protocol. The composition of the Se precursor was also changed several times. Initially, pure TOP/Se was used as a Se precursor. Later on, the Se concentration and the TOP content were varied. Finally, together with the switch from CdO to $Cd(OAc)_2$ as a Cd source, the initial Se precursor synthesis was changed to a protocol based on a procedure developed by Tobias Jochum (CAN GmbH).[125]

All synthetic steps were carried out under Schlenk conditions using nitrogen as inert gas. Except for the CdO precursors, the Cd precursors were always prepared in a 2 L three-neck flask, fitted with a thermocouple and a septum. The flask was connected to the Schlenk line via a separate cold trap and an additional connection for nitrogen. All precursor chemicals, except CdO and ODPA, were stored in a glovebox under nitrogen atmosphere.

Cadmium Oxide Precursor

In the beginning of this project, a Cd precursor solution based on CdO was used. Typically, 1.0 g (7.8 mmol) of CdO (99.998 %, Alfa Aesar) was combined with 5.2 g

(16 mmol) of ODPA (>99 %, PCI) and 240 mL of Cyanex. This turbid brownish mixture was stirred at room temperature under vacuum until no more bubbles formed. It was then heated to 180 °C and stirred at that temperature for at least 4 h. Subsequently, it was set under nitrogen and heated to 330 °C. It was kept at that temperature until all turbidity had dissolved and it had become almost colorless. The solution was then left to cool down to 180 °C, where it was set under vacuum and kept stirring for at least 2 h. The Cd concentration of the oxide precursor was 32.4 $\mathrm{mmol\,L^{-1}}$.

Cadmium Acetate Precursor (anhydrous)

The cadmium-precursor synthesis using $Cd(OAc)_2$ was based on a protocol developed by Tobias Jochum (CAN GmbH).[125] In a typical synthesis, 46 g (0.14 mol) of ODPA were combined with 666 mL of Cyanex and stirred under oil-pump vacuum for at least 3 h. In the glovebox, a separate 1 L Schlenk flask, fitted with a septum, was filled with 17.633 g (76.499 mmol) of $Cd(OAc)_2$ (anhydrous, 99.999 %, ChemPUR) and 450 mL of TOP (97 %, abcr). Outside of the glovebox, it was attached to a Schlenk line and evacuated under oil-pump vacuum. The mixture inside was stirred under vacuum for at least 1.5 h while the temperature (measured inside the heating mantle) was kept at 80 °C.

After completion of the initial degassing step, the ODPA solution was heated under nitrogen to 110 °C, upon reaching which the $Cd(OAc)_2$ solution was transferred into the 2 L flask using a transfer needle. This resulted in strong bubbling of the solution which also turned opaque during the process. Afterwards, the reaction mixture was stirred under vacuum at 90 °C for at least 8 h during which the flask was flushed at least three times with nitrogen. The reaction mixture was then set under nitrogen and left to cool down to room temperature over night.

Subsequently, the temperature was increased to 90 °C again and the mixture was stirred under vacuum for another hour. It was then set under nitrogen again and heated to 210 °C for the first complexation step. At around 200 °C, the turbidity in the reaction mixture typically dissolved and it became a clear solution. The flask was agitated carefully to remove any solid that had collected on the sides of the flask while it was filled. The temperature was held at 210 °C for 1 h. The solution was left to cool down to 140 °C and set under vacuum upon reaching the temperature.

It was stirred at this temperature for 3 h during which the flask was flushed three times with nitrogen. The complexation and vacuum conditioning steps were then repeated once, before the solution was set under nitrogen and left to cool down over night.

The finished precursor solution was then heated to 40 °C to facilitate the subsequent transfer into a 2 L Sigma-Aldrich Sure/Stor flask using a transfer needle with attached inline filter. It was then stored under nitrogen. The anhydrous acetate precursor had a Cd concentration of 68.6 mmol L^{-1}.

Cadmium Acetate Dihydrate Precursor

Due to unavailability of anhydrous $Cd(OAc)_2$ during the preparation of the beamtime at ESRF, the Cd-precursor synthesis was adapted to use $Cd(OAc)_2 \cdot 2\,H_2O$ as Cd source. The preparation of the precursor remained largely the same as with the anhydrous $Cd(OAc)_2$ with some minor changes. During the dissolution of ODPA in Cyanex, the temperature was set to 40 °C, as it was observed that the temperature tended to drop below room temperature during this step.

Due to the added water of hydration, 20.390 g (76.502 mmol) of $Cd(OAc)_2 \cdot 2\,H_2O$ (98 %, ChemPUR) were used to prepare the initial Cd solution. It was stirred under oil-pump vacuum for at least 5 h at 100 °C (in the heating mantle). In this step it was crucial, not to dissolve the $Cd(OAc)_2 \cdot 2\,H_2O$ before the mixture was set under vacuum, as otherwise the water would not be extracted as easily. The remainder of the synthesis protocol was analogous to the Cd precursor with anhydrous $Cd(OAc)_2$, except for the temperature used in the final vacuum conditioning steps, following the complexation steps, which was 160 °C instead of 140 °C. The Cd concentration of this precursor type is the same as for the anhydrous acetate precursor. Approximatingly, it is referred to in this work as dihydrate precursor 0.07 mol L^{-1}.

A variation of this precursor type with reduced Cd content was prepared, using only 17.633 g (66.158 mmol) of $Cd(OAc)_2 \cdot 2\,H_2O$. This resulted in a concentration of 59.3 mmol L^{-1}. Analogously to its higher concentration variety, this precursor is referred to as dihydrate precursor 0.06 mol L^{-1}.

Storage of both concentrations of dihydrate precursor caused the precipitation of a colorless flocculent solid, which could be redissolved by stirring at a temperature of 50 °C.

Selenium Precursor

In the beginning of this work, the Se precursor was pure TOP/Se. It was prepared by dissolving 1.26 g (15.9 mmol) of Se shot (>99.999 %, Sigma-Aldrich or 99.999 %, ChemPUR) under stirring in 250 mL of TOP in a nitrogen-filled glovebox. The precursor was stored in a 500 mL Sigma-Aldrich Sure/Stor flask under nitrogen. The resulting Se concentration was 63.8 $\mathrm{mmol\,L^{-1}}$. It was varied by using 6.00 g (76.0 mmol) of Se shot, resulting in a Se concentration of 304 $\mathrm{mmol\,L^{-1}}$.

In order to investigate the effect of TOP on the reaction rate, another Se precursor was prepared, in which a large part of the TOP had been replaced with Cyanex. For this approach 1.26 g (15.9 mmol) of Se shot were dissolved under stirring in 20 mL of TOP in a nitrogen-filled glovebox. Outside the glovebox 230 mL of Cyanex were degassed in a 500 mL Sigma-Aldrich Sure/Stor flask under oil-pump vacuum until no more bubbles formed. It was flushed with nitrogen three times during this. The Cyanex was finally set under nitrogen and the TOP/Se was added to it.

The final selenium-precursor synthesis was based on a protocol developed by Tobias Jochum (CAN GmbH).[125] In a nitrogen-filled glovebox 64.5 g (0.817 mol) of selenium shot were combined with 600 mL of ODE (90 %, Sigma-Aldrich) and 600 mL of TOP in a 2 L Sigma-Aldrich Sure/Stor flask. The mixture was then stirred in oil-pump vacuum until the selenium was completely dissolved and no more bubbles appeared. The finished Se precursor was then stored under nitrogen. Its concentration was 681 $\mathrm{mmol\,L^{-1}}$. This type of Se precursor was used for all experiments described in chapters 5 and 6.

8.3. The Growth of Magic-Sized CdSe Clusters

This section details the experimental parameters for the results shown in section 6. The experiments, those results are based on, are referred to as cluster growth experiments within this work. The precursor for this type of experiment is not a mixture of a separate Cd and Se precursor, which form CdSe NCs in situ, but rather a previously prepared solution containing magic-sized CdSe clusters which are then grown within a growth oven. These cluster solutions do not only contain nanoclusters, but often a mixture of clusters and fully formed NCs. These can then be differentiated by their differing growth mechanism during the growth experiment.

8.3.1. Preparation of CdSe Cluster Growth Solutions

In this section, the preparation of the CdSe starting solutions used in the various cluster growth experiments is described. Each growth solution is identified by a consecutive number. Cluster preparation experiments were conducted as standard CFD experiments, using a 10 cm growth oven, and a total flow rate of 2 mL/ min. Temperature in the preheating, mixing and growth stage were kept at the same level. The obtained CdSe nanocluster solution typically showed a clear yellow color. Over time (between hours and a few days), a colorless flocculent precipitate formed, which was attributed to organics within the unpurified cluster solution. Table 8.1 contains a list of all cluster preparation experiments performed during this work. For each experiment the identifying number, reaction temperature, Cd-precursor type and whether or not the Cd precursor was preheated before entering the flow system are given.

Table 8.1.: Experimental parameters of CdSe cluster preparation experiments.

No.	T / °C	**Cd Precursor Type**	**Cd Preheating**
1	280	$Cd(OAc)_2 \cdot 2\,H_2O$ (0.07 M)	Yes
2	280	$Cd(OAc)_2 \cdot 2\,H_2O$ (0.07 M)	Yes
3	290	$Cd(OAc)_2 \cdot 2\,H_2O$ (0.06 M)	Yes
4	280	$Cd(OAc)_2 \cdot 2\,H_2O$ (0.06 M)	Yes

8.3.2. Optical Characterization of Cluster Solution

A size-selective precipitation approach was used to separate a part of the cluster solution 1 in fractions containing differently-sized NCs. The initial sample was a clear yellow liquid, which contained a colorless flocculent precipitate. It was centrifuged for 5 min at 1000 × g to remove the precipitate. The resulting clear yellow supernatant was filtered using a syringe filter (PTFE, 0.2 µm) and will be referred to as the initial fraction (Fi). 10 mL of EtOH were added to Fi and it was centrifuged for 10 min at 10000 × g resulting in no precipitate. Another 5 mL of EtOH were added and it was centrifuged again at the same speed. The resulting precipitate contained the first fraction (F1) of the nanoclusters and was redispersed in 5 mL of toluene.

After adding another 5 mL of EtOH to the supernatant and centrifuging again (same parameters as before) the second fraction (F2) of nanoclusters was obtained in the precipitate (again redispersed in 5 mL of toluene). The third fraction (F3) of clusters was precipitated by adding 5 mL of MeOH and centrifuging using the same parameters as before. It was redispersed in 3 mL of toluene. The supernatant obtained after the third precipitation step was turbid and colorless. It was split in two fractions of 15 mL, to which 10 mL of MeOH each were added. The subsequent centrifugation step was carried out at 10 °C and yielded the fourth fraction (F4) of clusters, which was also redispersed in 3 mL of toluene. The final supernatant contained two colorless phases of which the lower was turbid. A sample of both phases was taken with a syringe. Upon dilution of the turbid phase with toluene the turbidity dissolved, yielding a clear and colorless solution. Using UV/Vis absorption spectroscopy it could be determined that this phase in fact contained the fifth fraction (F5) of clusters.

All fraction samples were investigated using the Cary 50 offline UV/Vis absorption spectrometer. The samples were diluted using toluene to achieve optical densities below 0.1. Subsequently PL and PLE spectra of fraction F1 were obtained using the FluoroMax 4 spectrometer.

8.3.3. Cluster Growth in the Presence of Excess Monomer

In the cluster growth experiment from unpurified solution, cluster solution 1 was pumped via one continuous pump at 1 mL/ min through a growth oven that was connected to a heat exchanger, the Kapton flow cell and the optical flow cell with a path length of 0.5 mm. Before the experiment, the flow system had been run with the same cluster solution for several hours, so no additional flushing was required. The oven was heated to a range of growth temperatures, at which online UV/Vis absorption spectra were acquired. After completion of the temperature set the system was left to cool down to room temperature at reduced flow rate. Subsequently the oven was exchanged and the experiment was repeated at a different time resolution. In this experiment 10 cm and 50 cm growth ovens were used, resulting in residence times of 7.84 s and 26.68 s respectively. Growth temperatures investigated were 50 °C, 180 °C, 200 °C, 220 °C, 240 °C, 260 °C, 280 °C, 300 °C, 320 °C and 340 °C.

8.3.4. Cluster Growth in the Absence of Excess Monomer

Solvent for Purified CdSe Clusters

In order to find the right solvent for the purified CdSe nanoclusters a batch growth experiment with solutions of CdSe nanoclusters in different solvents was conducted. In preparation of that the solvent from an as-prepared nanocluster solution had to be removed and replaced by the solvents of interest. Initially 10 mL of the as-prepared cluster solution 2 were centrifuged for 5 min at 1000 × g to remove the colorless flocculent precipitate it showed. The precipitate was discarded, while 30 mL of EtOH were added to the clear yellow supernatant. The resulting turbid suspension was centrifuged for 10 min at 10000 × g. Subsequently the colorless supernatant was discarded, while the yellow precipitate was redispersed in 5 mL of toluene. It was further purified by washing twice with 15 mL of EtOH and centrifuging at 10000 × g for 10 min. Afterwards the precipitate was redispersed in 6 mL of toluene and split in three fractions. The nanoclusters in each fraction were precipitated by adding 6 mL of EtOH to each and centrifuging for another 10 min at 10000 × g. The precipitates were then dispersed in different solvent: the first in 2.5 mL of ODE, the second in 5 mL of diphenylether (DPE), and the last in 2 mL of a solvent mix analogous to the original reaction mixture[1]. Of the three solvents, only the ODE and the solvent mix were able to redisperse the nanoclusters, whereas the DPE fraction was turbid, exhibiting a yellow flocculent precipitate. All fractions were characterized by UV/Vis absorption spectroscopy but only the ODE and solvent mix fractions were used for the subsequent growth experiment.

For the growth experiment 1.5 mL of the ODE as well as solvent mix fractions were diluted with 1.5 mL of the respective solvents in a 10 mL three-neck flask equipped with thermocouple, septum and condenser each. The dilution was necessary to ensure sufficient coverage of the thermocouples. The solutions were heated to 250 °C and the temperature was held for 5 min. During that time both solutions changed in color from yellow to orange. Afterwards both solutions were left to cool down to room temperature. While cooling down the ODE solution's color changed back to yellow, while the solvent mix solution remained orange. For the ODE solution the temperature cycle was repeated and it changed its color again to orange while hot and back to yellow while cooling down.

---

[1] The solvent mix contained 3.4 mL of Cyanex, 5.3 mL of TOP, and 3.0 mL of ODE.

Both solutions were characterized using UV/Vis absorption spectroscopy, while the solvent mix solution was also characterized using TEM. The TEM sample was prepared by washing 2.5 mL of the solution three times with EtOH (7.5 mL in the first step, 6 mL in the subsequent steps) and centrifuging at 10000 × g for 10 min. The final precipitate was redispersed in 1 mL of toluene.

Growth Experiment from Purified CdSe Clusters (Batch)

In order to verify the results from the previous experiment, another batch growth experiment was conducted. For this purpose 20 mL of the same nanocluster solution used in the previous experiment were purified by washing three times with EtOH (60 mL in the first step, 30 mL in subsequent steps) and centrifuging at 10000 × g for 10 min. The final precipitate was redispersed in 10 mL of the solvent mix (same composition as in the previous experiment).

In one 10 mL three-neck flask equipped with thermocouple, septum and condenser each, two times 3 mL of the washed cluster solution were heated to 250 °C. The solutions were kept at that temperature for 30 s in one case and 60 s in the other case, before cooling them down to room temperature with a water bath. Both solutions were characterized using UV/Vis absorption spectroscopy, as well as TEM. The TEM samples were prepared analogously to the previous experiment.

Growth Experiment from Purified CdSe Clusters (CFD)

In order to perform the growth experiment with the washed cluster solution in the CFD, 250 mL of CdSe nanocluster solution 3 were purified. The solution was initially centrifuged for 5 min at 1000 × g to remove the colorless precipitate. The supernatant was split in two fractions, to which 280 mL of EtOH were added. The resulting suspensions were centrifuged at 10000 × g for 10 min. Afterwards, the precipitated nanoclusters were redispersed in 60 mL of toluene per fraction. Two more times both nanocluster fractions were precipitated with 180 mL of EtOH and centrifuged for 10 min at 10000 × g. The final precipitates were redispersed in 125 mL of solvent mix (215 mL of Cyanex, 340 mL of TOP and 195 mL of ODE) and then combined again. The resulting nanocluster dispersion appeared as a clear, yellow solution, developing only a slight turbidity over four days of storage.

The purified CdSe nanocluster solution was then used in a CFD growth experiment. In this experiment, a continuous pump was connected directly to a growth oven, heat exchanger and optical flow cell. The cluster solution was pumped at 1 mL/ min through the oven while the temperature was varied and online UV/Vis absorption spectra were collected. Before the experiment, the previously cleaned pump filter was filled with the purified cluster solution, before flushing the whole flow system for 5 min. After completing one set of temperatures, the system was left to cool down at reduced flow rate, before the oven was exchanged to change the time resolution of the experiment. Four different oven lengths were used: 10 cm, 30 cm, 50 cm and 90 cm. This resulted in residence times of 7.84 s, 17.26 s, 26.68 s and 45.52 s respectively. The temperatures investigated were 50 °C, 150 °C, 200 °C, 220 °C, 250 °C, 280 °C, 300 °C and 320 °C. After the experiment, the flow system was flushed with Cyanex for 30 min.

8.3.5. Growth from CdSe Nanocrystal Solution

The unpurified CdSe solution 4 was used as a precursor and pumped at 1 mL/ min. The experiment was performed analogously to the one described in section 8.3.3. For each temperature and growth oven UV/Vis absorption spectra were collected. The growth oven lengths used in this experiment were: 10 cm, 16 cm, 30 cm, 50 cm, 75 cm and 90 cm with residence times of 7.84 s, 10.67 s, 17.26 s, 26.68 s, 38.46 s and 45.52 s respectively. The growth temperatures investigated were 80 °C, 120 °C, 200 °C, 250 °C, 280 °C, 300 °C, 320 °C and 350 °C.

8.4. Characterization Techniques

Samples in this work were characterized using a variety of analytical techniques. Whereas section 2.2 details the underlying theoretical principles of the various methods, this section focuses on the description of the practical measurement procedures. It contains information about the equipment used in the measurements, as well as the sample preparation.

8.4.1. UV/Vis Absorption Spectroscopy

The main method for characterization of NC samples used in this work was UV/Vis absorption spectroscopy. UV/Vis absorption spectra were taken by two different methods. For the characterization of NC growth during continuous-flow experiments, the online UV/Vis absorption spectrometer coupled to the CFD was used in conjunction with optical flow cells of different path length. In order to characterize preprepared NC samples, as well as the results of particle washing experiments, an offline tabletop spectrometer was used with static cuvettes as sample environment. Due to the differing nature of both experiments, sample preparation was fundamentally different.

Online Spectroscopy

The CFD is fitted with a MultiSpec Desktop online spectrometer manufactured by tec5, which is controlled via the software MultiSpec Pro from the same manufacturer. The spectrometer contains a 30 W Deuterium lamp as well as a 7 W halogen lamp, the combination of which allows for a usable wavelength range from 190 to 2500 nm. The device is equipped with a spectrometer cassette which contains a static monochromator, which disperses the light onto a diode array detector and possesses a spectral range of 190–1015 nm. This allows the acquisition of whole spectra with each detector readout, instead of scanning the monochromator wavelength as is common in most absorption spectrometers. The software allows to read out the detector once for a customizable integration time, or continuously. In continuous mode a single spectra is taken every time an adjustable cycle time passes. The device also contains a spectrometer cassette which allows absorption measurements in the NIR region of the lamp spectrum, which was not used in the present work though.

The absorption measurement takes place in a sample cell which is attached to the flow system of the CFD via 1⁄16 in HPLC connections. It possesses quartz windows and is connected to the spectrometer via optical fibers. The optical flow cells used in this work, were manufactured by Knauer and were used with two different optical path lengths: 0.5 mm and 3 mm.

All absorption measurements were done after an initial dark, as well as reference measurement which was subtracted from the acquired spectra as a background.

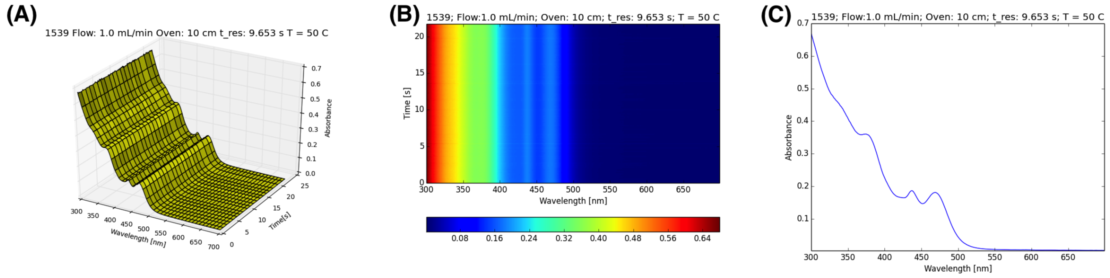

Figure 8.2.: Example of results from data treatment script: (A) 3D plot of spectra obtained in a cluster growth experiment, (B) 2D plot with color map of the same data, (C) averaged spectrum calculated from this data.

Unless otherwise noted, reference spectra were taken while pumping both precursor solutions at the flow rate used in the respective experiment without heating any of the reaction zones. For the cluster growth experiments, typically the reference spectra taken during the preparation of the respective cluster solution were used.

In order to improve signal-to-noise ratio, the integration time had to be adjusted, so that the intensity of the 100% transmitted light was maximized. Since this value changed over the course of this work due to modifications to the spectrometer, as well as replacement of the optical fibers, it is not always possible to compare the measured optical densities between different experiments. This also makes calculations of the concentration from the online spectroscopical data rather unreliable.

The online UV/Vis absorption data shown in this work was acquired by averaging a series of spectra acquired in continuous mode, typically between 60 and 300. This was done in order to reduce the influence of possible inhomogeneities (e.g. gas bubbles) flowing past the flow cell during the measurement.

Each spectrum acquired by the spectrometer software was saved in ASCII format within a previously specified folder on the measurement computer. Considering the amount of spectra taken during one measurement, this resulted in a few thousand files per measurement day. To overcome this issue a Python script was written that sorts the files according to date and time. The documented source code of the script is shown in section B.1 in the appendix. In order to facilitate the correlation of the measurement data to the experimental parameters, each single measurement is typically identified by the time and the date it was taken on.

For the purpose of making the raw data interpretable, another Python script was written which allows plotting of the data as well as data treatment (e.g. averaging). Its documented source code is shown in section B.2 in the appendix. Figure 8.2 shows exemplary output of the data treatment script. The script initially plots all spectra taken in one measurement (chosen by the user) in a 3D plot (figure 8.2 (A)), as well as a color map (B), as a function of acquisition time. This allows checking of the consistency of the data, as a variation of the absorption spectra with time becomes easily visible. In order to document such changes with time, it is also possible to plot OD at a selected wavelength against time. If the data is deemed consistent, as it is in this example, the script can finally average the single acquired spectra (section (C) in the figure) and generates an ASCII file containing the average spectrum. It also generates image files (.PNG format) of all plots. Should only part of a measurement contain consistent data, the script also allows selecting only a part of the acquired spectra for averaging. Further analysis of the data was then done in the software OriginPro 2016 by OriginLab.

Offline Spectroscopy

During the course of this work, some samples were also characterized offline using a Varian Cary 50 UV/Vis absorption spectrometer. This was done with the fractions obtained during the size-selective precipitation of NC solutions (section 8.3.2) as well as during the washing procedure in preparation of the growth experiment from a washed cluster solution. Since the Cary 50 is a single-beam spectrometer, a cuvette containing the pure solvent of the sample solutions was put into the sample compartment for an initial background measurement. The resulting 100% transmittance baseline was then subtracted from the subsequently measured spectra. These were typically measured between 300 and 700 nm.

Samples were prepared and their absorbance measured in quartz glass cuvettes with an optical path length of 1 cm. The sample solutions were diluted until their peak OD was lower than 0.1.

8.4.2. Photoluminescence Spectroscopy

PL as well as PLE spectroscopy were used in the characterization of the different species in section 5.3. The investigated sample was a fraction from the size-selective precipitation described in section 8.3.2. Both spectroscopy techniques were carried out using a Horiba Jobin Yvon FluoroMax 4 spectrometer. The FluoroMax 4 uses a 150 W xenon light source and excitation as well as emission monochromators in Czerny-Turner geometry. Both monochromators contain diffraction gratings with 1200 grooves/mm, with the excitation grating being blazed at 330 nm and the emission grating being blazed at 500 nm. A photomultiplier tube (PMT) serves as detector. Excitation and emission slit widths of 3 and 1 nm respectively were used for PL measurements. During PLE measurements, both slits were set to 1 nm width. Typically the samples' PL was measured after their absorbance and thus their preparation was analogous to the offline UV/Vis absorption measurements.

8.4.3. X-ray Powder Diffraction

X-ray powder diffractograms were obtained using a Philips X'Pert diffractometer with an X-ray tube emitting copper K_α radiation as an X-ray source. Samples were prepared by dropping sample solution onto a silicon wafer used as a sample holder and letting it dry. This was repeated several times to improve sample holder coverage. The obtained diffractograms were typically baseline corrected using the software PANalytical X'Pert HighScore. The same software was used to find suitable comparison diffractograms from the ICDD PDF-2 database, v2.3[131] to identify the present crystal phases. All XRD measurements were performed by Almut Barck (Institute of Physical Chemistry, University of Hamburg).

8.4.4. Transmission Electron Microscopy

Transmission electron microscopy was also used to obtain micrographs of some of the NCs prepared during this work. All images were taken on a Philips CM-300 UT microscope eqipped with a LaB_6 thermionic emitter using an acceleration voltage of 200 kV. This microscope is also equipped with an X-ray detector, making it possible to obtain EDX spectra. Samples were prepared by dropping 10 µL of the sample solution onto a copper grid (Plano, 400 meshes, $d = 3.05$ mm) covered with a thin amorphous carbon film and removing the solvent with a filter paper. All TEM and EDX measurements were carried out by Stefan Werner (Institute of Physical Chemistry, University of Hamburg).

8.4.5. Synchrotron X-ray Scattering Experiments

All synchrotron SAXS patterns shown in this work were obtained during a beamtime at beamline ID02 at ESRF. All measurements were conducted at a photon energy of 12.456 keV, with a sample-detector distance of 2.019 11 m. All patterns were recorded at an exposure time of 0.1 s in the KFC, connected to the CFD and heated via the prototype sample holder, under constant flow. The only exception are the patterns of the individual precursors, which were collected in quartz capillaries (Hilgenberg, wall thickness 0.01 mm, diameter 0.7 mm) with an exposure time of 1 s.

Bibliography

[1] R. Rossetti, L. Brus, *J. Phys. Chem.* **1982**, *86*, 4470–4472.

[2] H. Weller, U. Koch, M. Gutiérrez, A. Henglein, *Berichte der Bunsengesellschaft für Phys. Chemie* **1984**, *88*, 649–656.

[3] A. J. Nozik, F. Williams, M. T. Nenadovic, T. Rajh, O. I. Micic, *J. Phys. Chem.* **1985**, *89*, 397–399.

[4] A. P. Alivisatos, A. L. Harris, N. J. Levinos, M. L. Steigerwald, L. E. Brus, *J. Chem. Phys.* **1988**, *89*, 4001–4011.

[5] D. Heitmann, K. Kern, T. Demel, P. Grambow, K. Ploog, Y. H. Zhang, *Surf. Sci.* **1992**, *267*, 245–252.

[6] R. C. Ashoori, H. L. Stormer, J. S. Weiner, L. N. Pfeiffer, K. W. Baldwin, K. W. West, *Phys. Rev. Lett.* **1993**, *71*, 613–616.

[7] K. Bourzac, *Nature* **2013**, *493*, 283.

[8] S. Coe-Sullivan, P. T. Kazlas, *Quantum Dot Light Enhancement Substrate and Lighting Device Including Same*, **2017**, US Patent 9680054 B2.

[9] A. L. Efros, A. L. Efros, *Sov. Phys. Semicond.* **1982**, *16*, 772–775.

[10] L. Brus, *J. Phys. Chem.* **1986**, *90*, 2555–2560.

[11] H. Weller, *Angew. Chem.* **1993**, *105*, 43–55.

[12] D. V. Talapin, J. Steckel, *MRS Bull.* **2013**, *38*, 685–691.

[13] S. N. Raja, D. Zherebetskyy, S. Wu, P. Ercius, A. Powers, A. C. K. Olson, D. X. Du, L. Lin, S. Govindjee, L.-W. Wang, T. Xu, A. P. Alivisatos, R. O. Ritchie, *Nano Lett.* **2016**, *16*, 5060–5067.

[14] Y. Zhang, D. J. Hellebusch, N. D. Bronstein, C. Ko, D. F. Ogletree, M. Salmeron, A. P. Alivisatos, *Nat. Commun.* **2016**, *7*, 11924.

[15] M. Lorenzon, V. Pinchetti, F. Bruni, W. K. Bae, F. Meinardi, V. I. Klimov, S. Brovelli, *Nano Lett.* **2017**, *17*, 1071–1081.

[16] J. Lauth, J. Marbach, A. Meyer, S. Dogan, C. Klinke, A. Kornowski, H. Weller, *Adv. Funct. Mater.* **2014**, *24*, 1081–1088.

[17] T. Bielewicz, S. Dogan, C. Klinke, *Small* **2015**, *11*, 826–833.

[18] S. Willing, H. Lehmann, M. Volkmann, C. Klinke, *Sci. Adv.* **2017**, *3*, e1603191.

[19] M. Wu, D. N. Congreve, M. W. B. Wilson, J. Jean, N. Geva, M. Welborn, T. Van Voorhis, V. Bulovic, M. G. Bawendi, M. A. Baldo, *Nat. Photonics* **2015**, *10*, 31–34.

[20] X. Gong, Z. Yang, G. Walters, R. Comin, Z. Ning, E. Beauregard, V. Adinolfi, O. Voznyy, E. H. Sargent, *Nat. Photonics* **2016**, *10*, 253–258.

[21] F. Fan, O. Voznyy, R. P. Sabatini, K. T. Bicanic, M. M. Adachi, J. R. McBride, K. R. Reid, Y.-S. Park, X. Li, A. Jain, R. Quintero-Bermudez, M. Saravanapavanantham, M. Liu, M. Korkusinski, P. Hawrylak, V. I. Klimov, S. J. Rosenthal, S. Hoogland, E. H. Sargent, *Nature* **2017**, *544*, 75–79.

[22] D. R. Pernik, M. Gutierrez, C. Thomas, V. R. Voggu, Y. Yu, J. van Embden, A. J. Topping, J. J. Jasieniak, D. A. V. Bout, R. Lewandowski, B. A. Korgel, *ACS Energy Lett.* **2016**, *1*, 1021–1027.

[23] R. W. Crisp, G. F. Pach, J. M. Kurley, R. M. France, M. O. Reese, S. U. Nanayakkara, B. A. MacLeod, D. V. Talapin, M. C. Beard, J. M. Luther, *Nano Lett.* **2017**, *17*, 1020–1027.

[24] V. R. Voggu, J. Sham, S. Pfeffer, J. Pate, L. Fillip, T. B. Harvey, R. M. Brown, B. A. Korgel, *ACS Energy Lett.* **2017**, *2*, 574–581.

[25] J. Ostermann, J.-P. Merkl, S. Flessau, C. Wolter, A. Kornowksi, C. Schmidtke, A. Pietsch, H. Kloust, A. Feld, H. Weller, *ACS Nano* **2013**, *7*, 9156–9167.

[26] J. Dimitrijevic, L. Krapf, C. Wolter, C. Schmidtke, J.-P. Merkl, T. Jochum, A. Kornowski, A. Schüth, A. Gebert, G. Hüttmann, T. Vossmeyer, H. Weller, *Nanoscale* **2014**, *6*, 10413–10422.

[27] F. Li, J. Lu, X. Kong, T. Hyeon, D. Ling, *Adv. Mater.* **2017**, *29*, 1605897.

[28] C. R. Kagan, E. Lifshitz, E. H. Sargent, D. V. Talapin, *Science* **2016**, *353*, 885.

[29] C. Burda, X. Chen, R. Narayanan, M. A. El-Sayed, *Chem. Rev.* **2005**, *105*, 1025–1102.

[30] X. Peng, *Nano Res.* **2009**, *2*, 425–447.

[31] M. V. Kovalenko, L. Manna, A. Cabot, Z. Hens, D. V. Talapin, C. R. Kagan, V. I. Klimov, A. L. Rogach, P. Reiss, D. J. Milliron, P. Guyot-Sionnnest, G. Konstantatos, W. J. Parak, T. Hyeon, B. A. Korgel, C. B. Murray, W. Heiss, *ACS Nano* **2015**, *9*, 1012–1057.

[32] D. V. Talapin, A. L. Rogach, M. Haase, H. Weller, *J. Phys. Chem. B* **2001**, *105*, 12278.

[33] H. C. Schwarzer, W. Peukert, *AIChE J.* **2004**, *50*, 3234–3247.

[34] J. Y. Rempel, M. G. Bawendi, K. F. Jensen, *J. Am. Chem. Soc.* **2009**, *131*, 4479–4489.

[35] J. Van Embden, J. E. Sader, M. Davidson, P. Mulvaney, *J. Phys. Chem. C* **2009**, *113*, 16342.

[36] J. S. Steckel, B. K. H. Yen, D. C. Oertel, M. G. Bawendi, *J. Am. Chem. Soc.* **2006**, *128*, 13032.

[37] H. Liu, J. S. Owen, A. P. Alivisatos, *J. Am. Chem. Soc.* **2007**, *129*, 305–312.

[38] J. S. Owen, E. M. Chan, H. Liu, A. P. Alivisatos, *J. Am. Chem. Soc.* **2010**, *132*, 18206–18213.

[39] E. V. Shevchenko, D. V. Talapin, H. Schnablegger, A. Kornowski, Ö. Festin, P. Svedlindh, M. Haase, H. Weller, *J. Am. Chem. Soc.* **2003**, *125*, 9090–9101.

[40] X. Peng, J. Wickham, A. P. Alivisatos, *J. Am. Chem. Soc.* **1998**, *120*, 5343.

[41] L. Qu, W. W. Yu, X. Peng, *Nano Lett.* **2004**, *4*, 465–469.

[42] R. Viswanatha, H. Amenitsch, D. D. Sarma, *J. Am. Chem. Soc.* **2007**, *129*, 4470–4475.

[43] M. Tiemann, Ö. Weiß, J. Hartikainen, F. Marlow, M. Lindén, *ChemPhysChem* **2005**, *6*, 2113–2119.

[44] B. Abécassis, F. Testard, O. Spalla, P. Barboux, *Nano Lett.* **2007**, *7*, 1723–1727.

[45] A. L. Brazeau, N. D. Jones, *J. Phys. Chem. C* **2009**, *113*, 20246–20251.

[46] X. Chen, J. H. Schröder, S. Hauschild, S. Rosenfeldt, M. Dulle, S. Förster, *Langmuir* **2015**, *31*, 11678–11691.

[47] J. Polte, R. Erler, A. F. Thünemann, S. Sokolov, T. T. Ahner, K. Rademann, F. Emmerling, R. Kraehnert, *ACS Nano* **2010**, *4*, 1076–1082.

[48] W. Schmidt, P. Bussian, M. Lindén, H. Amenitsch, P. Agren, M. Tiemann, F. Schüth, *J. Am. Chem. Soc.* **2010**, *132*, 6822–6826.

[49] J. Polte, R. Erler, A. F. Thünemann, F. Emmerling, R. Kraehnert, *Chem. Commun.* **2010**, *46*, 9209–9211.

[50] A. Schiener, A. Magerl, A. Krach, S. Seifert, H.-G. Steinrück, J. Zagorac, D. Zahn, R. Weihrich, *Nanoscale* **2015**, *7*, 11328–11333.

[51] J. Polte, T. T. Ahner, F. Delissen, S. Sokolov, F. Emmerling, A. F. Thünemann, R. Kraehnert, *J. Am. Chem. Soc.* **2010**, *132*, 1296–1301.

[52] B. Abécassis, C. Bouet, C. Garnero, D. Constantin, N. Lequeux, S. Ithurria, B. Dubertret, B. R. Pauw, D. Pontoni, *Nano Lett.* **2015**, *15*, 2620–2626.

[53] R. M. Maceiczyk, L. Bezinge, A. J. DeMello, *React. Chem. Eng.* **2016**, *1*, 261–271.

[54] P. Nørby, S. Johnsen, B. B. Iversen, *ACS Nano* **2014**, *8*, 4295–4303.

[55] I. Lignos, L. Protesescu, S. Stavrakis, L. Piveteau, M. J. Speirs, M. A. Loi, M. V. Kovalenko, A. J. DeMello, *Chem. Mater.* **2014**, *26*, 2975–2982.

[56] Z. A. Peng, X. Peng, *J. Am. Chem. Soc.* **2002**, *124*, 3343–3353.

[57] S. Dolai, P. Dutta, B. B. Muhoberac, C. D. Irving, R. Sardar, *Chem. Mater.* **2015**, *27*, 1057–1070.

[58] D. C. Gary, M. W. Terban, S. J. L. Billinge, B. M. Cossairt, *Chem. Mater.* **2015**, *27*, 1432–1441.

[59] V. N. Soloviev, A. Eichhöfer, D. Fenske, U. Banin, *J. Am. Chem. Soc.* **2000**, *122*, 2673–2674.

[60] S. Kudera, M. Zanella, C. Giannini, A. Rizzo, Y. Li, G. Gigli, R. Cingolani, G. Ciccarella, W. Spahl, W. J. Parak, L. Manna, *Adv. Mater.* **2007**, *19*, 548–552.

[61] M. Zanella, A. Z. Abbasi, A. K. Schaper, W. J. Parak, *J. Phys. Chem. C* **2010**, *114*, 6205–6215.

[62] C. Kittel, *Einführung in die Festkörperphysik*, Oldenbourg Verlag, München, 14th ed., **2006**.

[63] H. Ibach, H. Lüth, *Festkörperphysik*, Springer-Verlag, Berlin, 7th ed., **2009**.

[64] P. W. Atkins, J. de Paula, *Physikalische Chemie*, Wiley-VCH, Weinheim, 4th ed., **2006**.

[65] P. Y. Yu, M. Cardona, *Fundamentals of Semiconductors - Physics and Materials Properties*, Springer-Verlag, Berlin Heidelberg New York, 3rd ed., **2005**.

[66] H. Weller, *Angew. Chemie Int. Ed.* **1993**, *32*, 41–53.

[67] L. E. Brus, *J. Chem. Phys.* **1984**, *80*, 4403.

[68] H. Weller, *Adv. Mater.* **1993**, *5*, 88–95.

[69] A. I. Ekimov, F. Hache, M. C. Schanne-Klein, D. Ricard, C. Flytzanis, I. A. Kudryavtsev, T. V. Yazeva, A. V. Rodina, A. L. Efros, *J. Opt. Soc. Am. B* **1993**, *10*, 100–107.

[70] D. J. Norris, M. G. Bawendi, *Phys. Rev. B* **1996**, *53*, 16338–16346.

[71] W. W. Yu, L. Qu, W. Guo, X. Peng, *Chem. Mater.* **2003**, *15*, 2854–2860.

[72] J. Jasieniak, L. Smith, J. van Embden, P. Mulvaney, M. Califano, *J. Phys. Chem. C* **2009**, *113*, 19468–19474.

[73] A. P. Alivisatos, *J. Phys. Chem.* **1996**, *100*, 13226–13239.

[74] P. Kambhampati, *Acc. Chem. Res.* **2011**, *44*, 1–13.

[75] Z. Hens, I. Moreels, *J. Mater. Chem.* **2012**, *22*, 10406–10415.

[76] C. A. Leatherdale, W.-K. Woo, F. V. Mikulec, M. G. Bawendi, *J. Phys. Chem. B* **2002**, *106*, 7619–7622.

[77] A. D. Yoffe, *Adv. Phys.* **2001**, *50*, 1–208.

[78] I. N. Levine, *Quantum Chemistry*, Pearson Education, Upper Saddle River, 6th ed., **2009**.

[79] E. Cassette, T. Mirkovic, G. D. Scholes, *J. Phys. Chem. Lett.* **2013**, *4*, 2091–2093.

[80] P. Reiss, M. Protière, L. Li, *Small* **2009**, *5*, 154–168.

[81] W. Friedrich, P. Knipping, M. Laue, *Sitzungsberichte der Math. Klasse der Königlich Bayer. Akad. der Wissenschaften* **1912**, 303.

[82] W. Massa, *Kristallstrukturbestimmung*, Springer Fachmedien, Wiesbaden, 8th ed., **2015**.

[83] W. H. Bragg, W. L. Bragg, *Proc. R. Soc. A Math. Phys. Eng. Sci.* **1913**, *88*, 428–438.

[84] A. Le Bail, I. Madsen, L. M. D. Cranswick, J. K. Cockcroft, P. Norby, A. D. Zuev, A. Fitch, J. Rodriguez-Carvajal, C. Giacovazzo, R. B. Von Dreele, P. Scardi, N. C. Popa, R. Allmann, L. A. Solovyov, B. Hinrichsen, U. Schwarz, A. Altomare, A. Moliterni, R. Caliandro, R. Rizzi, N. V. Y. Scarlett, M. Jansen, *Powder Diffraction*, The Royal Society of Chemistry, **2008**.

[85] O. Glatter, K. C. Holmes, R. Kirste, G. Kostorz, O. Kratky, P. Laggner, H. Leopold, K. Müller, R. C. Oberthür, I. Pilz, G. Porod, H. Stuhrmann, C. G. Vonk, P. Zipper, *Small Angle X-ray Scattering*, Academic Press, London, **1982**.

[86] D. I. Svergun, M. H. J. Koch, *Reports Prog. Phys.* **2003**, *66*, 1735–1782.

[87] C. B. Murray, C. R. Kagan, M. G. Bawendi, *Annu. Rev. Mater. Sci.* **2000**, *30*, 545–610.

[88] M. Harada, N. Tamura, M. Takenaka, *J. Phys. Chem. C* **2011**, *115*, 14081–14092.

[89] H. Koerner, R. I. MacCuspie, K. Park, R. A. Vaia, *Chem. Mater.* **2012**, *24*, 981–995.

[90] J. Polte, X. Tuaev, M. Wuithschick, A. Fischer, A. F. Thuenemann, K. Rademann, R. Kraehnert, F. Emmerling, *ACS Nano* **2012**, *6*, 5791–5802.

[91] A. Schiener, T. Wlochowitz, S. Gerth, T. Unruh, A. Rempel, H. Amenitsch, A. Magerl, *Mater. Res. Soc. Symp. Proc. Vol. 1528*, **2013**, pp. 1–6.

[92] S. Yan, Z. Wu, H. Yu, Y. Gong, Y. Tan, R. Du, W. Chen, X. Xing, G. Mo, Z. Chen, Q. Cai, D. Sun, *J. Phys. Chem. C* **2014**, *118*, 11454–11463.

[93] D. B. Williams, C. B. Carter, *Transmission Electron Microscopy*, Springer Science+Business Media, New York, 2nd ed., **2009**.

[94] B. Fultz, J. Howe, *Transmission Electron Microscopy and Diffractometry of Materials*, Springer, Berlin, 4th ed., **2013**.

[95] Y. Wang, Y. Li, C. Rong, J. P. Liu, *Nanotechnology* **2007**, *18*, 465701.

[96] C. Strelow, S. Kietzmann, A. Schramm, R. Seher, J.-P. Penttinen, T. V. Hakkarainen, A. Mews, T. Kipp, *Appl. Phys. Lett.* **2012**, *101*, 113114.

[97] B. J. Stanbery, S. Kincal, S. Kim, C. H. Chang, S. P. Ahrenkiel, G. Lippold, H. Neumann, T. J. Anderson, O. D. Crisalle, *J. Appl. Phys.* **2002**, *91*, 3598–3604.

[98] A. Biswas, I. S. Bayer, A. S. Biris, T. Wang, E. Dervishi, F. Faupel, *Adv. Colloid Interface Sci.* **2012**, *170*, 2–27.

[99] C. B. Murray, D. J. Norris, M. G. Bawendi, *J. Am. Chem. Soc.* **1993**, *115*, 8706–8715.

[100] Y. Yin, A. P. Alivisatos, *Nature* **2005**, *437*, 664–670.

[101] C. D. M. Donegá, P. Liljeroth, D. Vanmaekelbergh, *Small* **2005**, *1*, 1152–1162.

[102] S. G. Kwon, T. Hyeon, *Small* **2011**, *7*, 2685–2702.

[103] P. L. Saldanha, V. Lesnyak, L. Manna, *Nano Today* **2017**, *12*, 46–63.

[104] V. K. LaMer, R. H. Dinegar, *J. Am. Chem. Soc.* **1950**, *72*, 4847–4854.

[105] T. Sugimoto, *Adv. Colloid Interface Sci.* **1987**, *28*, 65–108.

[106] J. Van Embden, A. S. R. Chesman, J. J. Jasieniak, *Chem. Mater.* **2015**, *27*, 2246–2285.

[107] A. Fojtik, H. Weller, U. Koch, A. Henglein, *Berichte der Bunsengesellschaft für Phys. Chemie* **1984**, *88*, 969–977.

[108] Q. Yu, C. Y. Liu, *J. Phys. Chem. C* **2009**, *113*, 12766–12771.

[109] Z. J. Jiang, D. F. Kelley, *ACS Nano* **2010**, *4*, 1561–1572.

[110] J. C. Newton, K. Ramasamy, M. Mandal, G. K. Joshi, A. Kumbhar, R. Sardar, *J. Phys. Chem. C* **2012**, *116*, 4380–4389.

[111] A. Kasuya, R. Sivamohan, Y. A. Barnakov, I. M. Dmitruk, T. Nirasawa, V. R. Romanyuk, V. Kumar, S. V. Mamykin, K. Tohji, B. Jeyadevan, K. Shinoda, T. Kudo, O. Terasaki, Z. Liu, R. V. Belosludov, V. Sundararajan, Y. Kawazoe, *Nat. Mater.* **2004**, *3*, 99–102.

[112] J. Ouyang, M. B. Zaman, F. J. Yan, D. Johnston, G. Li, X. Wu, D. Leek, C. I. Ratcliffe, J. A. Ripmeester, K. Yu, *J. Phys. Chem. C* **2008**, *112*, 13805–13811.

[113] K. Yu, M. Z. Hu, R. Wang, M. L. Piolet, M. Frotey, M. B. Zaman, X. Wu, D. M. Leek, Y. Tao, D. Wilkinson, C. Li, *J. Phys. Chem. C* **2010**, *114*, 3329–3339.

[114] A. D. Dukes, J. R. McBride, S. J. Rosenthal, *Chem. Mater.* **2010**, *22*, 6402–6408.

[115] B. M. Cossairt, J. S. Owen, *Chem. Mater.* **2011**, *23*, 3114–3119.

[116] J. Ning, U. Banin, *Chem. Commun.* **2017**, *53*, 2626–2629.

[117] S. M. Harrell, J. R. McBride, S. J. Rosenthal, *Chem. Mater.* **2013**, *25*, 1199–1210.

[118] K. Yu, *Adv. Mater.* **2012**, *24*, 1123–1132.

[119] R. Xie, Z. Li, X. Peng, *J. Am. Chem. Soc.* **2009**, *131*, 15457–15466.

[120] R. K. Capek, K. Lambert, D. Dorfs, P. F. Smet, D. Poelman, A. Eychmüller, Z. Hens, *Chem. Mater.* **2009**, *21*, 1743–1749.

[121] L. H. Qu, Z. A. Peng, X. G. Peng, *Nano Lett* **2001**, *1*, 333–337.

[122] J.-S. Niehaus, PhD thesis, Universität Hamburg, **2012**.

[123] D. Neß, PhD thesis, Universität Hamburg, **2013**.

[124] K. Poulsen, PhD thesis, Universität Hamburg, **2015**.

[125] T. Jochum, PhD thesis, Universität Hamburg, **2016**.

[126] M. Tiemann, F. Marlow, F. Brieler, M. Lindén, *J. Phys. Chem. B* **2006**, *110*, 23142–23147.

[127] M. Tiemann, F. Marlow, J. Hartikainen, O. Weiss, M. Linden, *J. Phys. Chem. C* **2008**, *112*, 1463–1467.

[128] B. Abécassis, F. Testard, Q. Kong, B. Francois, O. Spalla, *Langmuir* **2010**, *26*, 13847–54.

[129] DuPont, *DuPont™ Kapton® Summary of Properties*, **2017**.

[130] R. Jose, N. U. Zhanpeisov, H. Fukumura, Y. Baba, M. Ishikawa, *J. Am. Chem. Soc.* **2006**, *128*, 629–636.

[131] ICDD, *Powder Diffraction File-2*, **2008**.

[132] Institut für Arbeitsschutz der DGUV, *GESTIS substance database*, found at: http://gestis.itrust.de, last accessed: **2017/08/16**.

[133] Cytec Inc., *Cyanex 923 Safety Data Sheet*, **2015**.

A. Engineering Drawings

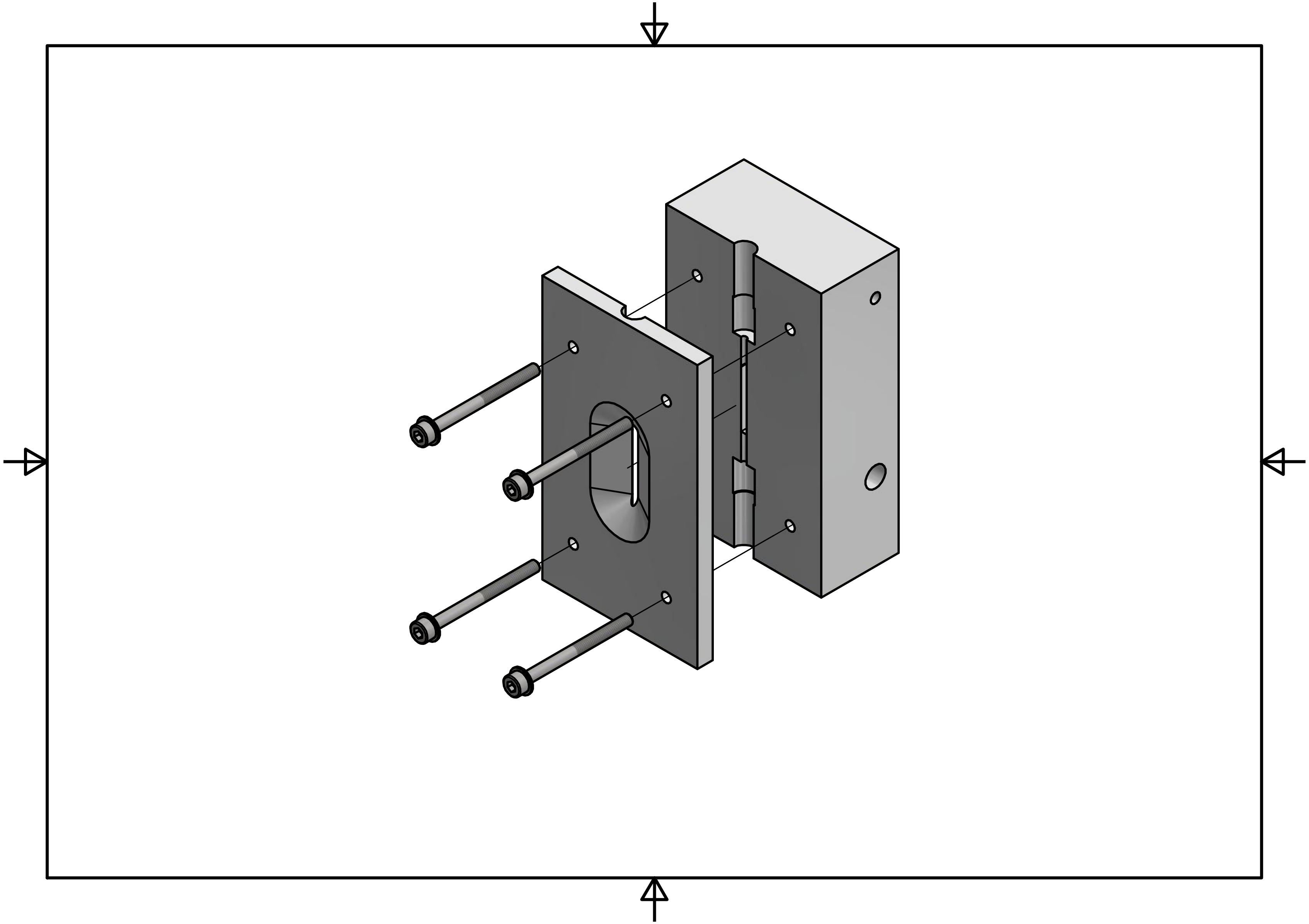

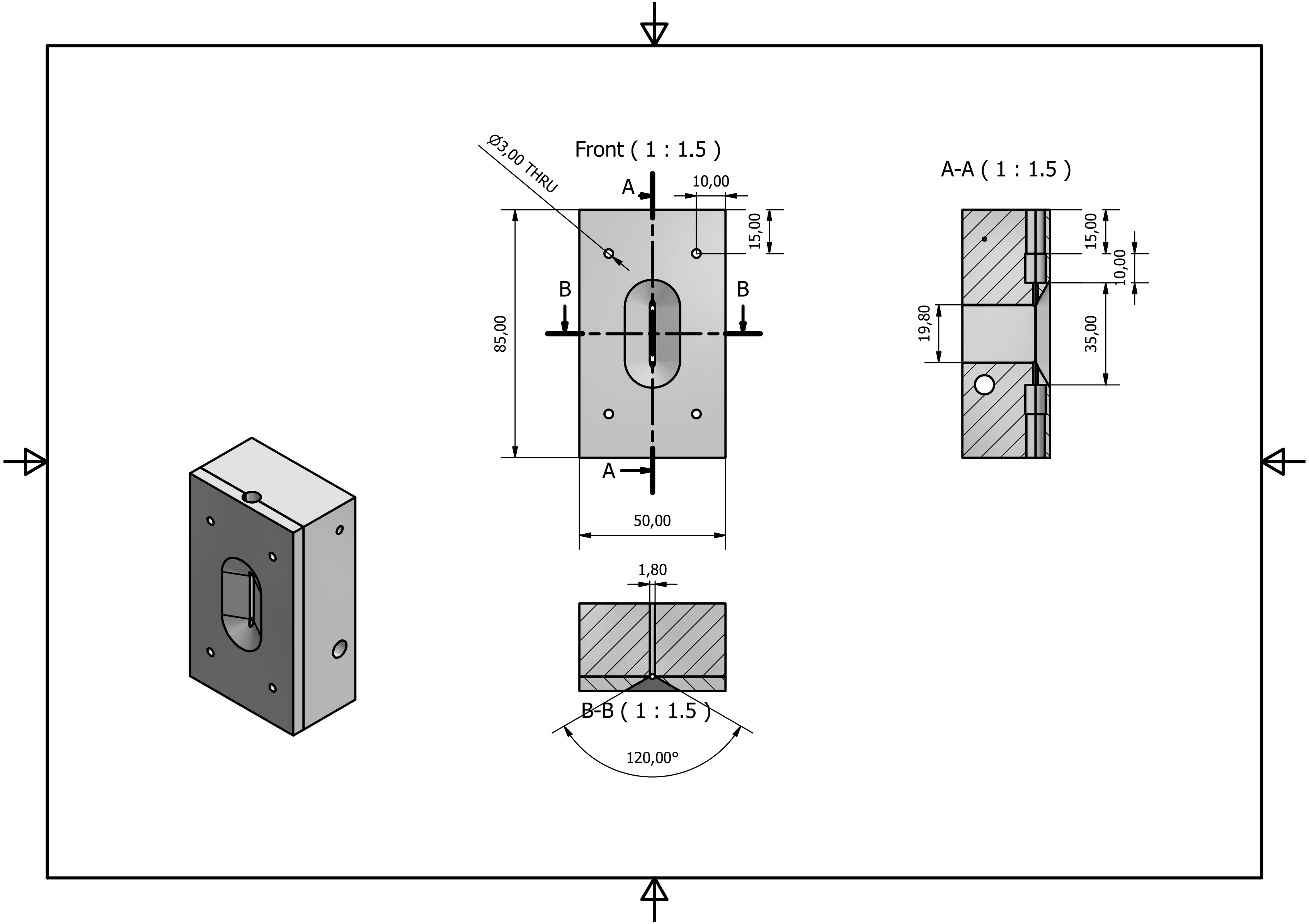
Front (1 : 1.5)
Ø3,00 THRU
A
A
B
B
10,00
15,00
85,00
50,00
A-A (1 : 1.5)
15,00
10,00
19,80
35,00
1,80
B-B (1 : 1.5)
120,00°

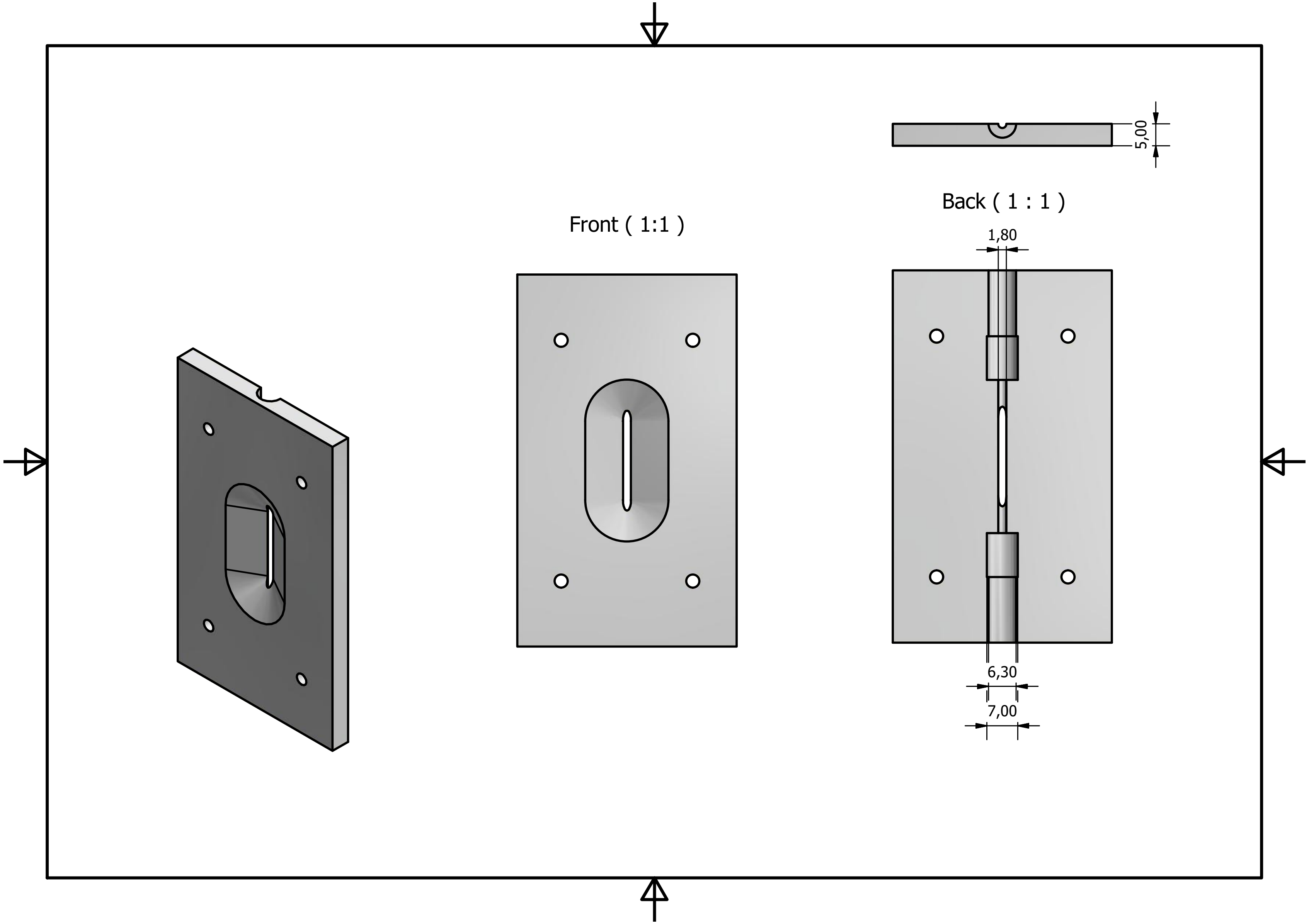
Front (1:1)
Back (1 : 1)
5,00
1,80
6,30
7,00

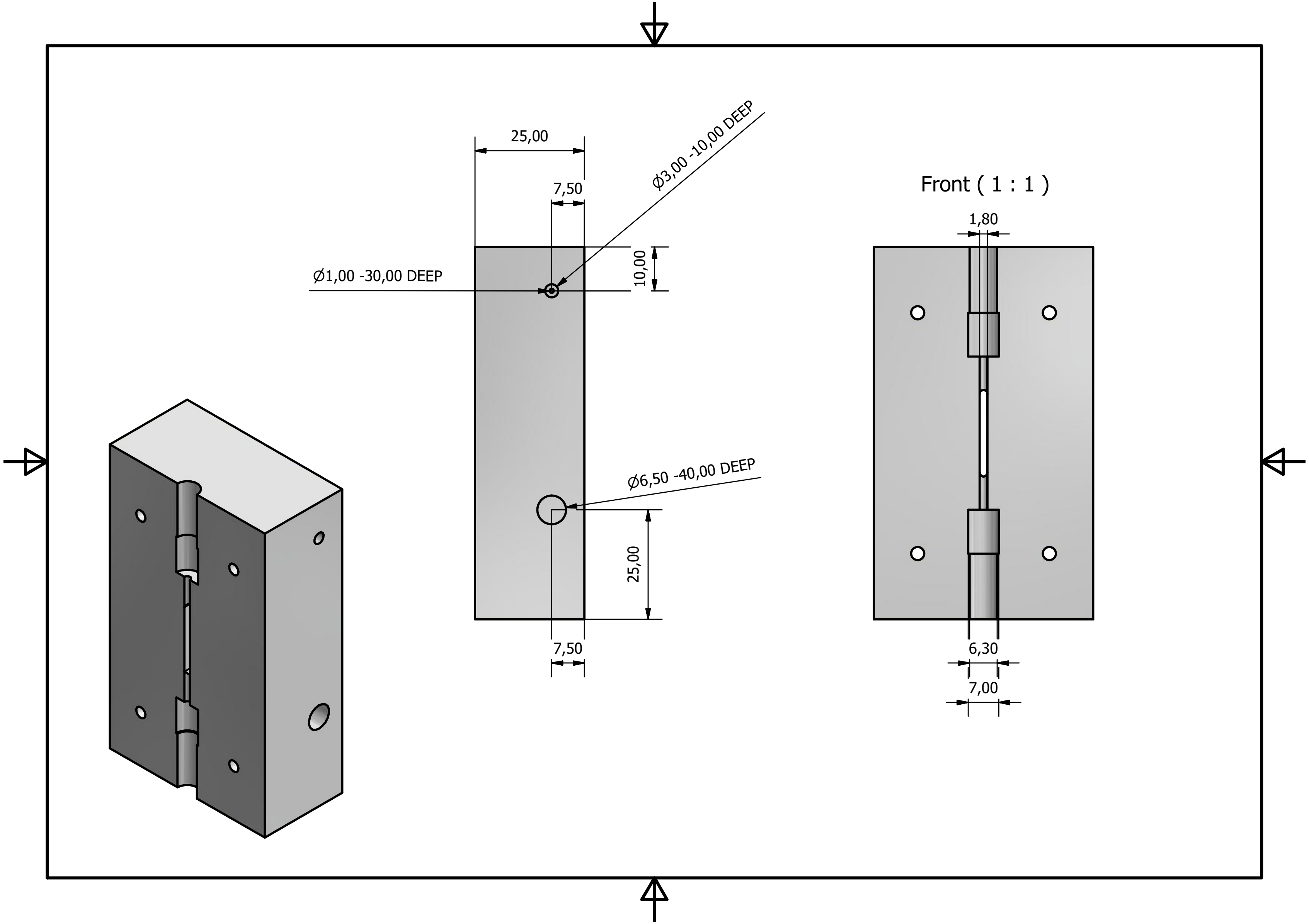
25,00
7,50
Ø3,00 -10,00 DEEP
Ø1,00 -30,00 DEEP
10,00
Ø6,50 -40,00 DEEP
25,00
7,50
Front (1 : 1)
1,80
6,30
7,00

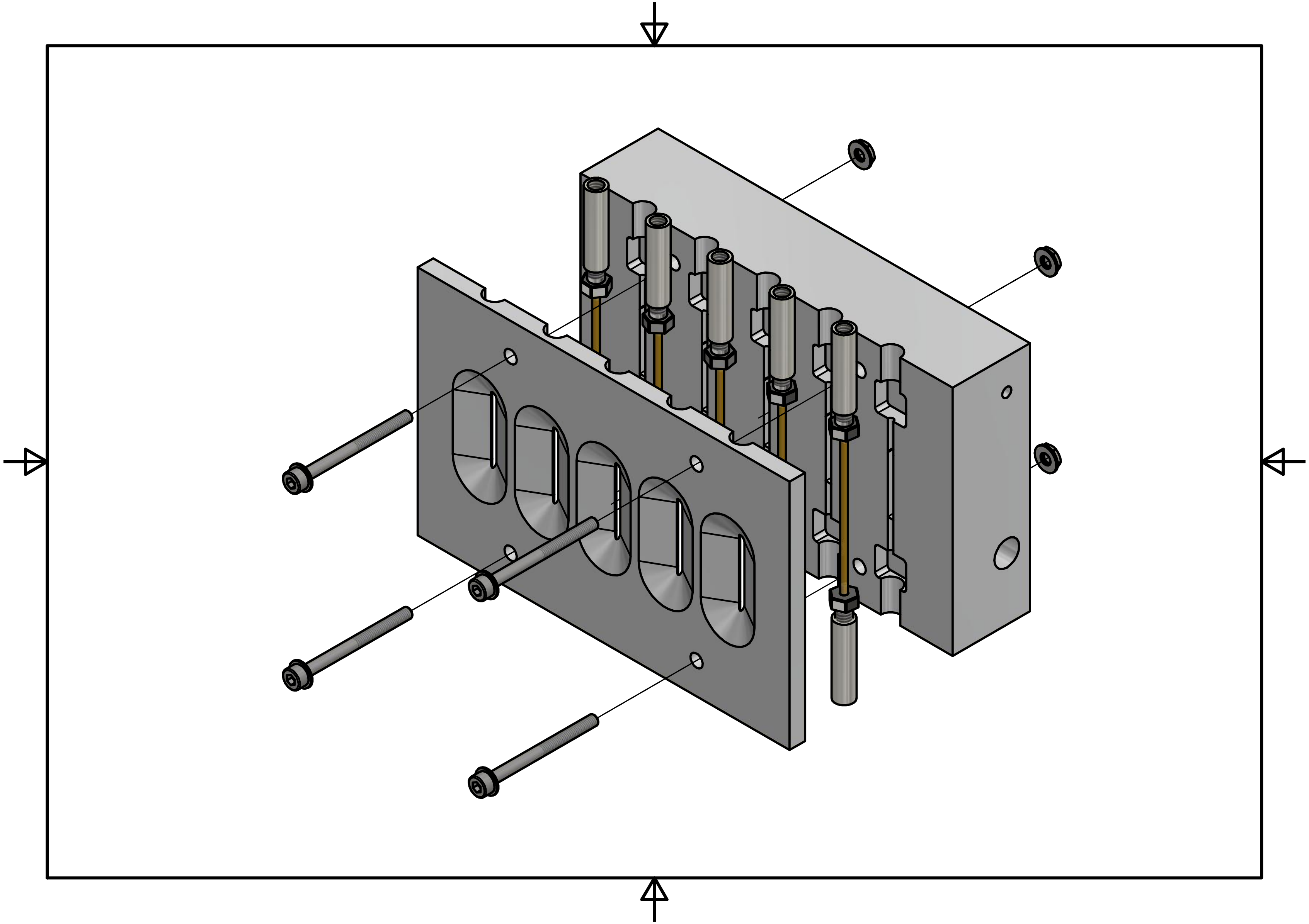

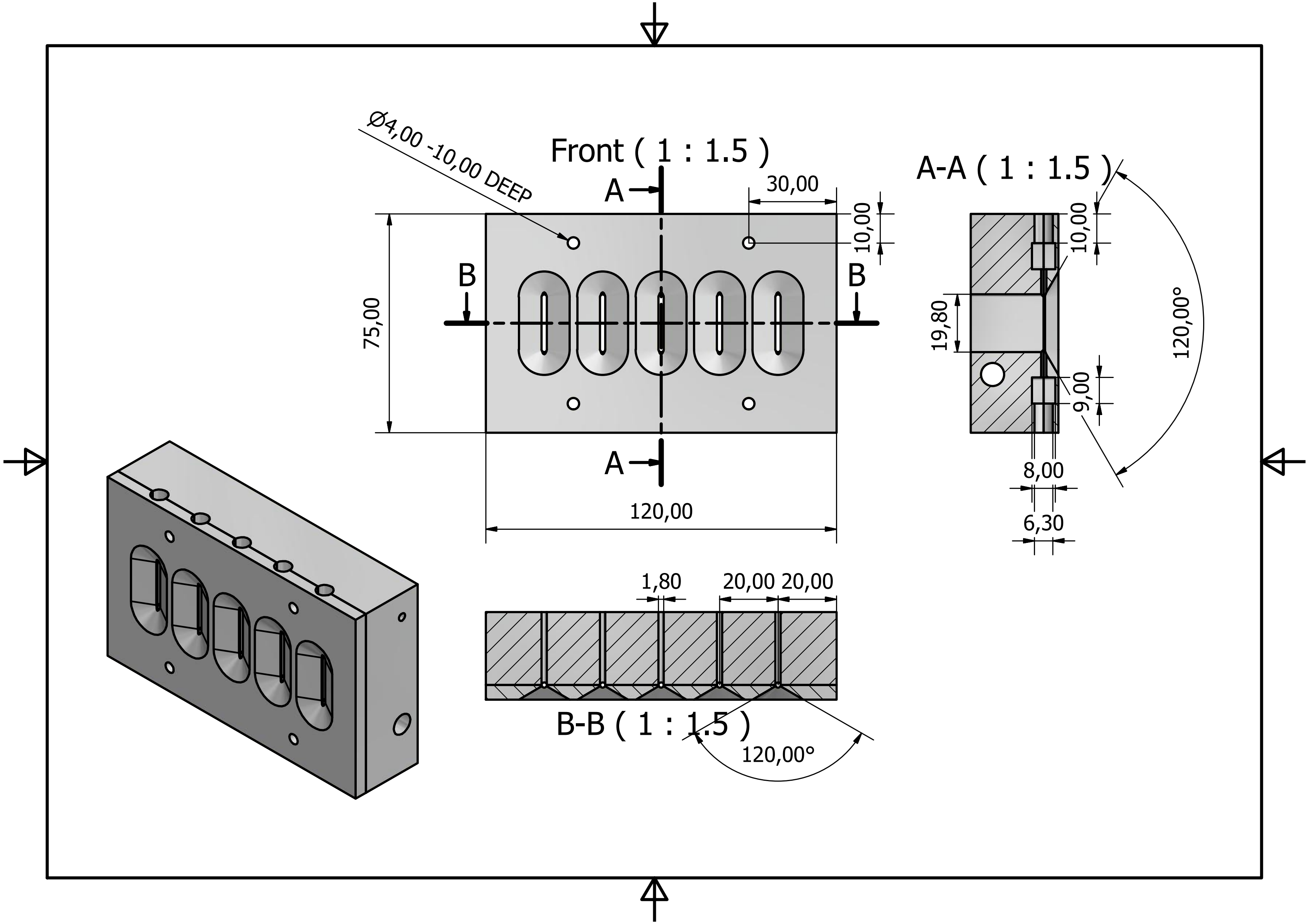
Front (1 : 1.5)
Ø4,00 -10,00 DEEP
A
A
B
B
30,00
10,00
75,00
120,00
A-A (1 : 1.5)
10,00
19,80
9,00
120,00°
8,00
6,30
1,80
20,00
20,00
B-B (1 : 1.5)
120,00°

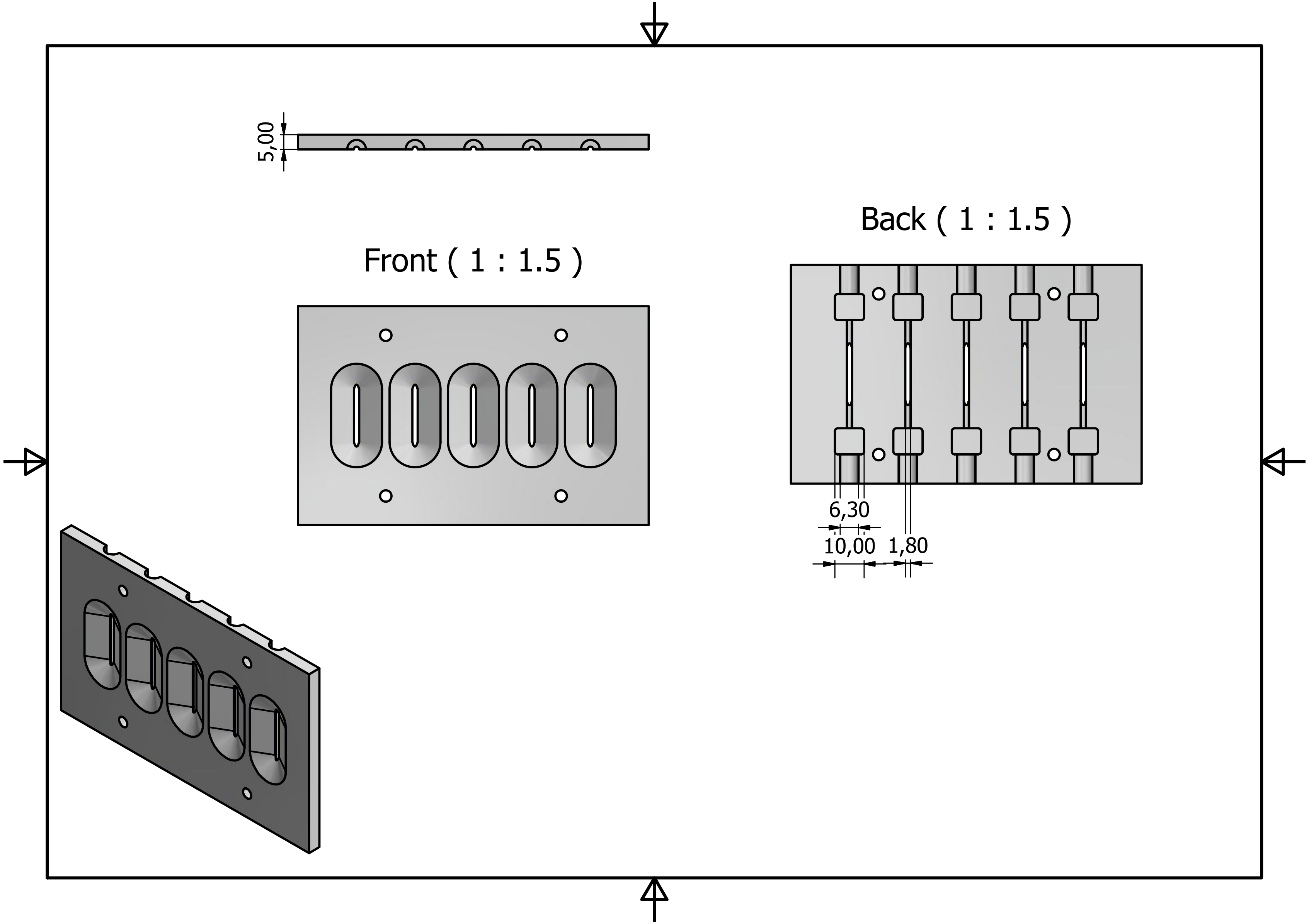
5,00
Front (1 : 1.5)
Back (1 : 1.5)
6,30
10,00
1,80

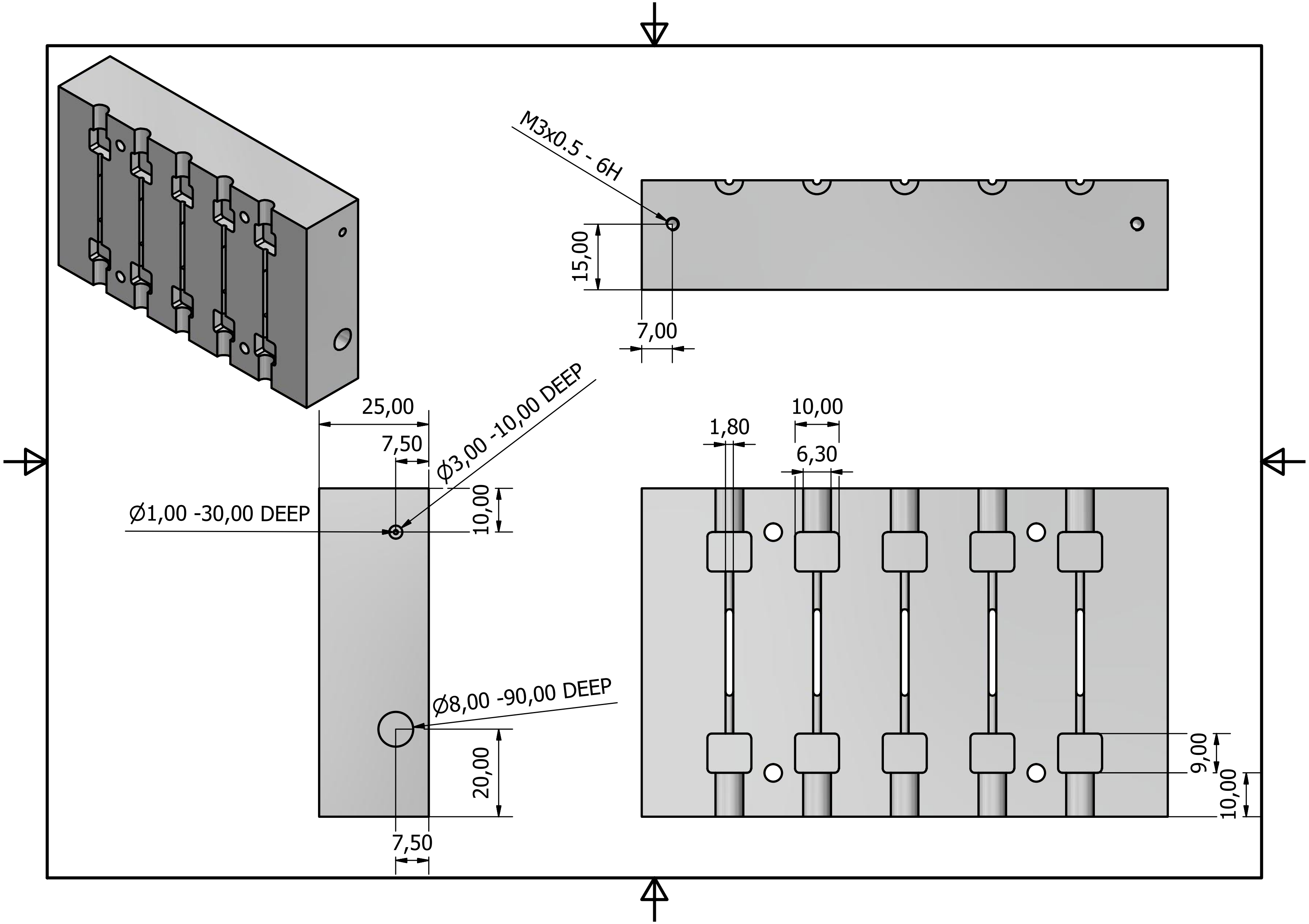
M3x0.5 - 6H
15,00
7,00
25,00
7,50
Ø3,00 -10,00 DEEP
Ø1,00 -30,00 DEEP
10,00
Ø8,00 -90,00 DEEP
20,00
7,50
1,80
10,00
6,30
9,00
10,00

B. Software Documentation

B.1. File Sorting Script

Listing B.1: Source code of the Python script used for sorting of measurement files from the online UV/Vis absorption spectrometer.

```
# -*- coding: utf-8 -*-
"""
Created on Mon Sep 22 16:12:41 2014

@author: rob
"""

import os
import numpy as np
import calendar as cal
import time

##########################################
# Definitions of filter methods
##########################################

def txt(item): return '.txt' in item

##########################################

# read all files in folder:
filelist = os.listdir('.')
```

```
# make sure only txt files are listed:
act_filelist = filter(txt, filelist)
# empty list for dates
dates = []

#############################################
# Make folders based on dates:
#############################################

for filename in act_filelist:
    # extracts date timestamp from filename:
    t_date = filename.strip('.txt').split('_')[2]
    # add all dates to date list:
    dates.append(t_date)
    # creates experiment directories based on dates, if they don't exist yet:
    if not os.path.exists(t_date):
        os.makedirs(t_date)
    os.rename(filename, t_date + '/' + filename)
# removes duplicate dates:
cleandate = list(set(dates))

#############################################

# for every experiment day:
for entry in cleandate:
    # makes list of files:
    times = []
    filelist = os.listdir(entry)
    filelist = filter(txt, filelist)
    filelist.sort()

    # extracts timestamp from filename:

```

```
    for filename in filelist:
        # removes file ending:
        t_time = filename.strip('.txt').split('_')[3]
        # creates UTC timestamp tuple from strings for hour, minute, second, milisecond from filename:
        t_utc = (int(entry[0:4]),int(entry[4:6]),int(entry[6:8]),int(t_time[0:2]),int(t_time[2:4]),int(t_time[4:6]))
        # converts utc timestamp to unix timestamp (in seconds):
        t_unix = cal.timegm(t_utc)
        times = np.append(times, int(t_unix))

    # creates array which contains the differences between unix timestamps (i.e. time difference between spectra)
    diffs = np.diff(times)



    # for every file:
    for i in range(len(times)):

        # The following conditional sequence sorts the files based on which measurement they are part of. It checks for first , last , and middle spectra of one experiment day.

        # For first spectra:
        if i == 0:
            # If absolute time difference between the file and the following file is larger than 1 s the file is discarded
            if abs(diffs[i]) > 1:
```

```
                if not os.path.exists(entry + '/restbert'):
                    os.makedirs(entry + '/restbert')
                os.rename(entry + '/' + filelist[i], entry + '/restbert/' + filelist[i])
            # If the above is not the case a new measurement folder is made with the time of the measurement as the name (HHMM) and the file is moved into it.
            else:
                dirname = str(time.gmtime(times[i])[3]) + str(time.gmtime(times[i])[4])
                if not os.path.exists(entry + '/' + dirname):
                    os.makedirs(entry + '/' + dirname + '/input')
                os.rename(entry + '/' + filelist[i], entry + '/' + dirname + '/input/' + filelist[i])

        # For last spectra:
        elif i == len(times)-1:
            # If the absolute time difference is larger than 1 s, the file is discarded.
            if abs(diffs[i-1]) > 1:
                if not os.path.exists(entry + '/restbert'):
                    os.makedirs(entry + '/restbert')
                os.rename(entry + '/' + filelist[i], entry + '/restbert/' + filelist[i])
            # If the above is not the case, the file is moved to the previously created directory.
            else:
                os.rename(entry + '/' + filelist[i], entry + '/' + dirname + '/input/' + filelist[i])

        # For all other spectra:
```

```
        else:
            # If the absolute time difference between the file and the previous as well as the next file is larger than 1 s, it is discarded.
            if abs(diffs[i-1]) > 1 and abs(diffs[i]) > 1:
                if not os.path.exists(entry + '/restbert'):
                    os.makedirs(entry + '/restbert')
                os.rename(entry + '/' + filelist[i], entry + '/restbert/' + filelist[i])
            # If the absolute time difference to the previous file is larger than 1 s and to the next file is less or equal than 1 s, it is a new measurement time, a respective directory is created and the file moved into it.
            elif abs(diffs[i-1]) > 1 and abs(diffs[i]) <= 1:
                dirname = str(time.gmtime(times[i])[3]) + str(time.gmtime(times[i])[4])
                if not os.path.exists(entry + '/' + dirname):
                    os.makedirs(entry + '/' + dirname + '/input')
                os.rename(entry + '/' + filelist[i], entry + '/' + dirname + '/input/' + filelist[i])
            # in all other cases it is a file belonging to the previous measurement and added to that directory.
            else:
                os.rename(entry + '/' + filelist[i], entry + '/' + dirname + '/input/' + filelist[i])
```

B.2. Data Treatment Script

Listing B.2: Source code of the Python script used for plotting and treatment of data obtained from the online UV/Vis absorption spectrometer.

```
#!/bin/python
# -*- coding: utf-8 -*-

import numpy as np
import matplotlib.pyplot as plt
import matplotlib.axes as axes
import os
import calendar as cal
from tkFileDialog import askdirectory

#functions needed to filter spectra from only one channel
def channel1(item): return 'CHANNEL1' in item
def channel2(item): return 'CHANNEL2' in item

#this function finds the index of one element in an array by
    comparing the differences between the array's elements
    and the value provided
def find_idx(array,value)    :
    if array.ndim > 1:
        if array[0,0]==array[0,1]:
            return np.argmin(np.abs(array-value)[:,0])
        else:
            return np.argmin(np.abs(array-value))
    else:
        return np.argmin(np.abs(array-value))



run = 1
runstate = 0 #the runstate defines the different options in
    the script
rslist = (0,1,2,3)
```

```

#the script is contained within this while loop, it runs, until the run variable is set to 0
while run:
    #if runstate is 0, the script calls on the user to select a root experiment directory
    if runstate == 0:
        maindir = askdirectory(title='Please␣choose␣root␣experiment␣directory...')
        runstate = 1
    #if runstate is 1, the script reads the contents of the selected root directory, lists them and asks the user to select a measurement directory (corresponding to a time of measurement)
    if runstate == 1:
        dirlist = os.listdir(maindir)
        dirlist.sort()
        print 'List␣of␣directories:\r'
        print dirlist
        dirname = maindir+'/'+raw_input('\nChoose␣working␣directory␣(Enter␣x␣to␣stop␣the␣program):␣')
    if dirname == maindir+'/x':
        run = 0
    elif dirname[-4:] not in dirlist:
        print '#########################\rPlease␣enter␣a␣directory␣that␣is␣present␣in␣your␣current␣working␣directory.\r#########################'
        raw_input('Press␣Enter␣to␣continue...')
    #upon selecting a measurement directory the program continues
    else:
        chan = raw_input('\nSelect␣measurement␣channel␣(1,2):␣')
```

```
        if not chan:#triggers if the user has entered no channel
            chan = raw_input('\nPlease enter a valid value for channel (1,2): ')
        ichan = int(chan)
        if ichan not in (1,2):#triggers if a wrong number has been entered
            chan = raw_input('\nPlease enter a valid value for channel (1,2): ')
            ichan = int(chan)

        cmd = raw_input('\nPlease enter the desired data interpretation method. The accepted format is a three-character number. First character for peaktrace, second character for timecut and third character for averaged spectrum. Values are 1 and 0. E.g.: 100 for peaktrace, 011 for timecut and averaging.: ')
        peaktrace = int(cmd[0])
        timecut = int(cmd[1])
        avplot = int(cmd[2])
        #the script always produces a 3d plot of the spectra against time, as well as a 2d colormap. With this input the user can decide, whether the temporal evolution of one wavelength shall be done (peaktrace), only a subset of all times shall be used (timecut) or an average of the whole data shall be calculated

        if peaktrace:#if peaktrace was selected, a wavelength is entered here
            peakwl = int(raw_input('Peak Wavelength? (in nm): '))

```

```
        print('Reading␣data...')
        filelist = os.listdir(dirname+'/input/')#the script
           generates a list of all files in the selected
           measurement directory's input subdirectory
        if ichan == 1:
            ch = filter(channel1, filelist)
        else:
            ch = filter(channel2, filelist)#the variable ch
                contains the filelist filtered by the channel
                 selected above (either 1 or 2)
        ch.sort()#essential to allow calculation of the time
            axis later on
        i = 0#counter for following loop

        #an empty numpy 2d array is created with one
           dimension corresponding to the number of spectra
           (length of ch) and the other dimension
           corresponding to the amount of intensity data
           points in one spectrum (185nm to 2205nm = 2021
           data points)
        intlist = np.empty(shape=[len(ch),2021])

        for filename in ch:#this loop runs over all files in
            the filelist

            #open the file in read mode in variable raw:
            raw = open(dirname+'/input/' + filename, 'r')
            #an empty array for wavelength and intensity is
               created
            wl = np.array([])
            intensity = np.array([])
            #skip first four lines (headers)
            raw.readline()
            raw.readline()
```

```
            raw.readline()
            raw.readline()

            #for every line in the file the values are read and then appended to the previously created arrays
            for line in raw:
                act_wl,act_intensity = line.strip('\n').split('\t')[0:2]
                wl = np.append(wl, float(act_wl))
                intensity = np.append(intensity, float(act_intensity))
            #the line in the previously created intlist array corresponding to the current run of the loop is set with the intensities from the file:
            intlist[i] = intensity
            i = i + 1

        #in this part, the starting timestamp is extracted from the first filename in the ch list:
        t_date0,t_time0,t_ms0 = ch[0].strip('.txt').split('_')[2:5]
        t_year0 = t_date0[0:4]
        t_month0 = t_date0[4:6]
        t_day0 = t_date0[6:8]
        t_hours0 = t_time0[0:2]
        t_min0 = t_time0[2:4]
        t_sec0 = t_time0[4:6]
        #the strings are recombined as utc time tuples, then converted to unix timestamps
        ts_utc0 = (int(t_year0), int(t_month0), int(t_day0), int(t_hours0), int(t_min0), int(t_sec0))
        ts_unix0 = cal.timegm(ts_utc0)
```

```
        #the unix timestamp is converted into ms and the ms value from the starting file is added
        ts_ms0 = float(ts_unix0*1000+int(t_ms0)*10)

        time = np.array([]) #creates an empty array for the time axis

        for filename in ch:#this loop extracts the timestamps from all files in the list
            t_date,t_time,t_ms = filename.strip('.txt').split('_')[2:5]
            t_year = t_date[0:4]
            t_month = t_date[4:6]
            t_day = t_date[6:8]
            t_hours = t_time[0:2]
            t_min = t_time[2:4]
            t_sec = t_time[4:6]
            ts_utc = (int(t_year), int(t_month), int(t_day), int(t_hours), int(t_min), int(t_sec))
            ts_unix = cal.timegm(ts_utc)
            ts_ms = float(ts_unix*1000 + int(t_ms)*10)
            #the difference between the current timestamp and the starting timestamp is appended to the array:
            time = np.append(time, ts_ms-ts_ms0)

        #parameters to cut diagrams
        wlstart = 300
        wlend = wl.max (axis=0)

        #if the timecut was requested, the user is asked here to give the start and end time, if they are not defined, or timecut is not called, the min and max of the time array are chosen:
```

```
        if timecut:
            tstart = float(raw_input('Start␣Time?␣(in␣s,␣0␣for␣minimum):␣'))*1000
            tend = float(raw_input('End␣Time?␣(in␣s,␣0␣for␣maximum):␣'))*1000
            if tstart == 0:
                tstart = time.min(axis=0)
            if tend == 0:
                tend = time.max(axis=0)
        else:
            tstart = time.min(axis=0)
            tend = time.max(axis=0)

        #x and y are created as 2d arrays with appropriate dimension, containing wavelengths and times
        x,y = np.meshgrid(wl,time)
        #indexes for wl and time cut are identified:
        wlcutstart = find_idx(wl,wlstart)
        wlcutend = find_idx(wl,wlend)
        timecutstart = find_idx(time,tstart)
        timecutend = find_idx(time,tend)

        #x, y, and intlist are cut based on wavelength and time cut, y is also converted to seconds
        xcut = x[timecutstart:timecutend+1,wlcutstart:wlcutend]
        ycut = y[timecutstart:timecutend+1,wlcutstart:wlcutend]/1000
        intcut = intlist[timecutstart:timecutend+1,wlcutstart:wlcutend]

        #the user is asked for experimental parameters
        rpm = float(raw_input('Please␣enter␣total␣Flow␣speed␣in␣ml/min:␣'))
```

```
        fileflow = str(rpm).split('.')
        ovl = raw_input('Please␣enter␣oven␣length␣in␣cm:␣')
        flovl = float(ovl)
        temp = raw_input('Please␣enter␣experiment␣temperature:␣')

        ###########################################################
        # Time resolution calculation (approximate)
        ###########################################################

        vmix = 3.8E-3 # in mL
        dtube = 0.1 # in cm
        if flovl != 0.0:
            vcon = 9 * (dtube/2)**2 * np.pi
        else:
            vcon = 0.0
        voven = flovl * (dtube/2)**2 * np.pi
        vtotal = vmix + vcon + voven
        tres = round(vtotal / rpm * 60, 3)

        ###########################################################
        #spectra folder is created where plot images will be saved
        if not os.path.exists(maindir+'/Spectra'):
            os.makedirs(maindir+'/Spectra')

        if avplot:
            avg_int = intcut.mean(axis=0)#averages all spectra along the time-axis

            #the output txt file is created, the filename contains experimental parameters and if timecut was selected, the start and end times:
```

```
        if timecut:
            output = open(maindir+'/Spectra/
               averageint_channel_' + chan + '_' +
               dirname[-4:] + '_' + fileflow[0] + 'p' +
               fileflow[1] + 'mLmin_' + ovl + 'cm_' +
               temp + 'C_'+str(tstart)+'_'+str(tend)+'.
               txt','w')
        else:
            output = open(maindir + '/Spectra/
               averageint_channel_' + chan + '_' +
               dirname[-4:] + '_' + fileflow[0] + 'p' +
               fileflow[1] + 'mLmin_' + ovl + 'cm_' +
               temp + 'C.txt','w')
        output.write('Wavelength\tAbsorbance\nnm\ta.u.\n
           ␣\t' + temp + '\n')
        #the values from avg_int are written in to the
           output file:
        for i in range(wlstart,int(wlend)):
            output.write(str(i) + '\t' + str(avg_int[i-
               wlstart]) + '\n')

        output.close()

    from mpl_toolkits.mplot3d import Axes3D
    from matplotlib import cm

    #clears and closes all open plots:
    plt.clf()
    plt.close()

    #fig1 contains the 3d plot of wavelength vs time vs
       absorbance, it contains a title including
       experimental parameters. The plot is saved as .
       PNG file, including a start and end time in case
```

```
            of timecut:
        fig1 = plt.figure()
        ax = fig1.add_subplot(111, projection='3d')
        ax.set_title(dirname[-4:] + ' Flow: ' + str(rpm) + ' mL/min Oven: ' + ovl + ' cm t_res: ' + str(tres) + ' s T = ' + temp + ' C')
        ax.plot_surface(xcut,ycut,intcut,color='yellow')
        ax.set_xlabel('Wavelength [nm]',fontsize='small')
        ax.set_ylabel('Time[s]',size='small')
        ax.set_zlabel('Absorbance',size='small')
        ax.tick_params(labelsize='small')
        if timecut:
            plt.savefig(maindir+'/Spectra/'+ dirname[-4:] + '_channel_' + chan + '_3dPlotCutforAv'+str(tstart)+'_'+str(tend)+'.PNG')
        else:
            plt.savefig(maindir+'/Spectra/'+ dirname[-4:] + '_channel_' + chan + '_3dPlot.PNG')

        #fig2 contains the colormap, which is also saved analogously to the 3d plot:
        fig2 = plt.figure()
        plt.imshow(intcut, origin='lower', interpolation='none', aspect='auto', extent=(xcut.min(),xcut.max(),ycut.min(),ycut.max()))
        plt.colorbar(orientation='horizontal')
        plt.xlabel('Wavelength [nm]')
        plt.ylabel('Time [s]')
        plt.title(dirname[-4:] + '; Flow:' + str(rpm) + ' mL/min; Oven: ' + ovl + ' cm; t_res: ' + str(tres) + ' s; T = ' + temp + ' C')
        if timecut:
            plt.savefig(maindir+'/Spectra/'+ dirname[-4:] + '_channel_' + chan + '_ColourmapCutforAv'+str
```

```
                (tstart)+'_'+str(tend)+'.PNG')
        else:
            plt.savefig(maindir+'/Spectra/'+ dirname[-4:] +
                '_channel_' + chan + '_Colourmap.PNG')

        #if peaktrace was selected, this creates a figure in
            which the intensity at the selected wavelength
           is plotted against the time. The plot is saved
           and a txt file containing the data is saved along
            with it:
        if peaktrace:
            pttimes = ycut[:,find_idx(xcut,peakwl)]
            ptints = intcut[:,find_idx(xcut,peakwl)]
            fig4 = plt.figure()
            ax1 = fig4.add_subplot(111)
            plt.plot(ycut[:,find_idx(xcut,peakwl)],intcut[:,
                find_idx(xcut,peakwl)],'b.')
            plt.ylabel('Absorbance␣(' + str(peakwl) + '␣nm)'
                )
            plt.xlabel('Time␣[s]')
            ax1.set_xbound(lower=ycut.min(),upper=ycut.max()
                )
            plt.savefig(maindir+'/Spectra/' + dirname[-4:] +
                 '_channel_' + chan + '_peaktrace_' + str(
                peakwl) + 'nm.PNG')
            output = open(maindir+'/Spectra/
                peaktrace_channel_' + chan + '_' + dirname
                [-4:] + '_' + str(peakwl) + 'nm.txt','w')
            output.write('Time(ms)\tAbsorbance(' + str(
                peakwl) + 'nm)\n')
            for i in range(len(ycut[:,find_idx(xcut,peakwl)
                ])):
                output.write(str(pttimes[i]) + '\t' + str(
                    ptints[i]) + '\n')
```

```
            output.close()

        #plots and saves the average spectrum:
        if avplot:
            fig5 = plt.figure()
            ax2 = fig5.add_subplot(111)
            plt.plot(xcut[0,0:],avg_int)
            plt.ylabel('Absorbance')
            plt.xlabel('Wavelength␣[nm]')
            plt.title(dirname[-4:] + ';␣Flow:' + str(rpm) + '␣mL/min;␣Oven:␣' + ovl + '␣cm;␣t_res:␣' + str(tres) + '␣s;␣T␣=␣' + temp + '␣C')
            ax2.set_xbound(lower=xcut.min(),upper=xcut.max())
            ax2.set_ybound(lower=intcut.min())
            if not os.path.exists(maindir+'/Spectra'):
                os.makedirs(maindir+'/Spectra')
            if timecut:
                plt.savefig(maindir+'/Spectra/'+ dirname[-4:] + 'channel_' + chan + '_AvgSpectrum_' + fileflow[0] + '_' + fileflow[1] + 'mLmin_' + ovl + 'cm_' + temp + 'C_' + str(tstart)+'_'+str(tend)+'.PNG')
            else:
                plt.savefig(maindir+'/Spectra/'+ dirname[-4:] + 'channel_' + chan + '_AvgSpectrum_' + fileflow[0] + '_' + fileflow[1] + 'mLmin_' + ovl + 'cm_' + temp + 'C.PNG')

        plt.show()#shows all plots
        #finally the user decides what to do next, i.e. in which section of the script to continue:
```

```
        runstate = int(raw_input('What would you like to do now? (0 = new root dir,1 = new experiment dir,2 = additional actions in current dir, 3 = exit): '))

        if runstate not in rslist:
            print 'Please enter a valid command.'
            runstate = int(raw_input('What would you like to do now? (0 = new root dir,1 = new experiment dir,2 = additional actions in current dir, 3 = exit): '))
        #choosing 3 ends the program:
        if runstate == 3:
            run = 0
```

C. Safety Data

Chemicals used in this work

The following table contains a list of chemicals used during this work as well as their hazard and precautionary statements according to the globally harmonized system of classification and labelling of chemicals (GHS).[132,133]

Substance	GHS Symbol	H Statements	P Statements
Cadmium(II) acetate	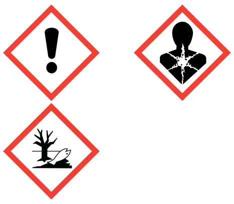	H302-H312-H332-H350-H410	P273-P280-P302+P352-P308+P313
Cadmium(II) acetate dihydrate	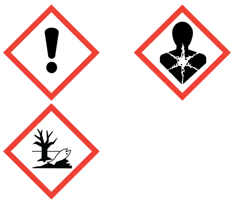	H302-H312-H332-H350-H410	P273-P280-P302+P352-P308+P313
Cadmium(II) oxide		H301-H330-H341-H350-H361fd-H372-H410	P201-P260-P280-P301+P330+P331+P310-P304+P340+P310-P308+P313

Substance	**GHS Symbol**	**H Statements**	**P Statements**
Cyanex 923 (mixture of tertiary Alkylphosphine oxides; Cytec Inc.)	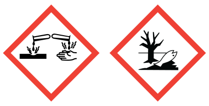	H314-H400	P260-P264-P280-P273-P301+P330+P331-P303+P361+P353-P304+P340-P305+P351+P338-P310-P321-P363-P391-P405-P501
Diphenylether		H319-H411	P264-P273-P280-P305+P351+P338-P337+P313-P501
Ethanol		H225-H319	P210-P240-P305+P351+P338-P403+P233
Nitric Acid	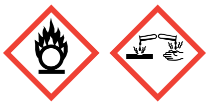	H272-H290-H314-EUH071	P280-P301+P330+P331-P304+P340-P305+P351+P338-P310
Octadec-1-ene		H304-EUH066	P301+P310-P331
Octadecylphosphonic acid	Kein Gefahrstoff gem. EG1272/2008		

Substance	**GHS Symbol**	**H Statements**	**P Statements**
Selenium		H301+H331-H373-H413	P260-P264-P273-P301+P310-P304+P340-P314-P321-P330-P403+P233-P405-P501
Toluene	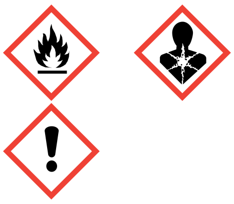	H225-H304-H315-H336-H361d-H373	P210-P240-P301+P310+P330-P302+P352-P308+P313-P314-P403+P233
Trioctylphosphine		H314	P280-P305+P351+P338-P310

D. Curriculum Vitae

Aus datenschutzrechtlichen Gründen entfällt der Lebenslauf in der Druckversion dieser Arbeit.

E. Acknowledgements

In diesem Abschnitt möchte ich einigen Personen meinen Dank aussprechen, die zu einem nicht unwesentlichen Teil zur Entstehung dieser Arbeit beigetragen haben. Insbesondere danke ich:

- Prof. Dr. Horst Weller für die Möglichkeit, meine Dissertation in seinem Arbeitskreis anzufertigen, die Betreuung während der Durchführung der praktischen Arbeiten, aber insbesondere auch die hilfreichen Diskussionen über die Interpretation der Messergebnisse. Ganz besonders möchte ich mich bedanken für die zahlreichen gewährten Möglichkeiten zu Konferenzbesuchen im In- und Ausland.
- PD Dr. Christian Klinke für die kurzfristige Übernahme des Zweitgutachtens.
- Dr. Cristina Palencia Ramírez für die hervorragende Zusammenarbeit im Rahmen des gemeinsamen CUI-Projekts, die zahllosen Diskussionen, aber vor allen Dingen, ihre Fähigkeit, die gute Stimmung in den langen Stunden am Reaktor stets aufrecht zu erhalten.
- Unseren Masterstudenten: Marcel Dohrmann, Jan Krohn und Felix Thiel für ihre stets engagierte Mitarbeit am Projekt, insbesondere bei der Vorbereitung, Durchführung und Nachbereitung der vier Beamtimes. Besonders in den Nachtschichten konnten so die besten Ideen entwickelt werden.
- Unseren Kooperationspartnern bei der Durchführung der Beamtimes: JProf. Dr. Martin Trebbin, Dr. Sebastian Bommel, Dr. Felix Lehmkühler, Lara Frenzel und Mohammad Vakili.
- Dr. Jan Niehaus für die Hilfe bei der anfänglichen Auslegung sowie des Aufbaus des kontinuierlichen Flussreaktors.

- Dr. Tobias Jochum für das zur Verfügung stellen seiner Precursorsynthese.
- Dem Sekretariat der PC: Martina Krasa, Beate Kreutzer und Sigrid Zeckert für die stete und oftmals kurzfristige Hilfe beim Lösen jedes erdenklichen organisatorischen Problems.
- Den Mitarbeitern des CUI Office sowie der CUI Graduate School für das Lösen der organisatorischen Probleme, die nicht in die Zuständigkeit der PC fielen.
- Der Feinmechanik- sowie der Elektronikwerkstatt der PC, durch die diverse Komponenten des kontinuierlichen Flussreaktors gebaut wurden.
- Den Praktikanten und Bachelorstudenten: Felix Thiel, Leif Mielke, Julia Nette, Laura Weidmann, Jonas Spethmann, Jan Krohn, Tuan Nguyen, Quint Duong und Leon Wasserfall für ihre Mitarbeit.
- Den Mitgliedern des Grill- und Hobelvereins: Dr. Anna Kreuziger, Svenja Kunze, Dr. Elisabeth Leib, Dr. Natalia Olichwer, Hendrik Schlicke, Jerry Willrodt sowie Dr. Sarah Wölper. Durch ihre Hilfe war es oft möglich, einen guten Ausgleich zur Arbeit zu schaffen.
- Meinen Bürokollegen in Büro 353, die noch in keinem anderen Punkt erwähnt sind: Friederieke Gorris und Lasse Habercorn dafür, dass es keinen einzigen langweiligen Arbeitstag gab.
- Der alten Besetzung von Büro 253: Dr. Wiebke Friedrich, Dr. Jannika Lauth, Dr. Florian Schulz und Dr. Lena Wittern für die gute Büroatmosphäre während des Anfangs meiner Doktorarbeit.
- Dem restlichen AK Weller für die allseits gute Stimmung und viele mehr oder minder sinnvolle Diskussionen im Sozialraum.
- Meiner Familie, meinen restlichen Freunden sowie insbesondere meiner Freundin Julia Ziegler für die viele Unterstützung in allen Lebenslagen.

F. Declaration of Authorship

Hiermit versichere ich an Eides statt, die vorliegende Dissertation selbst verfasst und keine anderen als die angegebenen Hilfsmittel benutzt zu haben. Die eingereichte schriftliche Fassung entspricht der auf dem elektronischen Speichermedium. Ich versichere, dass diese Dissertation nicht in einem früheren Promotionsverfahren eingereicht wurde.

Hamburg, den 18.08.2017

Robert Seher